AD-776 088

RESEARCH IN SEISMOLOGY

Frank Press, et al

Massachusetts Institute of Technology
Cambridge, Massachusetts

15 August 1973

Department of Earth and Planetary Sciences

Massachusetts Institute of Technology

Cambridge, Massachusetts 02139

RESEARCH IN SEISMOLOGY

Annual Report to

Air Force Office of Scientific Research

1 April 1972 - 31 March 1973

ARPA Order No. - 1827-1 / 2134

Program Code No. - 2F10

Name of Contractor - Massachusetts Institute of Technology

Effective Date of Contract - 1 April 1971

Contract Expiration Date - 28 February 1974

Amount of Contract - $552,389.00

Contract No. - F44620-71-C-0049

Principal Investigators - Frank Press, 617/253-3382
M. Nafi Toksöz, 617/253-6382
Keiiti Aki, 617/253-6397
Sean C. Solomon, 617/253-3786

Program Manager - William J. Best, 202/694-5456

Short Title of Work - Research in Seismology

Sponsored by
Advanced Research Projects Agency
ARPA Order No. 1827-1 / 2134

250

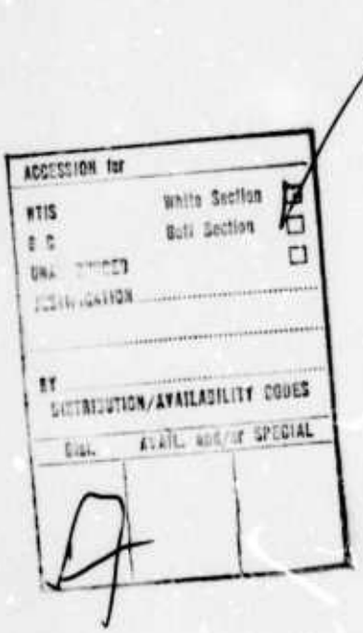

Qualified requestors may obtain additional copies from the Defense Documentation Center. All others should apply to the National Technical Information Service.

Approved for public release, distribution unlimited.

AIR FORCE OFFICE OF SCIENTIFIC RESEARCH (AFSC)
NOTICE OF TRANSMITTAL TO DDC
This technical report has been reviewed and is approved for public release IAW AFR 190-12 (7b).
Distribution is unlimited.
D. W. TAYLOR
Technical Information Officer

UNCLASSIFIED

Security Classification

DOCUMENT CONTROL DATA - R & D

(Security classification of title, body of abstract and indexing annotation must be entered when the overall report is classified)

1 ORIGINATING ACTIVITY *(Corporate author)*

Massachusetts Institute of Technology
Department of Earth & Planetary Sciences
Cambridge, Massachusetts 02139

2a. REPORT SECURITY CLASSIFICATION

UNCLASSIFIED

2b. GROUP

3 REPORT TITLE

RESEARCH IN SEISMOLOGY

4 DESCRIPTIVE NOTES *(Type of report and inclusive dates)*

Scientific. -------- Interim.

5 AUTHOR(S) *(First name, middle initial, last name)*

Frank Press
M. Nafi Toksöz
Keiiti Aki
Sean C. Solomon

6 REPORT DATE	7a. TOTAL NO. OF PAGES	7b. NO. OF REFS
15 August 1973	254	194

8a. CONTRACT OR GRANT NO	9a. ORIGINATOR'S REPORT NUMBER(S)
F44620-71-C-0049	
b. PROJECT NO AO 1827	
c. 62701E	9b. OTHER REPORT NO(S) *(Any other numbers that may be assigned this report)* AFOSR - TR - 74 - 0356
d.	

10 DISTRIBUTION STATEMENT

Approved for public release, distribution unlimited.

11 SUPPLEMENTARY NOTES	12. SPONSORING MILITARY ACTIVITY
TECH, OTHER	AFOSR (NPG) 1400 Wilson Blvd. Arlington, Virginia 22209

13 ABSTRACT

This report gives a summary of the projects conducted during the last year under the contract Research in Seismology. These investigations fall roughly under three broad headings: (1) Theoretical studies of source mechanisms of earthquakes and underground nuclear explosions; (2) Earth structure and path effects, especially the effects of lateral heterogeneities in velocity and in Q; (3) Studies of the capabilities of arrays for event detection and location. Lists of publications and theses completed during the contract year are also included.

DD FORM 1 NOV 65 1473

1c

UNCLASSIFIED

Security Classification

14 KEY WORDS	LINK A		LINK B		LINK C	
	ROLE	WT	ROLE	WT	ROLE	WT
Attenuation						
Body waves						
Earth heterogeneities						
Earthquakes						
Earth structure						
Seismic discrimination						
Seismology						
Source mechanism						
Surface waves						
Wave propagation						

Department of Earth and Planetary Sciences

Massachusetts Institute of Technology

Cambridge, Massachusetts 02139

RESEARCH IN SEISMOLOGY

Annual Report to

Air Force Office of Scientific Research

1 April 1972 - 31 March 1973

ARPA Order No. - 1827-1 / 2134

Program Code No. - 2F10

Name of Contractor - Massachusetts Institute of Technology

Effective Date of Contract - 1 April 1971

Contract Expiration Date - 28 February 1974

Amount of Contract - $552,389.00

Contract No. - F44620-71-C-0049

Principal Investigators - Frank Press, 617/253-3382
M. Nafi Toksöz, 617/253-6382
Keiiti Aki, 617/253-6397
Sean C. Solomon, 617/253-3786

Program Manager - William J. Best, 202/694-5456

Short Title of Work - Research in Seismology

Sponsored by

Advanced Research Projects Agency

ARPA Order No. 1827-1 / 2134

ABSTRACT

This report gives a summary of the projects conducted during the last year under the contract Research in Seismology. These investigations fall roughly under three broad headings: (1) Theoretical studies of source mechanisms of earthquakes and underground nuclear explosions; (2) Earth structure and path effects, especially the effects of lateral heterogeneities in velocity and in Q; (3) Studies of the capabilities of arrays for event detection and location. Lists of publications and theses completed during the contract year are also included.

TABLE OF CONTENTS

1. SUMMARY

In this annual report we review the work completed under the contract Research in Seismology during the year 1 April 1972 through 31 March 1973. Within the broad guidelines of the problem of discriminating earthquakes from underground nuclear explosions, we have conducted a number of specific investigations of seismic sources and seismic-wave propagation.

The topics studied can be grouped under three broad headings:

(1) Source mechanisms of earthquakes and explosions,

(2) Earth structure and path effects,

(3) Array studies.

In the following sections we present abstracts of papers published or soon to be published that fall into each category. Recently completed work is discussed in fuller detail. We also include lists of all publications and theses supported under this project during the contract year.

Several theoretical approaches to seismic source mechanisms have been followed. Y. Ida has pursued further his propagating-crack model for earthquake rupture. The model has the advantage that it links seismic observations such as near-field acceleration to physical properties of rocks such as static and dynamic friction. Variations in the

parameters used to formulate the boundary condition across the fault plane can explain the transition between stick-slip and stable sliding observed in rock failure, the dissimilarity in the amplitude spectra of large and small earthquakes, and rates of seismicity along faults.

A number of related theoretical seismic source models were constructed by S. Singh. His approach was to superpose point forces along some boundary in a medium of specified elastic or viscoelastic properties and to solve for the resulting displacement and stress fields. Among the interesting results of his studies are the demonstration that apparently torsion-free sources can generate SH-type waves and that the effects of viscoelasticity can significantly alter the displacement of stress fields for certain kinds of faulting from those calculated assuming perfect elasticity.

A number of advances were made toward inverting normal-mode and travel-time data to infer models of earth structure. Bounds on shear velocity and density in the mantle and core were obtained explicitly by C. Johnson using a new linear programming technique. In a related work, Wiggins, McMechan and Toksöz developed a procedure, based on the Herglotz-Wiechert integral, for direct determination of the envelope of possible body-wave velocities in the mantle and core.

Both of these studies have both clarified the limits of uncertainty in current earth models and pointed toward new data sets that would improve present constraints.

A major focus of our attention has been directed toward understanding lateral as well as radial variations in earth structure. As a consequence of a P-wave travel-time study using waves from deep earthquakes to minimize near-source heterogeneity, M. Sengupta and B. Julian noticed systematic differences in deep-mantle travel times for various paths. A lateral variation of P-wave velocity in the lower mantle of at least 1 percent is required.

The anomalous patterns of travel-time delays and amplitude variations across LASA have been recognized for some time. K. Aki has shown that this may be attributed to scattering by random velocity fluctuations in the crust beneath the array. The scattering is quite severe and the simple Chernov theory which fits the observations at lower frequencies (.5 Hz) is inadequate at higher frequencies (> 1 Hz).

The theory of plate tectonics has led to the recognition of a number of specific heterogeneities in earth structure, in particular the regions in the vicinity of plate boundaries at spreading centers and at subduction zones. When seismic sources are located in such regions, the effects on the

propagation of body waves can be pronounced. S. Solomon has demonstrated the striking azimuthal dependence of shear-wave spectra from earthquakes near ridges due to a localized zone of very low Q in the uppermost mantle beneath the ridge crest. M.N. Toksöz and his colleagues N. Sleep and A. Smith have further pursued their models of temperature and stress in subducted slabs of lithosphere. Current models successfully explain the travel-time and amplitude anomalies associated with shallow earthquakes and explosions on island arcs and the distribution and focal mechanisms of deep, intra-slab earthquakes.

The efficient utilization of the large aperture seismic arrays LASA and NORSAR has long been one of our continuing interests. In his Ph.D. thesis and later work, S. Shlien has made extensive statistical studies of the capability of the combined arrays for on-line signal detection and event location.

2. SOURCE MECHANISMS OF EARTHQUAKES AND EXPLOSIONS

2.1. Stress Concentration and Unsteady Propagation of Longitudinal Shear Cracks by Y. Ida (Abstract)

Unsteady propagation of a longitudinal-shear crack is studied through numerical calculation for better understanding of fracture and earthquakes. The relation which formulates rupture velocity as a function of stress intensity is used to describe the fracture process at the crack tip. The effects of creep and frictional slidings are taken into account by assuming a suitable form of the slip-velocity dependent boundary condition. In this model, stress accumulation takes place through creep, and then the crack begins to grow, controlled by the dynamic friction across the crack surface. It is shown that the motion of the crack tip is either smooth or bumpy, depending on the parameters of the boundary condition. The brittleness and ductility of material are interpreted by these two types of crack propagation, and this interpretation is qualitatively consistent with the experimental results on brittle-ductile transition induced by the temperature, the confining pressure, and the pore pressure. It is shown that the presence of smooth and bumpy crack propagations might give a possible explanation on the dissimilarity between large and small earthquakes, pointed

out by Aki. This model also suggests a method of estimating the recurrence period of earthquakes, based on the crustal deformation across the fault.

2.2 Cohesive Force and Unsteady Propagation of a Longitudinal-Shear Crack by Y. Ida (abstract)

The dynamic propagation of a longitudinal-shear crack is studied to form a model of fracture that has some physical basis. The stress field around the crack tip is analyzed in detail, under the assumption that the cohesive force is given as a function of the displacement discontinuity. This analysis yields a fracture condition which turns out to be equivalent to the energetic criterion, but the meaning of specific surface energy is made clearer. The stress distribution in the vicinity of the crack tip is demonstrated for several models of cohesive force diagrams. It is assumed that the slip velocity-dependent boundary condition, which includes the effect of creep and the static and dynamic frictions governs the semi-infinite fault plane except for the infinitesimally small end-region associated with cohesive force. Based on these formulations of the fracture and boundary conditions, the crack growth is calculated numerically. In this model, the stress accumulation first takes place through the creep over the whole fault plane,

and then the crack begins to grow, accompanied by the formation of the crack surface having the dynamic friction. It is shown that the crack tip is either "smooth" or "bumpy," depending on the parameter of the boundary condition. Smooth propagation is associated with the rapid expansion of the crack surface, while the bumpy propagation only produces the crack surface on the restricted area adjacent to the crack tip. The brittle and ductile fractures of the material are interpreted by these two types of crack propagation, and this interpretation successfully predicts the brittle-ductile transition induced by the temperature, the confining pressure, and the pore pressure.

2.3 The Maximum Acceleration of Seismic Ground Motion

by Y. Ida

Abstract

The near-field particle motion is evaluated on the basis of the idea that the initial shape of the seismic source function should be determined by the fracturing process in the rupture front. The effect of the cohesive force on the source function is examined in detail, and the following relations are derived for the maximum velocity

$\dot{U}_M$ and the maximum acceleration $\ddot{U}_M$; $\dot{U}_M \sim (\sigma_o/\mu)c$ and $\ddot{U}_M \sim (\sigma_o/\mu)^2(c^2/D_o)$, where σ_o is the strength, D_o is the displacement discontinuity required for the fracture, c is the rupture velocity and μ is the rigidity. If the strength of rock is assumed to govern the earthquake rupture ($\sigma_o \sim 1$ kbar and $D_o \sim 10$ cm), reasonable values are obtained, as $\dot{U}_M \sim 100$ cm/s and $\ddot{U}_M \sim 1$ g. The period and the dimension associated with the large particle acceleration are roughly 0.1 second and 100 meters, respectively, under the above assumption. This result suggests the possibility that earthquake hazard may be predicted from the mechanical property of rocks.

INTRODUCTION

In the vicinity of a seismic fault, it is expected that the ground motion is primarily governed by the fault-slip time function rather than the geometry and size of the fault plane. For the purpose of engineering seismology, it is thus very important to determine the accurate form of the fault-slip time function. Brune (1970) proposed a simple model of seismic source, assuming that the slip motion occurs instantaneously over the whole fault plane. In his model, the particle motion is related to the pre-existing stress field. It is physically more natural, however, to regard the earthquake occurrence as spontaneous rupture propagation associated with the stress concentration in the rupture front. If this is the case, the rupture cannot propagate supersonically, and Brune's time function is no longer applicable (Ida and Aki, 1972).

In the case of a subsonic rupture propagation, the entire form of source function involves several complicated effects, such as the initial state of the displacement field, and the dynamic processes of fracture and friction. If we restrict our consideration to the initial rise of source time function, however, the analysis can be made

more simply. For this purpose, we may focus our attention on the vicinity of the crack tip, since the effect of high stress concentration is so dominant there that the displacement field is almost determined by the material strength alone (Ida, 1972). The known solutions of dynamic crack propagation (Yoffe, 1951; Broberg, 1961; Kostrov, 1966) have a singularity of particle velocity or acceleration at the rupture front. This means that the initial form of source function corresponding to the rupture front gives the most important contribution in the estimation of the maximum velocity and acceleration of the near-field ground motion. In this paper, we estimate these quantities, based on the analysis of cohesive force at the crack tip (Ida, 1972).

COHESIVE FORCE AND PARTICLE MOTION

The singularity at the crack tip is eliminated by considering an inelastic property of material in the fault plane near the tip. According to Barenblatt (1959), the inelasticity is formulated by the "cohesive force" that works across the crack tip against the fracture. Let us

assume that the cohesive stress σ_c is given as a function of the displacement discontinuity D across the fault plane. The relation $\sigma_c = \sigma_c(D)$ is usually called the "cohesive force diagram". The direction of D relative to the geometry of the fault plane depends on whether the crack is of plane shear, tensile, or longitudinal-shear type, and $\sigma_c(D)$ is generally a different function for the different types of crack. The displacement discontinuity D is an unknown function of time t and space coordinate x_1. We here choose as x_1 the coordinate axis that is placed along the fault plane, perpendicularly to the crack edge which is assumed to be an infinite line. The form of D in the vicinity of the crack tip is determined for a given $\sigma_c(D)$, as has been studied in the case of the longitudinal-shear crack (Ida, 1972). The same discussion is also applicable to plane shear and tensile cracks, simply by replacing the factor involving the rupture velocity [see eqs. (7a), (7b) and (7c)].

To obtain practically useful expressions for particle motion, we introduce a "normalized" cohesive force diagram $\sigma(\phi)$, as

$$\sigma_c(D) = \sigma_o \cdot \sigma(D/D_o) \tag{1}$$

The constants σ_o and D_o are the representative values of stress and displacement. Let us choose as σ_o the stress of elastic limit (which is approximately equal to the yield strength), and as D_o the displacement required to break down the cohesion. Then we have

$$\sigma(0) \sim 1$$

$$\sigma(\phi) \sim 0 \text{ for } \phi \gtrsim 1 \tag{2}$$

If $\sigma(\phi)$ is given, a <u>normalized</u> displacement discontinuity ϕ is determined as a function of a normalized coordinate X (Ida, 1972). The non-normalized displacement discontinuity D is obtained from the scaling relation [eq.(17) of Ida (1972)], as

$$D = D_o\phi[-k(x_1 - ct)] \tag{3}$$

with the expression of X in terms of space and time:

$$X = -k(x_1 - ct) \tag{4}$$

Here c is the rupture velocity ($c > 0$), and k is defined by

$$k = (32\gamma/\pi\mu)(\sigma_o/D_oC) \tag{5}$$

where μ is the rigidity, and γ is the normalized specific

surface energy, i.e.,

$$\gamma = (1/2)\int_0^\infty \sigma(\phi)\,d\phi \tag{6}$$

The dimensionless constant C in (4) is a universal function of c. In the case of the longitudinal-shear crack, C is simply (Ida, 1972):

$$C = (1 - c^2/\beta^2)^{1/2} \tag{7a}$$

where β is the shear-wave velocity. For the other types of cracks, C also involves the longitudinal-wave velocity α. According to Weertman (1969), we have

$$C = 4(\beta/c)^2(1 - c^2/\beta^2)^{-1/2}[(1 - c^2/\alpha^2)(1 - c^2/\beta^2) - (1 - c^2/2\beta^2)^2] \tag{7b}$$

for the plane shear crack, and

$$C = 4(\beta/c)^2(1 - c^2/\alpha^2)^{-1/2}[(1 - c^2/\alpha^2)(1 - c^2/\beta^2) - (1 - c^2/2\beta^2)^2] \tag{7c}$$

for the tensile crack.

In fact, the nature of cohesive force is not known very well experimentally nor theoretically. Here we try to estimate roughly the effect of σ_o and D_o on the particle motion without detailed information on cohesion, remembering that the variation of $\sigma(\phi)$ is greatly restricted by (2). This kind of crude approximation is practically useful, because the parameters σ_o and D_o can be estimated more easily, even if it may be difficult to determine the complete form of cohesive force diagram.

On the fault plane, the displacement u is related to the source function D, as

$$u = (1/2)D \tag{8}$$

and thus the particle velolity $\dot{u}$ and acceleration $\ddot{u}$ are readily obtained from the function ϕ;

$$\dot{u} = (1/2)D_o k c \phi'$$

$$\ddot{u} = (1/2)D_o k^2 c^2 \phi''$$

where ϕ' and ϕ'' denote the derivatives of ϕ with respect to X. If the function $\phi'(X)$ has the maximum value ϕ_M' at a point $X = X_M$, we have the following expression of the maximum particle velocity $\dot{u}_M$:

$$\dot{u}_M = (16\gamma\phi_M'/\pi)(\sigma_o c/\mu C) \tag{9}$$

Here let us choose the origine of X so that $\phi(0) = 0$. By calculating $\phi(X)$ for several models of cohesive force diagram $\sigma(\phi)$, it was shown that $\phi'(X)$ actually has a maximum (Ida, 1972). The first five models in Table 1 cover the results in this calculation. In model 1, $\phi'(X)$ is infinite at $X = X_M$, since $\sigma(\phi)$ is discontinuous at $\phi = 1$. In this model, the infinity of ϕ_M' is clearly caused by the artificial choise of $\sigma(\phi)$. For the other models, ϕ_M' shows a finite value around unity in spite of the differences in details of the curves $\sigma(\phi)$. Roughly speaking, the dimensionless factor $16\gamma\phi_M'/\pi$ in (9) is thus expected to be of the order of the unity. From (4) and (5), we define x_M and t_M as

$$x_M = (\pi X_M/32\gamma)(\mu D_o/\sigma_o C) \tag{10}$$

$$t_M = x_M/c \tag{11}$$

which give the dimension and duration associated with large particle velocity. In the same manner, we have the maximum acceleration $\ddot{u}_M$, if $\phi''(X)$ has a maximum ϕ''_M:

$$\ddot{u}_M = (512\gamma^2\phi_M''/\pi^2)(\sigma_o\, c\, /\mu D_o C)^2 D_o \qquad (12)$$

In fact, ϕ''_M is infinite for all the models 1 through 5 in Table 1. The behavior of $\phi''(X)$ is thus examined in more detail in the next section.

SINGULARITY IN ACCELERATION

In the models 1 through 5 in Table 1, $\phi''(X)$ is proportional to $X^{-1/2}$ in the vicinity of $X = 0$, and not finite at $X = 0$. Furthermore, $\phi''(X)$ is also infinite at the point $\phi = 1$ in some models (1, 2, 4 and 5). Of these two singularities, the behavior around $\phi = 1$ simply reflects a more or less unsmooth connection of $\sigma(\phi)$ at this point; we arbitrarily assumed that $\sigma(\phi)$ vanishes for $\phi > 1$. Since the function $\phi'(X)$ is given by the Hilbert transform of $\sigma_{32}(X) = \sigma[\phi(X)]$ (Ida, 1972), $\phi''(X)$ is finite at $\phi = 1$ if $\sigma'(\phi)$ is continuous there. This condition is actually satisfied in model 3.

To study the behavior of $\phi(X)$ in the vicinity of $X = 0$, we rewrite the relation between $\phi'(X)$ and $\sigma_{32}(X)$ given in Ida (1972), as

$$\phi'(X) = -(X^{1/2}/16\gamma)\int_0^\infty (Y - X)^{-1} Y^{-1/2} [\sigma_{32}(Y) - \sigma_{32}(0)]dY \tag{13}$$

From (13), it is readily found that the following relation is necessary so that $\phi''(X)$ may be finite at $X = 0$:

$$\int_0^\infty Y^{-3/2} [\sigma_{32}(Y) - \sigma_{32}(0)]dY = 0 \tag{14}$$

Let us demonstrate through numerical calculation that $\phi''(X)$ can actually be finite at $X = 0$, if a suitable function is chosen as $\sigma(\phi)$. We consider the following cohesive force diagram, for example;

$$\sigma(\phi) = \begin{cases} a(\phi + \ell_1)(\phi - \ell)^2 & 0 \leqq \phi \leqq \ell \\ 0 & \phi \geqq \ell \end{cases} \tag{15}$$

putting $a = 2$ and $\ell + \ell_1 = 1.5$ in (15), we keep ℓ as an independent variable. The examples of the curve $\sigma(\phi)$ are given for several values of ℓ in Fig. 1. Since $\sigma'(\phi)$ in (15) is continuous at $\phi = \ell$, $\phi''(X)$ is finite except at $X = 0$ for any value of ℓ. The

distribution of $\phi(X)$ can be obtained in the same manner as described in Ida (1972). Fig. 2 shows the result for $\phi'(x)$. When ℓ is larger, the peak shifts to the right, and the steep rise of the curve around $X = 0$ is gradually removed. Finally, at $\ell = 1.37$, the condition (14) is approximately met, and $\phi'(x)$ increases smmothly at $X = o$ within the error of numerical calculation. The distribution of $\phi''(X)$ is given in Fig. 3. Corresponding to the behavior of $\phi'(X)$, $\phi''(0)$ approaches zero in the case of $\ell = 1.37$. The cohesive force diagram for $\ell = 1.37$ is denoted by Model 6 in Table 1.

Naturally, the cohesive force diagram that is physically realizable must give finite particle acceleration everywhere. Therefore we understand that the condition (14) is a physical requirement for $\sigma(\phi)$. For such $\sigma(\phi)$ that satisfies (14), eq. (12) may be used in the estimation of the maximum acceleration. The condition (14) is regarded as the criterion to determine the critical stress $\sigma(0)$, or $\sigma_c(0)$, above which the deformation is locally so concentrated that the displacement discontinuity appears along a crack surface in the continuous medium.

THE EFFECT OF DISTANCE FROM THE FAULT

When the observation point is not situated on the fault plane, the particle motion is generally affected by various factors of the sources, such as the dimension of the fault plane and the starting or stopping phases of rupture, other than the source-time function. For a distance that is sufficiently smaller than the source dimension, however, the stress field may still be approximated by our simple 2-dimensional crack model, and we may estimate how the particl motion attenuates in the near field. In this section, we consider this effect of distance in the case of the longitudinal-shear crack. For the other types of cracks, the mathematical treatment will be a little more complicated.

For the two-dimensional longitudinal-shear crack, the displacement u is given at an arbitrary point (x_1, x_2) (Ida and Aki, 1972) by

$$u = (1/2\pi)(1 - c^2/\beta^2)^{1/2} \, x_2 \int_{-\infty}^{\infty} [x_1'^2 + (1 - c^2/\beta^2) x_2^2]^{-1} \cdot D(x_1 - ct - x_1') dx_1' \qquad (16)$$

where the coordinate x_2 is perpendicular to the fault

plane and thus $|x_2|$ is the distance from the fault plane. Corresponding to (3) and (4), we introduce the normalized displacement U with the normalized coordinate X_2, as

$$U = u/D_o \tag{17}$$

$$X_2 = (32\gamma\sigma_o/\pi\mu D_o)x_2 \tag{18}$$

Because of the symmetry of the problem, we have only to consider the positive side of X_2. The particle velocity $\dot{u}$ and acceleration $\ddot{u}$ are derived from U, as

$$\dot{u} = D_o kc(\partial U/\partial X) \tag{19}$$

$$\ddot{u} = D_o k^2 c^2 (\partial^2 U/\partial X^2) \tag{20}$$

and thus the relative attenuations of $\dot{u}$ and $\ddot{u}$ are given by $\partial U/\partial X$ and $\partial^2 U/\partial X^2$ as a function of X_2. For the numerical calculation, the following relation that is derived with the use of eq. (10') in the paper of Ida (1972) is more convenient than (16):

$$\partial U/\partial X = (1/4)(2R)^{-1/2}\{(1 + X/R)^{1/2}$$

$$- (1/8\gamma)\int_0^\infty [(1 - X/R)^{1/2}X_2 + (1 + X/R)^{1/2}(Y - X)]$$

$$Y^{1/2}[(Y - X)^2 + X_2^2]^{-1}\sigma_{32}(Y)dY\} \qquad (21)$$

where

$$R = (X_1^2 + X_2^2)^{1/2}$$

The function $\sigma_{32}(Y)$ denotes the stress on the fault plane (at $X_2 = 0$). The results of the calculation are shown in Figs. 4 and 5 for model 6 of $\sigma(\phi)$. These figures give the distribution of $\partial U/\partial X$ and $\partial^2 U/\partial X^2$ as a function of X at various points of X_2. The maximum values of the normalized velocity and acceleration are listed for various values of X_2 in Table 2. We may find that the acceleration $\ddot{u}$ decreases rapidly with increasing X_2, and becomes much smaller than ϕ_M'' when X_2 exceeds X_M. Therefore the length X_M defined by (10) approximately gives the distance within which we expect as large an acceleration as on the fault plane. It is emphasized that the result of Table 2 involves only the effect of time function and does not explain the actual ground motion for very large distances.

ORIGIN OF STRONG GROUND MOTION

It has been shown that the cohesive force diagram (I) determines the fault-slip time function at the initial stage, and yields the expressions (9) and (12) for the maximum velocity $\dot{u}_M$ and acceleration $\ddot{u}_M$ on the fault plane. For a rough estimation, we may drop numerical factors involving γ, ψ_M' and ϕ_M'', and we have

$$\dot{u}_M \sim (\sigma_o/\mu)c \tag{22}$$

$$\ddot{u}_M \sim (\sigma_o/\mu)^2(c^2/D_o) \tag{23}$$

In a similar manner, we obtain the following approximate relations from (10) and (11):

$$x_M \sim (\mu/\sigma_o)D_o \tag{24}$$

$$t_M \sim (\mu/\sigma_o)(D_o/c) \tag{25}$$

Let us try to substitute the values of σ_o and D_o corresponding to the following two mechanisms of cohesion: (1) interatomic interactions ($\sigma_o \sim \mu$ and $D_o \sim 1$ Å), and (2) the gross strength of rocks broken by the

displacement comparable with the thickness of the seismic fault ($\sigma_o \sim 1$ Kbar and $D_o \sim 10$ cm). The results of the estimation are given in Table 3. In the first case, we have very large velocity and acceleration, but the duration or dimension associated with these high values is too small to account for seismic observations. In the second case, we have the velocity of 1 m/s and the acceleration of 1 g, which are acceptable values (Brune, 1970; Cloud and Perez, 1971). The associated time scale t_M of 0.1 second is also reasonable in view of the observed strong motion spectra.

The results for $\dot{u}_M$ and $\ddot{u}_M$ in the second case agree with similar estimates made by Brune (1970). It is emphasized, however, that the physical bases for the estimation are distinclly different in the two studies. In our treatment, the maximum particle motion is determined by the material property concerning the strength against fracture, while the particle velocity or acceleration is governed by the ambient effective tectonic stress in Brune's model. In addition, the predominant frequency of 10 cycles is arbitrarily assumed in Brune's estimate, but it was obtained in our study. Finally, our treatment is applicable to subsonic rupture propagation, while Brune's estimate is valid for a supersonic propagation which is not realistic for a

spontaneous rupture (Ida and Aki, 1972).

The result in Table 3 suggests that maximum seismic motion may not be directly related to atomic bonding, but rather governed by the bulk strength of rocks. The values of σ_o and D_o in the second case yield the specific surface energy of 10^{10} erg/cm^2, which is much larger than the laboratory measurements 10^3 erg/cm^2 for rocks (Brace and Walsh, 1962). Such a large value of the specific surface energy for an earthquake was also obtained independently from the information on the time during which the rupture velocity approaches the upper limit (Kikuchi and Takeuchi, 1970). This problem should be examined more carefully because of the importance of specific surface energy in the fracture phenomena.

The factor C specified by (6) is neglected in the approximate relations (22) and (23). This assumption is valid, unless the rupture velocity c is close to the critical sound velocity, i.e., the shear-wave velocity for the longitudinal-shear crack and the Rayleigh wave velocity for the plane shear or tensile cracks. In many cases, the observed rupture velocity appears to be substantially smaller than the critical value (see Table 3 in Abe, 1972), even for deep-focus earthquakes (Fukao, 1972). In such cases, our rough estimation of $\dot{u}_M$ and

$\dot{u}_M$ is not influenced very much, even if the factor C is taken into account. According to a theoreticla calculation of dynamic crack propagation, the rupture velocity approaches the critical sound velocity (Kostrov, 1966). One possible explanation of the discrepancy between theory and observation is given by the dependence of $\dot{u}$ on c. According to (9), $\dot{u}$ should be infinitely large if c were the critical sound velocity. This suggests that the energy loss associated with $\dot{u}$, such as heat generation,would be enormous at the critical sound velocity, and that c is not easily increased unless such enormous energy is supplied. In other words, it is expected that the theory might give the correct observation of rupture velocity, if the energy dissipation is taden into account.

For the practical purpose, it is highly desirable to predict the ground motion in more detail for individual event. At present, uncertain knowledge of the cohesive force diagram prevents us from determining more accurate values of the coefficients in (9) to (12). Therfore better estimate cannot be made only by giving more suitable values for σ_o, D_o, μ and c. An expedent way to overcome this difficulty might be to regard these coefficients

as empirical parameters. It is another problem whether such large faulting as earthquake can be well described by the cohesive force diagram. Further theoretical and experimental studies are necessary to clarify this point.

ACKNOWLEDGMENTS

I would like to thank Dr. K. Aki for many useful suggestions. Drs. H. Kanamori and Y. Fukao read the manuscript and provided me with many helpful comments. This work was partially supported by the National Science Foundation under Grant GA 24268, and partially supported by the Advanced Research Projects Agency monitored by the Air Force Office of Scientific Research through contract F 44620-71-C-0049.

REFERENCES

Abe, K. (1972). Mechanisms and tectonic implications of the 1966 and 1970 Peru Earthquakes, Phys. Earth Planet. Interiors, 5, 367-379.

Barenblatt, G.I. (1959). The formation of equilibrium cracks during brittle fracture. General ideas and hypotheses. Axially-symmetric cracks, Appl. Math. Mech., 23, 622-636.

Brace, W.F. and J.B. Walsh (1962). Some direct measurements of the surface energy of quartz and orthoclase, Amer. Mineral., 47, 1111-1122.

Broberg, K.B. (1961). The propagation of a brittle crack, Arkiv Fysik, 18, 159-192.

Brune, J.N. (1970). Tectonic stress and the spectra of seismic shear waves from earthquakes, J. Geophys. Res., 75, 4997-5009.

Cloud, W.K. and V. Perez (1971). Unusual accelerograms recorded at Lima, Peru, Bull. Seism. Soc. Am., 61, 633-640.

Fukao, Y. (1972). Source process of a large deep-focus earthquake and its tectonic implications - The Western Brazil Earthquake of 1963, Phys. Earth Planet. Interiors, 5, 61-76.

Ida, Y. (1972). Cohesive force across the tip of a longitudinal-shear crack and Griffith's specific surface energy, J. Geophys. Res., 77, 3796-3805.

Ida, Y. and K. Aki (1972). Seismic source-time function of propagating longitudinal-shear cracks, J. Geophys. Res., 77, 2034-2044.

Kikuchi, M. and H. Takeuchi (1970). Unsteady propagation of longitudinal shear cracks (in Japanese), Zisin, 23, 304-312.

Kostrov, B.V. (1966). Unsteady propagation of longitudinal-shear cracks, Appl. Math. Mech., 30, 1241-1248.

Weertman, J. (1969). Dislocations in uniform motion on slip or climb planes having periodic force laws, in Mathematical Theory of Dislocations, ed. by T. Mura. American Society of Mechanical Engineers, New York, 178-202.

Yoffe, E.H. (1951). The moving Griffith crack, Phil. Mag., 42, 739-750,

TABLE 1

The maximum ϕ_M' of the normalized particle velocity $\phi'(X)$ on the fault plane for given models of cohesive force diagram $\sigma(\phi)$

Model	$\sigma(\phi)$*	γ	ϕ_M'	X_M
1	1	$1/2$	∞	4.0
2	$1-\phi$	$1/4$	0.683	1.4
3	$(1-\phi)^2$	$1/6$	0.909	0.5
4	$(1-\phi)(1+2\phi)$	$5/12$	0.693	2.7
5	$(1-\phi^2)^{1/2}$	$\pi/8$	0.712	2.9
6	$2(\phi+0.13)(\phi-1.37)^2$	0.405	0.581	6.4

* $\sigma(\phi) = 0$ for $\phi > 1$ in the models 1-5, and for $\phi > 1.37$ in model 6.

TABLE 2

The maximum values of the normalized particle velocity $\partial U/\partial X$ and acceleration $\partial^2 U/\partial X^2$ as a function of the distance X_2 from the fault plane for model 6

X_2	Max($\partial U/\partial X$)	Max($\partial^2 U/\partial X^2$)	Min($\partial^2 U/\partial X^2$)
0	0.290	0.16	-0.13
0.1	0.266	0.14	-0.10
0.5	0.212	0.085	-0.048
1.0	0.173	0.053	-0.024
5.0	0.0873	0.0087	-0.0028
10.0	0.0624	0.0033	-0.0010
50.0	0.0280	0.00031	-0.000091
100.0	0.0198	0.00011	-0.000032

TABLE 3

The maximum velocity $\dot{u}_M$ and acceleration $\ddot{u}_M$ for the assumed mechanisms of fracture

		1. Atomic Cohesion	2. Strength of Rocks
Assumed*	σ_o	1 Mbar	1 Kbar
	D_o	1 Å	10 cm
Obtained†	$\dot{u}_M$	10^5 cm/s	1 m/s
	$\ddot{u}_M$	10^{20} cm/s^2	1 g
	x_M	1 Å	0.1 km
	t_M	10^{-18} s	0.1 s

* $\mu \sim 1$ Mbar and $c \sim 1$ km/s are commonly assumed.

† Eqs. (22), (23), (24) and (25) are used.

FIGURE CAPTIONS

Fig. 1 The models of cohesive force diagram given by eq. (15), in which a = 2 and $\ell + \ell_1 = 1.5$ are assumed. The number attached to each curve denotes the value of ℓ.

Fig. 2. The distribution of $\phi'(X)$ for the models of cohesive force in Fig. 1. The number attached to each curve denotes the value of ℓ.

Fig. 3. The distribution of $\phi''(X)$ for the models of cohesive force in Fig. 1. The number attached to each curve denotes the value of ℓ.

Fig. 4. The normalized particle velocity $\partial U/\partial X$ at various distances X_2 from the fault plane. X may be regarded as the coordinate along the fault, or the time, referring to (4).

Fig. 5. The normalized particle acceleration $\partial^2 U/\partial X^2$ at various distances X_2 from the fault plane. X may be regarded as the coordinate along the fault, or the time, referring to (4).

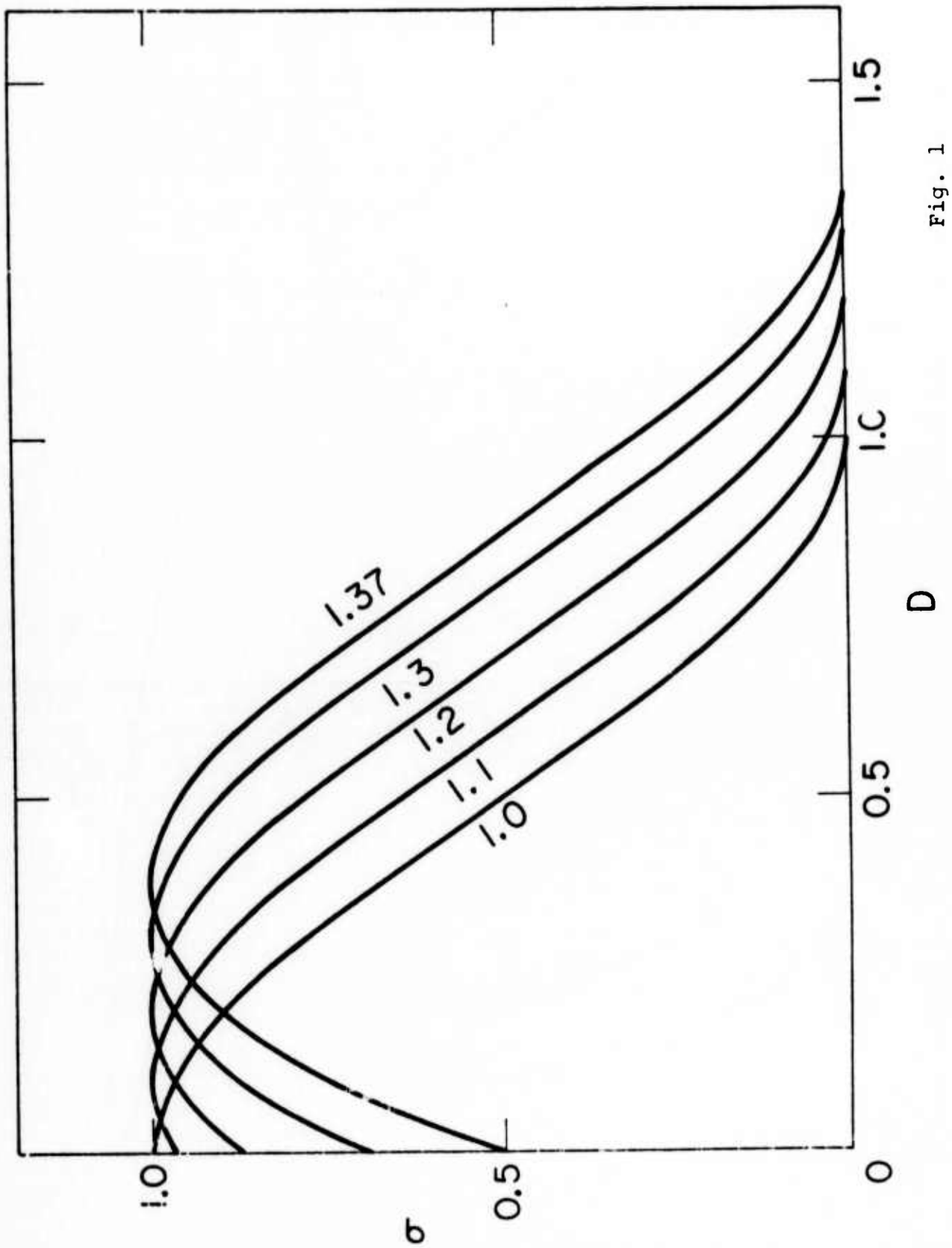

Fig. 1

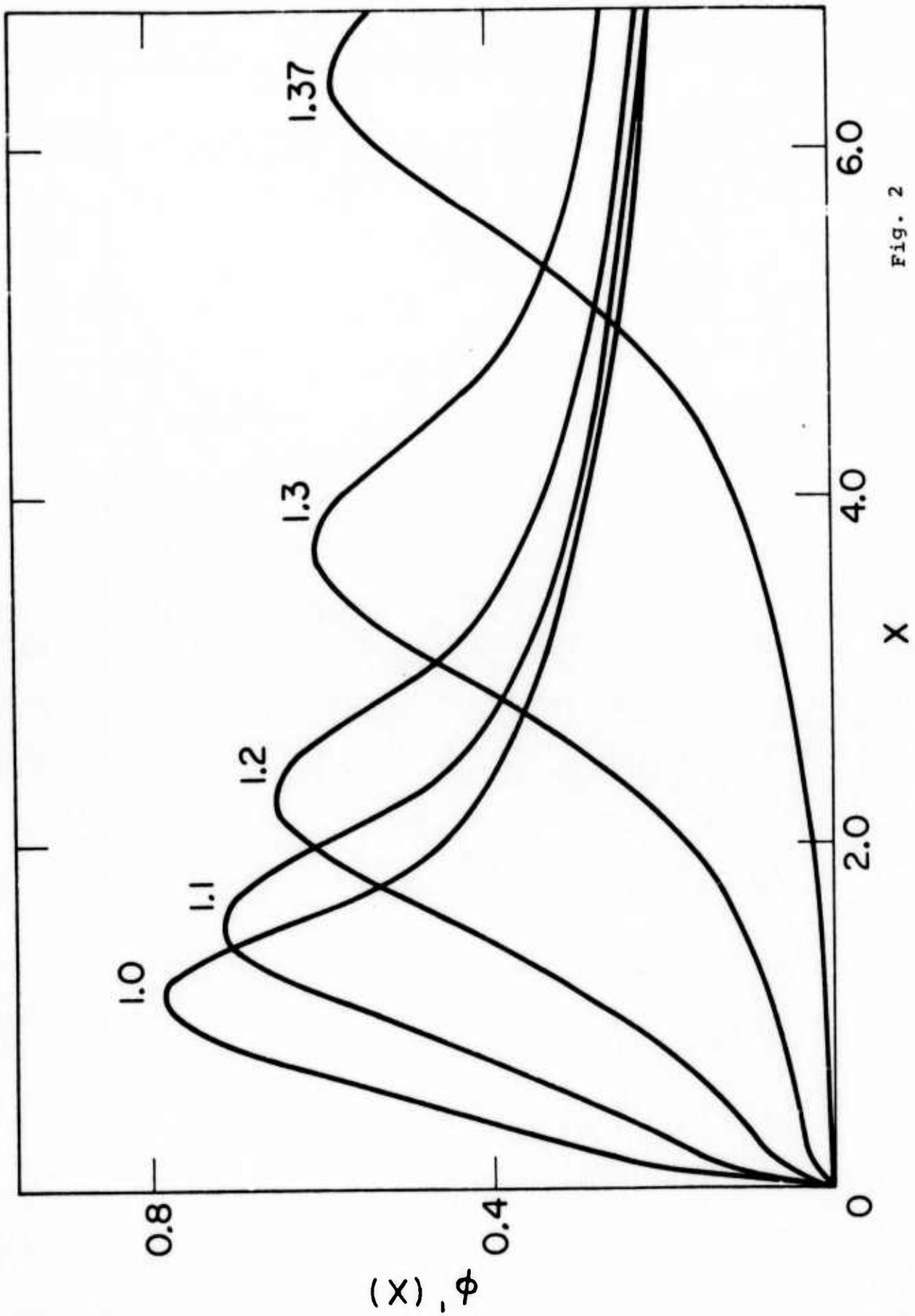

Fig. 2

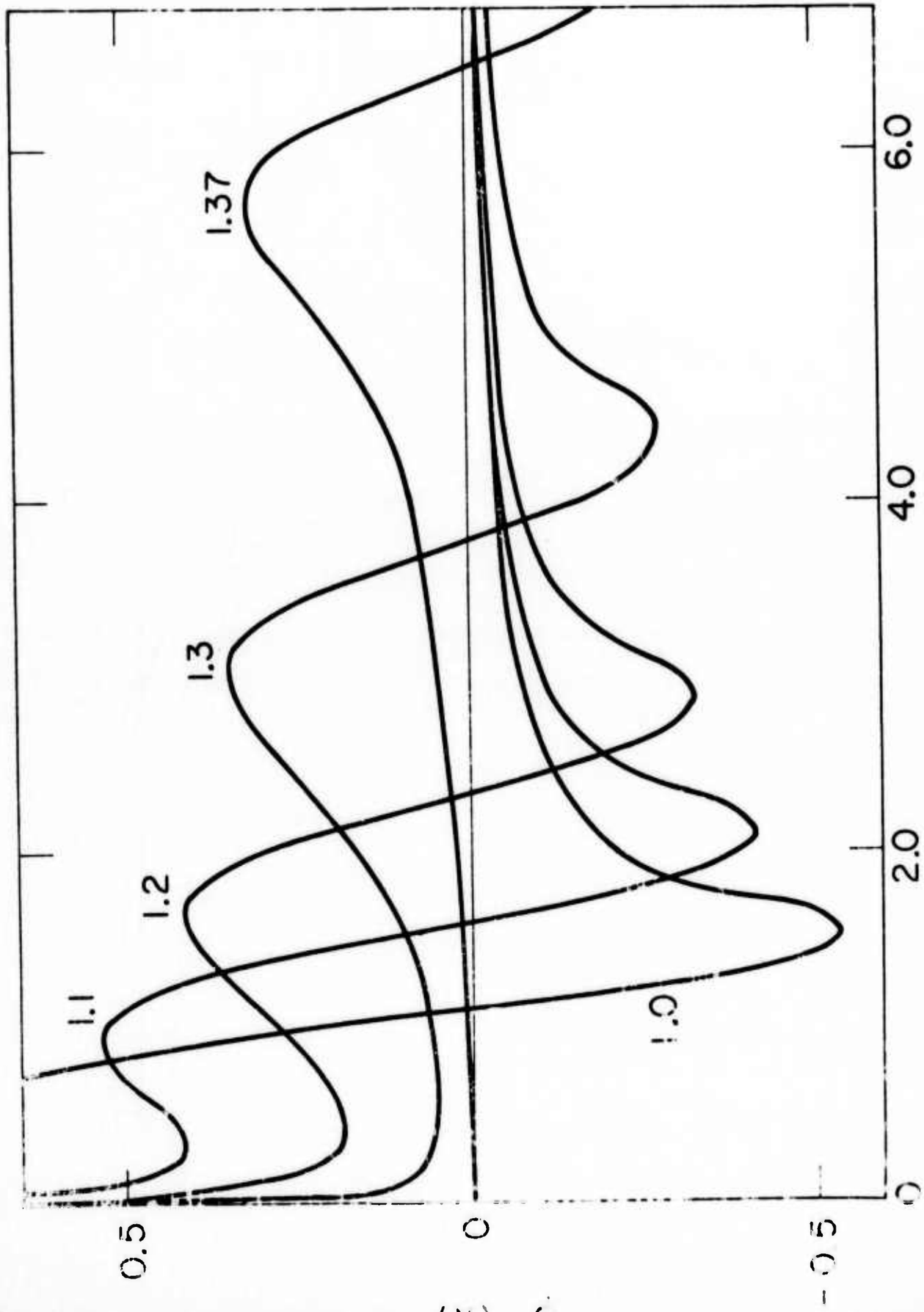

Fig. 3

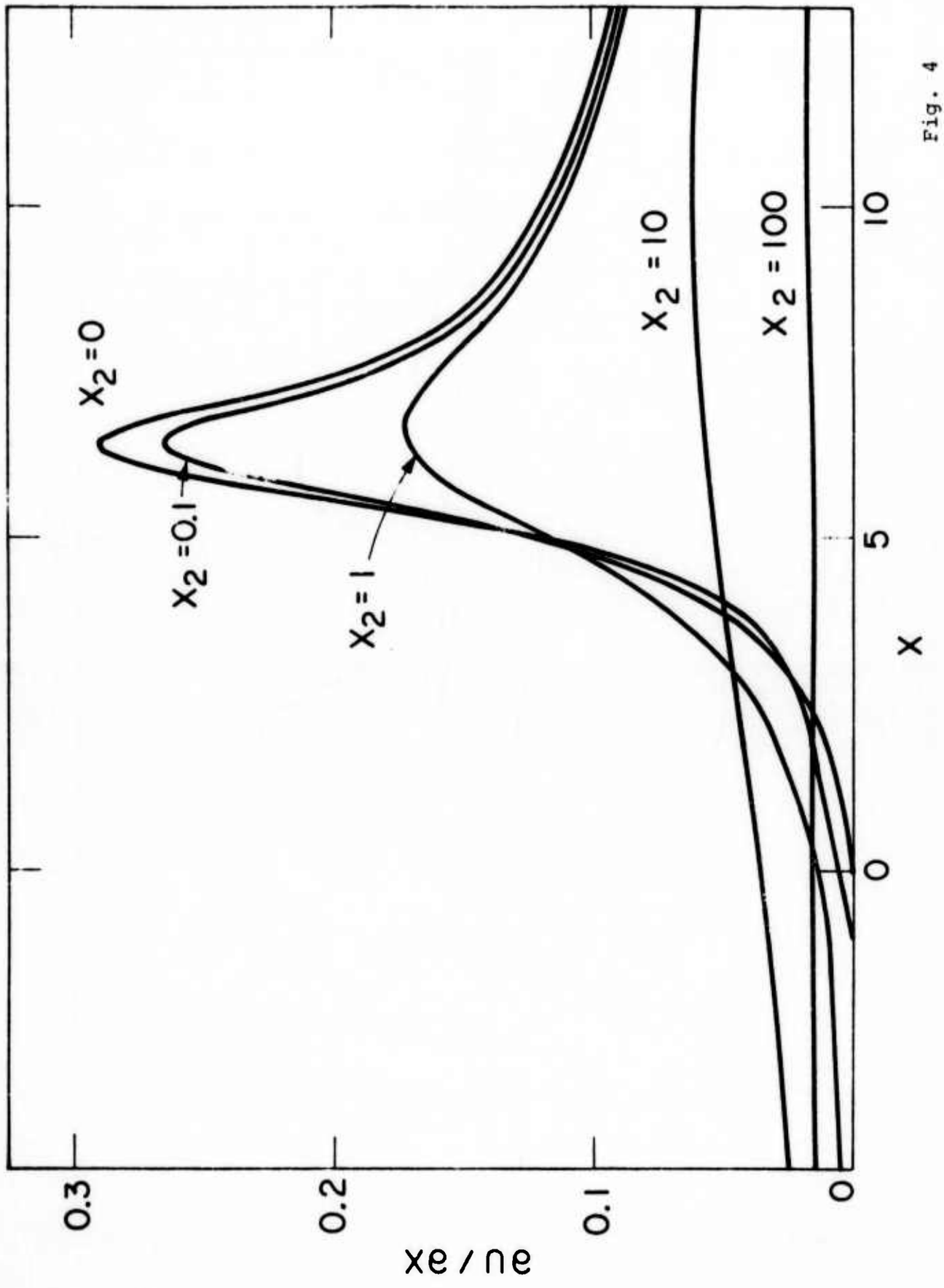

Fig. 4

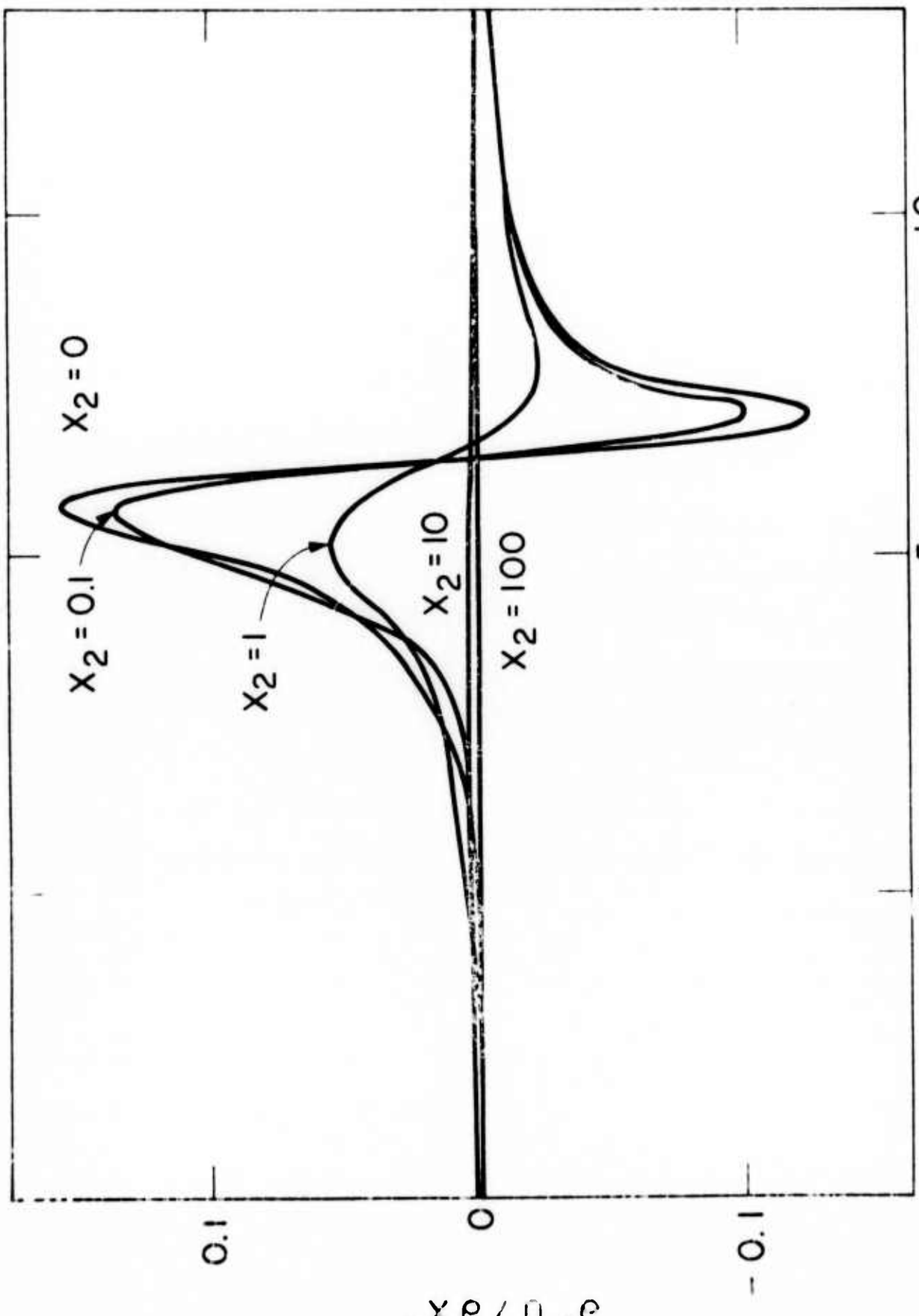

Fig. 5

2.4 Generation of SH-Type Motion by Torsion-Free Sources

by S.J. Singh

Summary

The problem of a spherical cavity in an infinite medium is re-examined. The spectral displacement and stress fields are derived when arbitrary tractions are prescribed over the surface of the cavity. This also yields the solution of the problem of the release of pre-existing stress within a spherical zone. The particular case when the radius of the cavity is small in comparison with the wavelength under consideration is discussed in detail. The nature of the tractions are obtained which, when applied at the surface of the cavity, yield the same displacement field as radiated by various point sources. Equivalent body forces are obtained for the release of pre-existing tensile and shear stresses within a spherical zone of small radius. In the course of the analysis, it is shown that an apparently torsion-free source is capable of generating SH-type motion.

INTRODUCTION

With regard to a given spherical polar coordinate system, the motion at a given point may be resolved into a toroidal part and a spheroidal part. For the toroidal part, the radial component of the displacement and the dilatation vanish identically. For the spheroidal part, the radial component of the curl of the displacement is zero. Suppose we shift the origin of the coordinate system along the polar axis. A motion which is of the toroidal type with respect to the old system will, in general, contain both the toroidal and the spheroidal parts with reference to the new system. This becomes obvious by observing that even if the radial component of the displacement vanishes in the old system, it may not vanish in the new system. However, if the motion has azimuthal symmetry, toroidal motion has only an azimuthal component while the azimuthal component of the spheroidal motion vanishes. In this special case, when the origin is shifted along the polar axis, the toroidal motion stays toroidal and the spheroidal motion stays spheroidal.

The realization of the above property is very important when considering the field radiated by a given source. It

shows that an apparently torsion-free source is capable of exciting SH-type motion.

SPHERICAL CAVITY IN AN INFINITE MEDIUM

Consider a homogeneous, isotropic, elastic medium of infinite extent containing a spherical cavity of radius a. Let the center of the cavity be the origin of a spherical polar coordinate system (R,Θ,ϕ). Our aim is to calculate the radiated field when the tractions are prescribed over the surface of the cavity. Since the motion must vanish at infinity, we assume the following expression for the displacement at any point of the medium

$$\vec{u} = \sum_{\nu=c,s} \sum_{\ell=1}^{\infty} \sum_{m=0}^{\ell} \left[\alpha^{\nu}_{m\ell} \vec{M}^{\nu}_{m\ell}(k_\beta R) + \beta^{\nu}_{m\ell} \vec{N}^{\nu}_{m\ell}(k_\beta R) + \gamma^{\nu}_{m\ell} \vec{L}^{\nu}_{m\ell}(k_\alpha R) \right] + \gamma^{c}_{00} \vec{L}^{c}_{00}(k_\alpha R), \qquad (1)$$

where $\alpha^{\nu}_{m\ell}$, etc., are arbitrary constants; $k_\alpha = \omega/\alpha$, $k_\beta = \omega/\beta$, ω being the angular frequency and α,β the wave velocities. $\vec{M}$, $\vec{N}$ and $\vec{L}$ are the solutions of the vector Navier equation. These may be expressed in the form

$$\vec{M}^{\nu}_{m\ell}(k_\beta R) = \operatorname{curl}\left[\vec{R}\, h_\ell(k_\beta R)\, Y^{\nu}_{m\ell}(\Theta,\phi)\right]$$

$$= \sqrt{\ell(\ell+1)}\, \vec{C}^{\nu}_{m\ell}(\Theta,\phi)\, h_\ell(k_\beta R), \qquad (2)$$

$$k_\beta \vec{N}^\nu_{m\ell}(k_\beta R) = \text{curl}\ \vec{M}^\nu_{m\ell}(k_\beta R)$$

$$= \ell(\ell+1)\ \vec{P}^\nu_{m\ell}(\Theta,\phi)\ h_\ell(k_\beta R)/R$$

$$+ \sqrt{\ell(\ell+1)}\ \vec{B}^\nu_{m\ell}(\Theta,\phi)\left(\frac{d}{dR} + \frac{1}{R}\right) h_\ell(k_\beta R), \quad (3)$$

$$k_\alpha \vec{L}^\nu_{m\ell}(k_\beta R) = \text{grad}[h_\ell(k_\alpha R)\ Y^\nu_{m\ell}(\Theta,\phi)]$$

$$= \vec{P}^\nu_{m\ell}(\Theta,\phi)\ \frac{d}{dR} h_\ell(k_\alpha R)$$

$$+ \sqrt{\ell(\ell+1)}\ \vec{B}^\nu_{m\ell}(\Theta,\phi)\ h_\ell(k_\alpha R)/R. \quad (4)$$

In (2) to (4), h_ℓ is the spherical Hankel function of the second kind and

$$Y^{c,s}_{m\ell}(\Theta,\phi) = P^m_\ell(\cos\Theta)(\cos m\phi, \sin m\phi),$$

$$\vec{P}_{m\ell}(\Theta,\phi) = \vec{e}_R\ Y_{m\ell}(\Theta,\phi), \quad (5)$$

$$\sqrt{\ell(\ell+1)}\ \vec{B}_{m\ell}(\Theta,\phi) = \left[\vec{e}_\Theta \frac{\partial}{\partial\Theta} + \vec{e}_\phi \frac{1}{\sin\Theta}\frac{\partial}{\partial\phi}\right] Y_{m\ell}(\Theta,\phi),$$

$$\sqrt{\ell(\ell+1)}\ \vec{C}_{m\ell}(\Theta,\phi) = \left[\vec{e}_\Theta \frac{1}{\sin\Theta}\frac{\partial}{\partial\phi} - \vec{e}_\phi \frac{\partial}{\partial\Theta}\right] Y_{m\ell}(\Theta,\phi).$$

The radial stress vector is given by

$$\vec{T}_R = \lambda \vec{e}_R\ \text{div}\ \vec{u} + \mu\left(2\frac{\partial \vec{u}}{\partial R} + \vec{e}_R \times \text{curl}\vec{u}\right), \quad (6)$$

where λ, μ are the Lamé parameters. Inserting for $\vec{u}$ from (1), we find (Ben-Menahem and Singh, 1968)

$$\vec{T}_R = \sum_{\nu=c,s} \sum_{\ell=1}^{\infty} \sum_{m=0}^{\ell} [\hat{\alpha}^{\nu}_{m\ell}(R)\sqrt{\ell(\ell+1)}\ \vec{C}^{\nu}_{m\ell}(\theta,\phi) + \hat{\beta}^{\nu}_{m\ell}(R)\vec{P}^{\nu}_{m\ell}(\theta,\phi) + \hat{\gamma}^{\nu}_{m\ell}(R)\sqrt{\ell(\ell+1)}\ \vec{B}^{\nu}_{m\ell}(\theta,\phi)] + \hat{\beta}^{c}_{00}(R)\vec{P}^{c}_{00}(\theta,\phi), \quad (7)$$

where

$$\begin{aligned}
\hat{\alpha}_{m\ell}(R) &= \mu k_\beta \eta\ F_{\ell,1}(\eta)\ \alpha_{m\ell}, \\
\hat{\beta}_{m\ell}(R) &= 2\mu[\ell(\ell+1)k_\beta F_{\ell,1}(\eta)\ \beta_{m\ell} + k_\alpha F_{\ell,3}(\xi)\gamma_{m\ell}], \quad (8) \\
\hat{\gamma}_{m\ell}(R) &= \mu[k_\beta F_{\ell,2}(\eta)\ \beta_{m\ell} + 2k_\alpha F_{\ell,1}(\xi)\ \gamma_{m\ell}],
\end{aligned}$$

with $\xi = k_\alpha R$, $\eta = k_\beta R$ and

$$\begin{aligned}
F_{\ell,1}(x) &= \frac{\ell-1}{x^2} h_\ell(x) - \frac{1}{x} h_{\ell+1}(x), \\
F_{\ell,2}(x) &= [\frac{2}{x^2}(\ell^2-1) - 1]\ h_\ell(x) + \frac{2}{x} h_{\ell+1}(x), \quad (9) \\
F_{\ell,3}(x) &= [\frac{1}{x^2}(\ell^2-1) - \frac{1}{2}(\frac{\alpha}{\beta})^2]\ h_\ell(x) + \frac{2}{x} h_{\ell+1}(x).
\end{aligned}$$

Let the tractions at the surface of the cavity be given by

$$\vec{T}_R = \vec{F}(\theta,\phi) \quad \text{at } R = a. \tag{10}$$

We expand $\vec{F}(\theta,\phi)$ in terms of the vector spherical harmonics:

$$\vec{F}(\theta,\phi) = \sum_{\nu=c,s} \sum_{\ell=1}^{\infty} \sum_{m=0}^{\ell} [a^{\nu}_{m\ell}\sqrt{\ell(\ell+1)}\ \vec{C}^{\nu}_{m\ell}(\theta,\phi) + b^{\nu}_{m\ell}\vec{P}^{\nu}_{m\ell}(\theta,\phi) + c^{\nu}_{m\ell}\sqrt{\ell(\ell+1)}\ \vec{B}^{\nu}_{m\ell}(\theta,\phi)] + b^{c}_{00}\vec{P}^{c}_{00}(\theta,\phi). \tag{11}$$

Given $\vec{F}(\theta,\phi)$, the expansion coefficients $a_{m\ell}$, etc., can be obtained with the help of the orthogonality relations for the vector spherical harmonics (Morse and Feshbach, 1953; p. 1900). Equations (7), (10) and (11) yield

$$\hat{\alpha}_{m\ell}(a) = a_{m\ell},\ \hat{\beta}_{m\ell}(a) = b_{m\ell},\ \hat{\gamma}_{m\ell}(a) = c_{m\ell}\ . \tag{12}$$

Putting R=a in (8) and using (12), we can find $\alpha_{m\ell}$, etc., in terms of the known expansion coefficients $a_{m\ell}$, etc. We get

$$\alpha_{m\ell} = a_{m\ell}/[\mu k_{\beta}\chi\ F_{\ell,1}(\chi)],$$

$$\beta_{m\ell} = \frac{1}{\mu k_\beta \Delta_\ell} [F_{\ell,1}(\zeta) b_{m\ell} - F_{\ell,3}(\zeta) c_{m\ell}], \qquad (13)$$

$$\gamma_{m\ell} = \frac{1}{2\mu k_\alpha \Delta_\ell} [2\ell(\ell+1) F_{\ell,1}(\chi) c_{m\ell} - F_{\ell,2}(\chi) b_{m\ell}],$$

where

$$\zeta = ak_\alpha, \quad \chi = ak_\beta, \text{ and}$$

$$\Delta_\ell = 2\ell(\ell+1) F_{\ell,1}(\zeta) F_{\ell,1}(\chi) - F_{\ell,2}(\chi) F_{\ell,3}(\zeta). \qquad (14)$$

This gives the formal solution of the problem of a spherical cavity in an unbounded medium when the tractions are prescribed over the surface of the cavity. An equivalent solution was obtained by Scholte (1962). However, due to the difference in notation, a comparison of the results seems difficult.

It is seen from (13) that the original problem splits into two independent problems, one with $b_{m\ell} = c_{m\ell} = 0$ and the other with $a_{m\ell} = 0$. The motion is of the toroidal type in the former case and of the spheroidal type in the latter case. We thus arrive at the conclusion that when the tractions are of the toroidal type, ensuing motion in a homogeneous, isotropic, unbounded medium is of the toroidal type. Similarly, spheroidal tractions lead to spheroidal motion.

At this point, it may be noted that when we talk about toroidal or spheroidal type field, we always have a spherical polar coordinate system in our minds. In the above case, it is the (R,Θ,ϕ) system with its origin at the center of the cavity. On the other hand, the toroidal and spheroidal motions measured at the surface of the earth ought to be with reference to a coordinate system having its origin at the center of the earth. The coordinates in the latter system are denoted by (r,θ,ϕ) as shown in Fig. 1. The two systems have the same polar axis and r_0 is the distance of the center of the cavity from the center of the earth. The important point to be observed is that, in general, a toroidal or spheroidal type motion with respect to the (R,Θ,ϕ) system corresponds to toroidal plus spheroidal type motion with respect to the (r,θ,ϕ) system. This becomes clear from the following transformations which express $\vec{M}$, $\vec{N}$ and $\vec{L}$ vectors in the (R,Θ,ϕ) system in terms of these vectors in the (r,θ,ϕ) system (Wason and Singh, 1971):

$$\vec{M}_{mn}(k_\beta R) = \sum_{\ell=m}^{\infty} \vec{M}_{m\ell}(k_\beta r) \left[E^{\ell}_{mn}(k_\beta r_0) - \frac{(\ell-m)k_\beta r_0}{\ell(2\ell-1)} E^{\ell-1}_{mn}(k_\beta r_0) - \frac{(\ell+m+1)k_\beta r_0}{(\ell+1)(2\ell+3)} E^{\ell+1}_{mn}(k_\beta r_0)\right]$$

$$- \sum_{\ell=m}^{\infty} \frac{k_\beta r_0}{\ell(\ell+1)} E^{\ell}_{mn}(k_\beta r_0) \vec{N}'_{m\ell}(k_\beta r), \qquad (15)$$

$$\vec{N}_{mn}(k_\beta R) = \sum_{\ell=m}^{\infty} \vec{N}_{m\ell}(k_\beta r)\ [E^{\ell}_{mn}(k_\beta r_0)$$

$$- \frac{(\ell-m)k_\beta r_0}{\ell(2\ell-1)} E^{\ell-1}_{mn}(k_\beta r_0) - \frac{(\ell+m+1)k_\beta r_0}{(\ell+1)(2\ell+3)} E^{\ell+1}_{mn}(k_\beta r_0)]$$

$$- \sum_{\ell=m}^{\infty} \frac{k_\beta r_0}{\ell(\ell+1)} E^{\ell}_{mn}(k_\beta r_0)\ \vec{M}'_{m\ell}(k_\beta r), \qquad (16)$$

$$\vec{L}_{mn}(k_\alpha R) = \sum_{\ell=m}^{\infty} E^{\ell}_{mn}(k_\alpha r_0)\ \vec{L}_{m\ell}(k_\alpha r), \qquad (17)$$

where $r > r_0$ and

$$\begin{aligned} \vec{M}'_{m\ell}(k_\beta r) &= \text{curl}[\vec{r}\ h_\ell(k_\beta r)\frac{\partial}{\partial\phi}Y_{m\ell}(\theta,\phi)], \\ k_\beta\ \vec{N}'_{m\ell}(k_\beta r) &= \text{curl}\ \vec{M}'_{m\ell}(k_\beta r). \end{aligned} \qquad (18)$$

Further, $\vec{M}_{m\ell}(k_\beta r)$, $\vec{N}_{m\ell}(k_\beta r)$ and $\vec{L}_{m\ell}(k_\alpha r)$ are obtained from $\vec{M}_{m\ell}(k_\beta R)$, $\vec{N}_{m\ell}(k_\beta R)$ and $\vec{L}_{m\ell}(k_\alpha R)$, respectively, by changing R to r and θ to θ. The function E^{ℓ}_{mn} is defined as

$$\begin{aligned} E^{\ell}_{m,m}(x) &= (2m-1)!!(2\ell+1)j_\ell(x)/x^m, \\ E^{\ell}_{m,m+1}(x) &= (2m+1)!!(2\ell+1)[(\ell-m)j_\ell(x)/x^{m+1} \\ &\qquad - j_{\ell+1}(x)/x^m], \qquad (19) \\ E^{\ell}_{m,m+2}(x) &= (2m+3)!!(2\ell+1)[\tfrac{1}{2}(\ell-m)(\ell-m-1)j_\ell(x)/x^{m+2} \\ &\quad + (m+1)\{j_{\ell+1}(x)/x^{m+1} - \frac{1}{2m+3}j_\ell(x)/x^m\}], \end{aligned}$$

where j_ℓ is the spherical Bessel function of the first kind and

$$(2m-1)!! = 1\cdot 3\cdot 5\cdot \ldots \cdot(2m-1);\ m \geq 1,\ (-1)!! = 1 .$$

Similar expressions can be obtained for other values of n. However, we will not need them here.

From (17) we note that an $\vec{L}$ vector in the (R,θ,ϕ) system transforms to a sum of $\vec{L}$ vectors in the (r,θ,ϕ) system. Similarly, if $m = 0$, a $\vec{M}$ or a $\vec{N}$ vector transforms to a sum of $\vec{M}$ or $\vec{N}$ vectors. However, if $m \neq 0$, i.e. if the motion is not symmetric about the polar axis, a $\vec{M}$ or a $\vec{N}$ vector in the (R,θ,ϕ) system transforms to a sum of $\vec{M}$ vectors plus a sum of $\vec{N}$ vectors in the (r,θ,ϕ) system. Therefore, a toroidal or a spheroidal motion in the (R,θ,ϕ) system has, in general, both the toroidal and spheroidal components in the (r,θ,ϕ) system.

Once the field has been expressed in the (r,θ,ϕ) system, the problem of satisfying the boundary conditions at the surface of the earth or any parallel boundary, r = constant, becomes straightforward. It can be easily seen that if the primary field is of the toroidal type the secondary field will also be of the toroidal type. Similarly, for a primary field of the spheroidal type we get a secondary field of the spheroidal type.

We may summarize the above discussion as follows. If the field due to a source with regard to the (R,θ,ϕ) system is axially symmetric and is of the toroidal or spheroidal type then the total field due to such a source in a radially heterogeneous earth will be of the toroidal or spheroidal type, respectively, even when referred to the (r,θ,ϕ) system. But if the field due to the source is not axially symmetric and is of the toroidal or spheroidal kind with regard to the (R,θ,ϕ) system, the total field when the source is placed in a radially heterogeneous earth has both the toroidal and spheroidal components with regard to the (r,θ,ϕ) system.

THE CASE OF SMALL CAVITY

We next assume that the radius of the cavity is small in comparison with the wavelength under consideration so that $\zeta << 1$, $\chi << 1$. We can then use the following expansion of the spherical Hankel function about the origin:

$$h_\ell(x) = \frac{1}{(2\ell+1)!!}\left[x^\ell - \frac{1}{2(2\ell+3)}x^{\ell+2} + \frac{1}{2.4(2\ell+3)(2\ell+5)}x^{\ell+4} + \ldots\right] + i(2\ell-1)!!\left[x^{-\ell-1} + \frac{1}{2(2\ell-1)}x^{-\ell+1} + \frac{1}{2.4(2\ell-1)(2\ell-3)}x^{-\ell+3} + \ldots\right]. \tag{20}$$

We shall be considering only such tractions as could be expressed in terms of the spherical harmonics of degree $\ell \leqslant 2$. Using (9), (13), (14) and (20), we obtain the following limiting values for $\alpha_{m\ell}$, etc. for $\ell \leqslant 2$ as ζ and χ tend to zero:

$$\gamma_{00} = -\frac{i}{4\mu} a^3 k_\alpha^2 b_{00}; \tag{21}$$

$$\alpha_{m,1} = \frac{i}{3\mu} a^3 k_\beta^2 a_{m,1},$$

$$\beta_{m,1} = \frac{2i}{3\mu} a^2 k_\beta (b_{m,1} + 2c_{m,1}), \tag{22}$$

$$\gamma_{m,1} = (\beta/\alpha)^3 \beta_{m,1};$$

$$\alpha_{m,2} = \frac{i}{12\mu} a^4 k_\beta{}^3 a_{m,2},$$

$$\beta_{m,2} = \frac{i}{\mu}\left[\frac{\lambda + 2\mu}{9\lambda + 14\mu}\right] a^3 k_\beta{}^2 (b_{m,2} + 3c_{m,2}), \tag{23}$$

$$\gamma_{m,2} = 2(\beta/\alpha)^4 \beta_{m,2}.$$

Inserting the above values in (1) and writing

$$\vec{u} = \sum_{\nu=c,s} \sum_{\ell=1}^{\infty} \sum_{m=0}^{\ell} \vec{u}^{\nu}_{m\ell} + \vec{u}^{c}_{00}, \tag{24}$$

we find

$$\vec{u}^{c}_{00} = -\frac{i}{4\mu} a^3 k_\alpha{}^2 b^c_{00} \vec{L}^{c}_{00}(k_\alpha R), \tag{25}$$

$$\vec{u}^{\nu}_{m,1} = \frac{i}{3\mu} a^3 k_\beta{}^2 a^\nu_{m,1} \vec{M}^{\nu}_{m,1}(k_\beta R)$$
$$+ \frac{2i}{3\mu} a^2 k_\beta (b^\nu_{m,1} + 2c^\nu_{m,1}) [\vec{N}^{\nu}_{m,1}(k_\beta R)$$
$$+ (\beta/\alpha)^3 \vec{L}^{\nu}_{m,1}(k_\alpha R)], \tag{26}$$

$$\vec{u}^{\nu}_{m,2} = \frac{i}{12\mu} a^4 k_\beta{}^3 a^\nu_{m,2} \vec{M}^{\nu}_{m,2}(k_\beta R)$$
$$+ \frac{i}{\mu}\frac{\lambda + 2\mu}{9\lambda + 14\mu} a^3 k_\beta{}^2 (b^\nu_{m,2} + 3c^\nu_{m,2})$$
$$\cdot [\vec{N}^{\nu}_{m,2}(k_\beta R) + 2(\beta/\alpha)^4 \vec{L}^{\nu}_{m,2}(k_\alpha R)]. \tag{27}$$

Equation (24) gives the displacement field in an unbounded medium containing a small spherical cavity, of radius a, the boundary of which has prescribed surface tractions $\vec{F}(\theta,\phi)$. Equations (25) to (27) are similar to the expressions for the displacement field due to various point sources situated in an infinite medium. We shall derive the relationship between the seismic moment of a point source and the tractions at the surface of the cavity so that the two yield identical radiations. It has been shown by Singh et al. (1972) that the displacement field due to a point source in a homogeneous, isotropic, infinite medium may be expressed in terms of the vectors $\vec{M}$, $\vec{N}$ and $\vec{L}$. In the following, the results for point sources have been taken from Table 3 of Singh et al. (1972).

(i) Center of compression

A center of compression is equivalent to three equal mutually perpendicular dipoles. The seismic moment of a dipole is defined as the product of the force and arm-length. The seismic moment of a center of compression may be defined as the seismic moment of any one of the component dipoles (Aki and Tsai,1972). Let the seismic moment of the center of compression be M_0. We then have

$$\vec{u} = \frac{iM_0 k_\beta^2}{4\pi\mu} \left(\frac{\beta}{\alpha}\right)^4 \vec{L}^C_{00}(k_\alpha R). \qquad (28)$$

Comparing (25) and (28), we find

$$b_{00}^{c} = -\frac{M_0}{\pi a^3}\left(\frac{\mu}{\lambda + 2\mu}\right). \tag{29}$$

It is obvious from (11) and (29) that, in this case, the surface traction is simply a pressure. The relation between the magnitude of the pressure, p_0, and the siesmic moment, M_0, of the equivalent center of compression is

$$M_0 = \pi a^3 p_0(\lambda + 2\mu)/\mu. \tag{30}$$

This relation has been given earlier by Aki and Tsai (1972).

(ii) Center of rotation

If the rotation is about the z-axis, we have

$$\vec{u} = -\frac{iM_0 k_\beta^2}{4\pi\mu}\vec{M}_{01}^{c}(k_\beta R). \tag{31}$$

Comparing with (26), we get

$$a_{01}^{c} = -\frac{3M_0}{4\pi a^3} \tag{32}$$

the rest of the coefficients being zero.

Equation (11) shows that, for a center of rotation about the z-axis, of seismic moment M_0,

$$\tau_{RR} = 0, \quad \tau_{R\theta} = 0, \quad \tau_{R\phi} = -\tau_0 \sin\theta,$$

where

$$M_0 = \frac{4}{3}\pi a^3 \tau_0.$$

(iii) Single couple

For a couple of moment M_0 in the xy-plane with its forces parallel to the x-axis,

$$\vec{u} = -\frac{iM_0 k_\beta^2}{48\pi\mu}[6\vec{M}^c_{01} + \vec{N}^s_{22} + 2(\frac{\beta}{\alpha})^4 \vec{L}^s_{22}]. \tag{33}$$

Comparing (26), (27) and (33), we obtain

$$a^c_{01} = \frac{3M_0}{8\pi a^3},$$

$$b^s_{22} + 3c^s_{22} = -\frac{M_0}{48\pi a^3}\left(\frac{9\lambda + 14\mu}{\lambda + 2\mu}\right). \tag{34}$$

If the forces of the couple are parallel to the y-axis, we have instead

$$\vec{u} = -\frac{iM_0 k_\beta^2}{48\pi\mu}[6\vec{M}^c_{01} + \vec{N}^s_{22} + 2(\frac{\beta}{\alpha})^4 \vec{L}^s_{22}]. \tag{35}$$

From (34), we get $b_{22} + 3c_{22}$, but not b_{22} and c_{22} separately. This implies that the solution is not unique. Corresponding to a given source, we can find more than one distribution of tractions over the surface of a small cavity which would yield the same radiations as the given source. This lack of uniqueness is obviously caused by the limiting process. For a cavity of radius which may not be small, we have seen in (7), (8) and (13) that a given displacement field gives a definite stress field on the surface of the cavity and, conversely, corresponding to a given distribution of stresses at the surface of the cavity, there is a definite unique displacement field.

(iv) Double couple

Defining a double couple of seismic moment M_0 in the xy-plane as the sum of the two single couples whose displacement fields are given by (33) and (35), we have

$$\vec{u} = -\frac{iM_0 k_\beta^2}{24\pi\mu}[\vec{N}^s_{22} + 2(\frac{\beta}{\alpha})^4 \vec{L}^s_{22}], \tag{36}$$

and

$$b^s_{22} + 3c^s_{22} = -\frac{M_0}{24\pi a^3}\left(\frac{9\lambda + 14\mu}{\lambda + 2\mu}\right). \tag{37}$$

(v) Dipole

For a dipole along the z-axis of seismic moment M_0

$$\vec{u} = -\frac{iM_0 k_\beta^2}{12\pi\mu}[\vec{N}^c_{02} - (\frac{\beta}{\alpha})^4(\vec{L}^c_{00} - 2\vec{L}^c_{02})]. \quad (38)$$

As before, we find

$$\begin{aligned} b^c_{00} &= -\frac{M_0}{3\pi a^3}\left(\frac{\mu}{\lambda + 2\mu}\right), \\ b^c_{02} + 3c^c_{02} &= -\frac{M_0}{12\pi a^3}\left(\frac{9\lambda + 14\mu}{\lambda + 2\mu}\right). \end{aligned} \quad (39)$$

However, if the dipole is along the x-axis, we have

$$\begin{aligned} \vec{u} = \frac{iM_0 k_\beta^2}{48\pi\mu}[&2\vec{N}^c_{02} - \vec{N}^c_{22} \\ &+ 2(\frac{\beta}{\alpha})^4(2\vec{L}^c_{00} + 2\vec{L}^c_{02} - \vec{L}^c_{22})]. \end{aligned} \quad (40)$$

For this case,

$$\begin{aligned} b^c_{00} &= -\frac{M_0}{3\pi a^3}\left(\frac{\mu}{\lambda + 2\mu}\right), \\ b^c_{02} + 3c^c_{02} &= \frac{M_0}{24\pi a^3}\left(\frac{9\lambda + 14\mu}{\lambda + 2\mu}\right), \\ b^c_{22} + 3c^c_{22} &= -\frac{M_0}{48\pi a^3}\left(\frac{9\lambda + 14\mu}{\lambda + 2\mu}\right). \end{aligned} \quad (41)$$

We have obtained above tractions or a set of tractions which when applied over the surface of a small cavity in an infinite medium give the same field as radiated by a point source in an infinite medium in the absence of the cavity.

RELEASE OF STRESS IN A SPHERICAL ZONE

Consider a homogeneous, isotropic, elastic, prestressed medium. Suppose that the stress is released within a spherical zone of radius a. Our aim is to calculate the additional displacement field caused by the release of the pre-existing stress. Denote the initial radial stress vector at any point by $\vec{T}_R^{\,0}$ and let

$$\vec{T}_R^{\,0} = -\vec{F}(\theta,\phi) \text{ at } R = a. \tag{42}$$

If the additional displacement field is expressed as in (1) and the corresponding stress vector as in (7), then we must have

$$\vec{T}_R + \vec{T}_R^{\,0} = 0 \text{ at } R = a. \tag{43}$$

Equations (42) and (43) yield

$$\vec{T}_R = -\vec{T}_R^{\,0} = \vec{F}(\theta,\phi) \text{ at } R = a. \tag{44}$$

Comparing (10) and (44) we note that the additional field due to the release of the stress in a spherical zone is identical with the field due to a spherical cavity in an infinite medium with prescribed surface tractions.

Consequently, we can use here the results derived before for a spherical cavity, including those for a cavity of small radius.

Consider the case in which the initial stress is a simple tension of magnitude τ_0 parallel to the axis of x. We have

$$\tau^0_{xx} = \tau_0, \quad \tau^0_{yy} = \tau^0_{zz} = \tau^0_{yz} = \tau^0_{zx} = \tau^0_{xy} = 0. \tag{45}$$

Equations (42) and (45) yield

$$\begin{aligned}
\vec{F}(\theta,\phi) &= -\vec{T}_R^{\,0} \\
&= -\tau_0(\vec{e}_R\cdot\vec{e}_x)\vec{e}_x \\
&= -\tau_0 \sin\theta\cos\phi\,(\sin\theta\cos\phi\,\vec{e}_R \\
&\quad + \cos\theta\cos\phi\,\vec{e}_\theta - \sin\phi\,\vec{e}_\phi) \\
&= -\frac{1}{6}\tau_0[2\vec{P}^c_{00} - 2\vec{P}^c_{02} + \vec{P}^c_{22} \\
&\quad - \sqrt{6}\,\vec{B}^c_{02} + \frac{1}{2}\sqrt{6}\,\vec{B}^c_{22}]
\end{aligned} \tag{46}$$

using (5). Comparing (11) and (46), we get

$$\begin{gathered}
b^c_{00} = -\frac{1}{3}\tau_0, \quad b^c_{02} = \frac{1}{3}\tau_0, \quad b^c_{22} = -\frac{1}{6}\tau_0, \\
c^c_{02} = \frac{1}{6}\tau_0, \qquad c^c_{22} = -\frac{1}{12}\tau_0.
\end{gathered} \tag{47}$$

The coefficients not mentioned are zero. Inserting into (13), one finds the coefficients $a_{m\ell}$, etc.

$$\begin{aligned}
\beta^c_{00} &= -\frac{\tau_0}{3\mu k_\beta \Delta_0} F_{0,1}(\zeta), \\
\beta^c_{02} &= \frac{\tau_0}{6\mu k_\beta \Delta_2}[2F_{2,1}(\zeta) - F_{2,3}(\zeta)], \\
\beta^c_{22} &= -\frac{1}{2}\beta^c_{02}, \\
\gamma^c_{00} &= \frac{\tau_0}{6\mu k_\alpha \Delta_0} F_{0,2}(\chi), \\
\gamma^c_{02} &= \frac{\tau_0}{6\mu k_\alpha \Delta_2}[6F_{2,1}(\chi) - F_{2,2}(\chi)], \\
\gamma^c_{22} &= -\frac{1}{2}\gamma^c_{02}.
\end{aligned} \tag{48}$$

Inserting into (1), we obtain the displacement field due to the stress release

$$\begin{aligned}
\vec{u} = {} & \beta^c_{02}(\vec{N}^c_{02} - \tfrac{1}{2}\vec{N}^c_{22}) + \gamma^c_{00}\vec{L}^c_{00} \\
& + \gamma^c_{02}(\vec{L}^c_{02} - \tfrac{1}{2}\vec{L}^c_{22}).
\end{aligned} \tag{49}$$

Once again, we consider the case when the radius of the spherical zone, a, is small in comparison with the wavelength of interest. Therefore, $\zeta << 1$, $\chi << 1$, and (9), (14), (20), and (48) yield

$$\beta_{02}^{c} = \frac{5i}{6\mu}\tau_0 k_\beta{}^2 a^3\left(\frac{\lambda + 2\mu}{9\lambda + 14\mu}\right),$$

$$\gamma_{00}^{c} = \frac{i}{12\mu}\tau_0 k_\alpha{}^2 a^3, \tag{50}$$

$$\gamma_{02}^{c} = 2\left(\frac{\beta}{\alpha}\right)^4 \beta_{02}^{c}.$$

Equation (49) now becomes

$$\vec{u} = \frac{5i}{12\mu}\tau_0 k_\beta{}^2 a^3\left(\frac{\lambda + 2\mu}{9\lambda + 14\mu}\right)[2\vec{N}_{02}^{c} - \vec{N}_{22}^{c} + 2\left(\frac{\beta}{\alpha}\right)^4\left\{\frac{1}{10}\left(\frac{9\lambda + 14\mu}{\mu}\right)\vec{L}_{00}^{c} + 2\vec{L}_{02}^{c} - \vec{L}_{22}^{c}\right\}]. \tag{51}$$

Comparing the last equation with (28) and (40), we note that the displacement field (51) is identical with the field due to a dipole in the x-direction of seismic moment

$$M_0 = 20\pi a^3 \tau_0\left(\frac{\lambda + 2\mu}{9\lambda + 14\mu}\right) \tag{52}$$

plus a center of compression of seismic moment

$$M_0 = \pi a^3 \tau_0 \frac{(\lambda + 2\mu)(3\lambda - 2\mu)}{\mu(9\lambda + 14\mu)}. \tag{53}$$

We thus see that the displacement field due to the release of a pre-existing stress, in the form of simple tension τ_0 parallel to the x-axis, within a small spherical zone, is identical with the displacement field due to a

tension dipole in the x-direction and a center of compression. Similarly, if the pre-existing stress is a simple pressure in the y-direction, the equivalent force system is a pressure dipole in the y-direction plus a center of dilatation. Combining the two results, we find that if the initial stress is a tension τ_0 in the x-direction plus a pressure τ_0 in the y-direction, the equivalent force system is a tension dipole in the x-direction together with a pressure dipole in the y-direction, each of seismic moment M_0 given by (52).

Suppose a new coordinate system (x',y',z') is obtained by rotating the (x,y,z) system about the z-axis through an angle $-\pi/4$. In that case

$$\begin{aligned} \vec{e}_{x'} &= (\vec{e}_x - \vec{e}_y)/\sqrt{2}, \\ \vec{e}_{y'} &= (\vec{e}_x + \vec{e}_y)/\sqrt{2}. \end{aligned} \tag{54}$$

This yields

$$\vec{e}_x\vec{e}_x - \vec{e}_y\vec{e}_y = \vec{e}_{x'}\vec{e}_{y'} + \vec{e}_{y'}\vec{e}_{x'}. \tag{55}$$

The last result shows that a tension τ_0 in the x-direction and a pressure τ_0 in the y-direction are equivalent to a shear τ_0 with reference to the x'y' directions. Further, we know that a tension dipole M_0 and a pressure dipole M_0

acting along mutually perpendicular directions are together equivalent to a double couple M_0. We, therefore, conclude that the displacement field due to the release of pre-existing shearing stress τ_0 within a small spherical zone of radius a is identical with the displacement field due to a double couple of seismic moment M_0, where

$$M_0 = 20\pi a^3 \tau_0 \left(\frac{\lambda + 2\mu}{9\lambda + 14\mu} \right). \tag{56}$$

This result could have been derived directly by assuming an initial stress of the form

$$\tau^0_{xy} = \tau_0, \quad \tau^0_{xx} = \tau^0_{yy} = \tau^0_{zz} = \tau^0_{yz} = \tau^0_{zx} = 0. \tag{57}$$

For the Poisson case ($\lambda = \mu$), (56) becomes

$$M_0 = \frac{60}{23} \pi a^3 \tau_0. \tag{58}$$

Equation (58) has been obtained earlier by Aki et al. (1969) and by Aki and Tsai (1972), beginning with the results of Honda (1960, 1962). Since Honda gives only the far-field displacements, Aki et al. (1969) and Aki and Tsai (1972) state that relation (58) holds only for the far-field. However, as we have seen above, the relationship applies for

the total exact-field. The only assumption is that the radius of the spherical zone is small, in comparison with the wavelength under consideration.

ACKNOWLEDGMENTS

Part of the work reported in this paper was done while the author was at the Weizmann Institute, Israel. The author is grateful to Professor Ari Ben-Menahem for helpful suggestions.

This research has been supported by the Advanced Research Projects Agency monitored by the Air Force Office of Scientific Research through contract F 44620-71-C-0049.

REFERENCES

Aki, K., P. Reasenberg, T. DeFazio, and Y.B. Tsai (1969). Near-field and far-field seismic evidences for triggering an earthquake by the Benham explosion, Bull. Seism. Soc. Am. 59, 2197-2207.

Aki, K. and Y.B. Tsai (1972). Mechanism of Love-Wave excitation by explosive sources, J. Geophys. Res. 77, 1452-1475.

Ben-Menahem, A. and S.J. Singh (1968). Eigenvector expansions of Green's dyads with applications to geophysical theory, Geophys. J. 16, 417-452.

Honda, H. (1960). The generation of seismic waves, Publ. Dominion Obs., Ottawa 24, 329-334.

Honda, H. (1962). Earthquake mechanism and seismic waves, J. Phys. Earth 10, No. 2, 1-97.

Morse, P.M. and H. Feshbach (1953). Methods of Theoretical Physics, McGraw-Hill, New York.

Scholte, J.G.J. (1962). The mechanism at the focus of an earthquake, Bull. Seism. Soc. Am. 52, 711-721.

Singh, S.J., A. Ben-Menahem, and M. Vered (1972). A unified approach to the representation of seismic sources (submitted for publication).

Wason, H.R. and S.J. Singh (1971). Transformation of earthquake displacement field for spherical earth, Bull. Seism. Soc. Am. 61, 289-295.

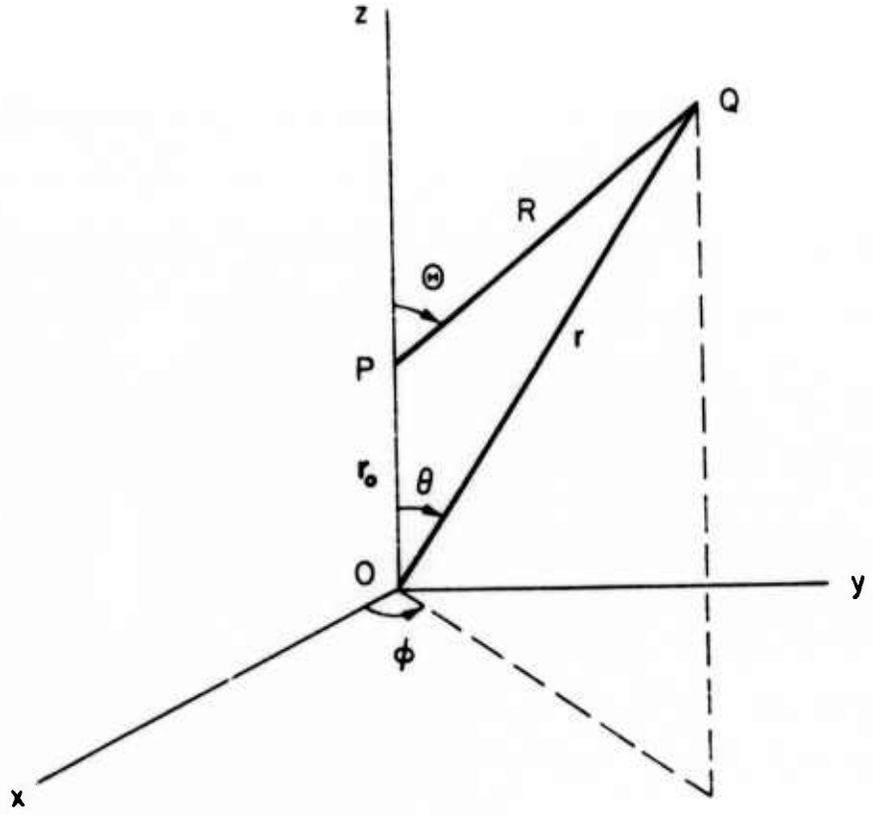
z
Q
R
Θ
r
P
r_o
θ
O
y
φ
x

2.5 On the Disturbance Due to a Spherical Distortional Pulse in an Elastic Medium by S.J. Singh and M. Rosenman*

(Abstract)

Theoretical expressions are derived for the displacement, velocity and stress in the time domain induced by an axially symmetric shearing stress applied at the inner surface of a spherical cavity in a homogeneous, isotropic, elastic medium of infinite extent. Theoretical seismograms are computed for a step source and for three sources with exponential decay in time. A satisfactory time-dependence of the source can be obtained by combining the step source with one or more exponentially decaying sources.

* Address: Department of Geology, Harvard University, Cambridge, Massachusetts.

2.6 A Spherical Cavity in a Micropolar Elastic Medium and Related Problems, by S.J. Singh (Abstract)

The problem of a spherical cavity in an infinite, linear, isotropic, micropolar elastic medium is considered. The spectral displacement and stress fields are obtained when arbitrary tractions and couples are prescribed over the surface of the cavity. It is found that, as in the elastic case, the original problem splits into two

independent problems corresponding to spheroidal and toroidal motions, respectively. In the case of purely radial static or dynamic displacements, there is no microrotation. The solutions of such micropolar elastic problems can be obtained from the corresponding elastic solutions on replacing μ by $\mu + \frac{1}{2}\kappa$. This correspondence principle is used to derive the micropolar-elastic solutions of several problems involving radial displacements only.

2.7 Quasi-Static Deformation of a Viscoelastic Half-Space by a Displacement Dislocation by S.H. Singh and M. Rosenman (Abstract)

The correspondence principle is used to get the Laplace transformed solution of the problem of the quasi-static deformation of a viscoelastic half-space by a shear displacement dislocation from the corresponding elastic results. The transformed solution is inverted for the Voigt and the Maxwell viscoelastic models. It is shown that, for a vertical dip-slip fault, the surface displacements for the viscoelastic case are identical with the elastic displacements. In the case of a vertical strike-slip fault, detailed numerical results are obtained for both a point source and a finite rectangular source. It is found that the results for the viscoelastic models differ significantly from the corresponding elastic results.

2.8 Quasi-Static Strains and Tilts Due to Faulting in a Viscoelastic Half-space by M. Rosenman and S.J. Singh

(Abstract)

Recently derived quasi-static surface displacements resulting from a finite rectangular vertical strike-slip fault in a viscoelastic half-space are used to derive the surface strains and tilts for both Voigt and Maxwell viscoelastic models. Contour maps are obtained for various strain and tilt components. The variation with time and epicentral distance is studied in some representative cases. Detailed numerical calculations reveal significant differences between the viscoelastic and the elastic results in the case of a vertical strike-slip fault. This contrasts with the results for a vertical dip-slip fault in a uniform half-space, where the surface strains and tilts for the viscoelastic and the elastic models are identical.

3. EARTH STRUCTURE AND PATH EFFECTS

3.1 Regionalized Earth Models from Linear Programming Methods by C.E. Johnson (Abstract)

This study is concerned with the development of possible models of the internal structure of the earth consistent with a given set of observed data. A two-stage linear programming procedure was used together with an assumed parameterization to obtain an explicit envelope of possible shear velocity and density values in the mantle and core. This envelope is determined separately for oceanic, shield, and tectonic regions of the upper mantle. The data used in this study consist of the mass and moment of inertia of the earth, periods of free oscillations, including recently available overtones, regionalized phase and group velocities of Rayleigh waves, and phase velocities of Love waves. The results constrain the variations of density and shear velocity in the lower mantle to within about 1.5% from the center of the envelope. The density just below the mantle-core boundary was found to lie between 9.79 and 9.86 grams/cc. A rigid core was needed to satisfy the overtone data with a shear velocity between 3.35 and 3.52 km/sec. The radius of the mantle-core boundary was found to lie between 3476.38 and 3486.42 kilometers. Excellent agreement

with recent travel time studies of body waves was found for shear velocity in the lower mantle and for the radius of the mantle-core boundary. Geophysical and petrological interpretations based on these results are discussed.

3.2 Range of Earth Structure Nonuniqueness Implied by Body Wave Observations by R.A. Wiggins, G.A. McMechan and M.N. Toksöz (Abstract)

The Herglotz-Wiechert integral for the direct inversion of ray parameter versus distance curves can be manipulated to find the envelope of all possible models consistent with geometrical body wave observations (travel time and ray parameter versus distance). Such an extremal inversion approach has been used to find the uncertainty bounds for the velocity structure in the mantle and core. We find, for example, that there is an uncertainty of ±40 km in the radius of the inner core boundary, ±18 km at the core-mantle boundary, and ±35 km at the 435-km transition zone. The velocity uncertainty is about ±0.08 km/sec for P and S waves in the lower mantle and about ±0.20 km/sec in the core. Experiments with various combinations of ray tapes in the core indicate that rather crude observations of SKKS-SKS travel times confine the range of possible

models far more dramatically than do the most precise estimates of PmKP travel times. Comparisons of results from extremal inversion and linearized perturbation inversions indicate that body wave behavior is too strongly nonlinear for linearized schemes to be effective for predicting uncertainty.

3.3 A Travel-Time Study Using Deep-Focus Earthquakes

by M.K. Sengupta (Abstract)

Revision of the Jeffreys-Bullen (J-B) tables has been made from the analysis of travel-times of deep earthquakes. Deep events (450 to 600 km) were used in order to avoid the source bias caused by a downgoing slab. The absolute values of travel-times have been determined from the Nevada Test Site explosion data for which the upper mantle velocity structure near the source is known and could be corrected for.

In this analysis, station errors and the systematic error of the J-B tables are, in general, similar to other works. However, a smaller scattering of the data suggests that the results of this study may be more reliable. Prediction of travel-times from deep events, barring a d.c. term, could be made from our times and station corrections with an error comparable to the reading error.

Residual sphere plots of data suggest that anomalous, high velocity structures of the mantle beneath island arcs might exist even beyond the region of deep earthquakes (e.g., in the Solomon islands). Also, there is a suggestion of lateral heterogeneity at the deep mantle as evidenced from these plots and the anomalous travel-time variations between different source zones beyond 80° of distance. Stations in western North America were found to show different residuals for different source regions in different azimuths reflecting a complicated velocity structure underneath the stations.

3.4 Seismic Travel-Time Evidence for Lateral Inhomogeneity in the Deep Mantle by B.R. Julian and M.K. Sengupta (Abstract)

Regional variations in travel times at distances greater than about 70° have been found in a study of P waves from deep focus earthquakes. These data can be explained satisfactorily only in terms of large-scale lateral heterogeneity in the lowest few hundred km of the mantle, this region being more heterogenous than that which lies above it. The travel time varies by more than a second, indicating at least a 1% variation in the P wave velocity in the deep mantle. Among other results, the data indicate a pronounced lateral variation

beneath the Hawaiian islands, the velocities being high to the northwest of Hawaii and low in the vicinity of the islands. It also appears that low velocities may be characteristic of island arcs at depths greater than 1000 km.

3.5 Scattering of P Waves Under the Montana LASA

by K. Aki (Abstract)

The variations of amplitude and time-delay of teleseismic P waves across the Montana LASA were interpreted as due to scattering by a random inhomogeneity in the earth's crust under the array. The prediction of the Chernov theory explains well the observed statistical properties of P waves with frequency 0.5 cps. The inhomogeneity under LASA has a correlation distance of about 10 km, with a fractional RMS velocity fluctuation of 4%, extending to a depth of about 60 km. The turbidity coefficient under LASA at 0.5 cps is 0.008 km^{-1}, which is much greater than the values ($10^{-3} \sim 10^{-4} km^{-1}$ at 5 ~ 10 cps) observed for refracted waves in the crust and upper mantle in the U.S.S.R. by Nikolayev and his colleagues. The scattering under LASA is so strong that the condition for the Born approximation is violated for frequencies higher than 0.5 cps. Accordingly, the observed statistical properties of 1 cps waves show systematic departure from

the prediction of the Chernov theory.

3.6 Shear-Wave Attenuation and Melting Beneath the Mid-Atlantic Ridge by S.C. Solomon

Summary

Because the attenuation of seismic waves is sensitive to variations in temperature and to partial melting, the mapping of seismic Q beneath the mid-ocean ridge systems is a useful tool to outline boundaries between lithosphere and asthenosphere and to constrain the mechanics of the intrusion process. Our approach is to measure the differential attenuation of long-period shear waves, using a spectral ratio technique, from earthquakes on the ridge and to look for variations in attenuation with propagation direction. We correct for propagation distance and, where known, the upper mantle attenuation beneath the receiving stations.

The azimuthal dependence of attenuation of S waves from an earthquake offset from the ridge axis on a transform fault indicates the existence of a low-Q zone, no wider than 100 km and confined to depths shallower than about 100 to 150 km, beneath the crest of the mid-Atlantic ridge. The absence of appreciable azimuthal variation in shear-wave attenuation for an earthquake on the ridge crest suggests that the low-Q zone is at least 50 km wide.

Q within such a zone must be 10 or less for long-period S waves. The most likely explanation of such a low-Q zone of limited spatial extent and with sharply defined boundaries is that the zone is a region of extensive partial melting, probably at temperatures in excess of the anhydrous solidus of mantle material. Such a region of large melt concentration is consistent with the chemistry of rocks from the mid-ocean ridges and with models of the temperature field derived from numerical calculations of flow beneath spreading centers.

INTRODUCTION

The upper mantle beneath mid-ocean ridges and other spreading centers is anomalously hot, most likely because the ascending limb of some form of convection cell is centered more or less beneath the ridge axis. Portions of the mantle beneath a spreading ridge must further be partially molten, if for no other reason than to segregate the basaltic magmas needed to form the oceanic crust. High temperatures and partial melting can have a profound effect on the velocity of seismic-wave propagation and especially on the seismic attenuation or the quality factor Q. Beneath mid-ocean ridges, a zone of unusually low velocity and low Q extends approximately from the base of the crust [Le Pichon et al., 1965; Molnar and Oliver, 1969; Keen and Tramontini, 1970], at least in the immediate vicinity of the ridge crest, to several hundred kilometers depth [Francis, 1969; Knopoff et al., 1970; Weidner, 1972; Forsyth, 1972; Taylor, 1972]. This zone is commonly identified with a partially molten asthenosphere, whose accentuated features and shallow top are a consequence of the elevation of isotherms by convective upwelling.

Better quantitative information on the spatial variation

of Q beneath spreading mid-ocean ridges can therefore serve as a valuable constraint on the mantle temperature field and the process of lithosphere generation. While the most detailed such information will probably result from short-range refraction experiments using ocean-bottom sensors, we are limited at present to land-based observations. The approach in this paper will be to measure the amplitude spectra of long-period, teleseismic shear waves generated by earthquakes on a mid-ocean ridge, to look for changes in the differential attenuation of the waves with propagation direction, and to relate such changes to spatial variations of Q beneath the ridge. The most important result of this study is the striking evidence for a narrow, shallow region of very low Q lying beneath the crest of the mid-Atlantic ridge. This low-Q zone is clearly associated with melting, and probably represents the region in which temperatures exceed the dry solidus of mantle material.

SOURCE OF DATA

We shall present in this paper the differential attenuation of S waves from two earthquakes on the mid-Atlantic ridge. All data for this work are taken from recordings on

horizontal, long-period seismometers of the World-Wide Standard Seismograph Network. The mid-ocean ridge in the north Atlantic is an ideal spreading center to be studied using teleseismic body waves because of the excellent azimuthal coverage of standard stations. Pertinent information on the two earthquakes treated is given in Table 1. Their epicenters are shown superimposed on a seismicity map for the north Atlantic in Figure 1.

The earthquake of 2 June 1965 was located on the crest of the mid-Atlantic ridge. The focal mechanism is one of normal faulting, with the inferred tensional pre-stress axis approximately horizontal and perpendicular to the strike of the ridge [Sykes, 1970a]. We shall contrast below the attenuation of shear waves that have propagated more nearly parallel to the ridge axis with those that propagated roughly perpendicular to the axis. Of some note is the eastward offset in the ridge crest immediately to the south of the epicenter. Further mention will be made of this point later.

The earthquake of 13 February 1967 was located on the Gibbs fracture zone, a prominent transform fault that offsets two portions of the mid-Atlantic ridge crest by over 350 km [Fleming et al., 1970]. The focal mechanism derived from P-wave first motions is shown in Figure 2; clearly right-

lateral strike-slip motion on a nearly vertical fault is indicated. The strike of the east-west nodal plane is identical to the strike of the fracture zone [Fleming et al., 1970]. The earthquake epicenter is roughly 60 km east of the northern ridge crest segment. We shall pay particular attention below to the contrast in attenuation between shear waves that have propagated beneath the ridge crest and those that have traveled beneath the older ocean floor to the south. We might remark that the Gibbs fracture zone is somewhat unusual. It is actually a double fracture zone and apparently marks a boundary between regions with slightly different spreading directions [Fleming et al., 1970]. Added to the confusion is that spreading directions predicted for this region of the north Atlantic from Europe-North American spreading poles [Le Pichon, 1968; Chase, 1972] do not match the trend of the fracture zone, though these two determinations of spreading direction differ by 17 degrees and bracket the strike direction of the transform fault.

DIFFERENTIAL ATTENUATION

Background

A seismic signal contains information on both the source of the signal and the medium through which it has propagated. To isolate the effect of seismic attenuation, we appeal to the technique of body-wave equalization [Ben-Menahem et al., 1965], which has been used in assorted forms to study attenuation phenomena with a fair degree of success [Teng, 1968; Solomon and Toksöz, 1970; and several others].

The problem is simplified to a point source in an earth for which geometric ray theory and linear elasticity and anelasticity are valid. Then the observed amplitude spectrum of an isolated body wave from an earthquake may be written:

$$A(f) = S(f)\ R(\theta,\phi)\ A_p(f)\ A_I(f) \qquad (1)$$

where S is the amplitude spectrum at the source, R is the radiation pattern, a function of propagation direction (θ,ϕ), A_p is the transfer function for propagation through the earth and A_I is the transfer function for the instrument. By geometric ray theory we can factor $A_p(f)$ as follows:

$$A_p(f) = G \cdot \exp[-ft^*] \cdot \exp[-f\delta t^*] \qquad (2)$$

where G is a frequency-independent factor which accounts for geometrical spreading, and the remainder of the expression on the right-hand side of (2) accounts for attenuation.

The quantities t^* and δt^* are given by integrals of the reciprocal qualtiy factor over the ray path. We consider that Q^{-1} at any point within the earth can be written as a sum of some spherically symmetric model $Q_o^{-1}(r)$ and a residual term

$$Q^{-1}(\underline{r}) = Q_o^{-1}(r) + \delta Q^{-1}(\underline{r}) \ , \qquad (3)$$

a relationship valid for small losses. In general, all quantities in (3) may also depend on frequency. We then define

$$t^* = \pi \int_S Q_o^{-1}(s)\ v^{-1}(s)\ ds \qquad (4)$$

and

$$\delta t^* = \pi \int_S \delta Q^{-1}(s)\ v^{-1}(s)\ ds \qquad (5)$$

where ds is an increment of length along the ray path S. Equation (2) then follows from the definitions (4) and (5) as long as variations in v^{-1} are small compared to δQ^{-1}.

If the amplitude spectrum of a given body wave is measured at two stations, then the ratio of the spectra can be used to determine the difference in attenuation of the waves to the two respective stations. If

$$R_{12}(f) = \frac{A_1(f)}{A_2(f)}$$

then

$$\ln R_{12}(f) + f(t_1^* - t_2^*) - \ln[I_1(f)/I_2(f)] =$$

$$c_{12} + f(\delta t_2^* - \delta t_1^*) \qquad (6)$$

The left-hand side of (6) can be measured or calculated, and should vary roughly linearly with frequency if δt^* is a slowly-varying function of frequency. Thus the quantity $(\delta t_2^* - \delta t_1^*)$ may be determined by fitting a straight line to the left-hand side of (6). An example of such a measurement is shown in Figure 3. As a further check,

the intercept of such a straight line, given by the constant c_{12}, can be calculated from the source mechanism of the earthquake and a suitable velocity model for the earth.

By equation (5), the contributions to δt^* can arise from any portion of the ray path. It is expected, however, that δt^* will be controlled primarily by the upper mantle, in particular the asthenosphere, where values of Q^{-1} are known to be large and variable [Solomon, 1972a] and where seismic velocity and other physical properties also show lateral variation. This intuitive deduction receives support from the observation that station differences in δt^* for shear waves from deep-focus earthquakes do not generally depend on the source location [Solomon and Toksöz, 1970; Solomon, 1971]. For shallow sources, of course, the body waves to stations at teleseismic distances must pass through the asthenosphere twice. Only if the variation in upper mantle attenuation beneath the stations is known *a priori* or if the source is located in a region of unusually low Q can the near-source and near-receiver contributions to δt^* be separated with some confidence.

Discussion of Assumptions

Several of the assumptions made in the derivations of the previous section either are incorrect or restrict the permissible data set. The frequency range, .015 to .17 Hz, of the shear waves considered in this study includes frequencies too low for geometric ray theory strictly to apply and too high for the earthquakes indicated above to be regarded as point sources. Further, the possibility of contamination of the S wave by other phases should be examined. We discuss below the degree to which failure of these assumptions may affect our conclusions about seismic attenuation.

For propagation through the mantle, use of geometric ray theory is questionable probably only if the wave bottoms in the immediate vicinity of a transition zone, i.e. a sharp increase in velocity with depth. In this work we consider S waves which have traveled epicentral distances of 39 to 69 degrees or, alternatively, have bottomed in the mantle at depths of about 900 to 1800 km. Transition zones for shear-wave velocity at such depths in the mantle are not particularly well-documented, though second order discontinutities in $dt/d\Delta$ for S waves have been suggested to exist at $\Delta = 42°$ [Hales and Roberts, 1970a] and near $\Delta = 70°$ [Fairborn, 1969]. Presumably, determinations of δt^* obtained from waves at such distances should be used with care.

The amplitude spectrum of a body wave is distorted by passage through a layered crust. This distortion can be quite large for periods less than about 10 seconds; it is sensitive to crustal structure; and it tends to be worse for SV waves than for SH waves [Haskell, 1960, 1962; Ben-Menahem et al., 1965]. We have chosen not to correct shear wave spectra for station crustal response, primarily because of the large uncertainty in the velocity structure, particularly for shear waves, in the crust beneath most seismograph stations. A few attempts at correcting for the crust convinced us that the uncertainty in the correction term is comparable to the correction itself. Further, for a sufficiently wide frequency band the effect on spectral ratios of different station crustal responses is to introduce several peaks and troughs without appreciably altering the longer term trend as a function of frequency.

For shallow earthquakes, the body-wave amplitude spectrum will be multiplied by an additional transfer function because of the crust and free surface near the source. Earthquakes on the mid-ocean ridge system are known to be very shallow [Tsai, 1969; Weidner, 1972]; the depth of the 2 June 1965 event was constrained by Weidner [1972] to be only 3 ± 2 km. Further, the S waves reflected from the free surface will add

constructively to the direct S for both SV and SH components for the two earthquakes considered here. Thus the ratio of transfer functions associated with crustal structure at the source for stations at two somewhat different distances will be nearly unity.

A more serious complication to the measurement of δt^* is the finiteness of the earthquake source. The effects on the body-wave radiation pattern of rupture propagation on a fault plane of finite extent have been calculated for both the frequency and time domains [Ben-Menahem, 1962; Bollinger, 1968; Fukao, 1970]. These effects will significantly alter the body-wave amplitude spectra in the frequency range of interest here even for relatively small sources.

As a guide to the nature of the error in δt^* due to neglect of finite source dimensions, we computed the variation with azimuth of amplitude spectrum due to horizontal rupture propagation on a vertical fault [Ben-Menahem, 1962] and the resulting dependence on azimuth of the apparent differential attenuation obtained from the slope of the ratio of the amplitude spectrum at the given azimuth to the spectrum in the rupture direction. A uniform rupture velocity of 2 km/sec and fault lengths of 10, 20 and 30 km were used as representative values for mid-Atlantic ridge earthquakes of magnitude 5.5 to 6 [e.g. Udias, 1971]. A

constant horizontal phase velocity of 8 km/sec was used. This corresponds to an epicentral distance of about 50° for S waves from shallow events; the range in phase velocity for the distance range considered in this study is about 7.3 to 9.5 km/sec. Amplitude spectra were first smoothed by averaging over a moving window .02 Hz in width (see next section), and apparent differential attenuation was calculated for the frequency band .01 to .15 Hz. The values for δt^* thus determined are shown in Figure 4.

The effect of finiteness is to introduce troughs in the amplitude spectra at frequencies which depend on azimuth and on the difference in time of rupture at the two ends of the fault. As a result, there will be paired peaks and troughs in the spectral ratio, with the number of such features dependent on the fault length L and on the frequency band. For $L = 10$ km, the lowest-frequency trough is located at $f = .16$ Hz ($\phi = 180°$) to $f = .27$Hz ($\phi = 0°$). The spectral ratio used to calculate δt^* thus contains a single trough centered at a frequency above the highest frequency in the band. There is a large, azimuth-dependent variation in the apparent differential attenuation as a result. For $L \geq 20$ km, there is at least one trough-peak pair in each spectral ratio, so the azimuthal

variation of δt^* is less pronounced. In general, the effect of source finiteness on δt^* decreases as fault length increases and as higher frequencies are included in the frequency band [cf. Ward and Toksöz, 1971]. The lowest frequency trough is in the observed spectra from the event of 13 February 1967 generally occurs at a frequency in the range of .04 to .10 Hz and is azimuth-dependent, though there is considerable scatter. This is consistent with a fault length of 20 to 30 km, and indicates that the effect of finite source size on δt^* will probably be roughly as shown in Figure 4 for these values of L. For the 2 June 1965 event, the geometry is somewhat different, but the lowest-frequency troughs are at about the same or slightly higher frequencies than for the other earthquake.

It thus appears likely that finite source dimensions and rupture velocity will contribute a reasonably small ($\lesssim$ 6 sec) term, which varies smoothly with azimuth, to the apparent differential attenuation. If observed differences in δt^* are much larger than 6 sec or if there are large changes in δt^* with a small change in azimuth, then such observations cannot be ascribed to source effects but must reflect genuine variations in Q^{-1}.

The S waves included in this study were sufficiently well isolated from other body-wave arrivals (SS, ScS, SKS, etc.) so that the time window chosen for spectral analysis does not include these phases. A further potential complication is the contamination of long-period SV waves by S-coupled PL waves [Oliver, 1961]. From published phase and group velocity curves for fundamental-mode PL waves [Chander et al., 1968], we tested whether PL-wave contamination was likely for the epicentral distances, frequency bands, and time windows employed in our analysis of SV waves. With a few exceptions noted below, all involving epicentral distances less than 50° and predominantly oceanic paths, PL waves should not have affected SV-wave spectral amplitudes.

ATTENUATION MEASUREMENTS

Measurements of the differential attenuation of shear waves were made in the same fashion as in Solomon and Toksöz [1970]. Seismograms from horizontal components of the WWSSN were digitized at an interval of about 0.7 sec, rotated, and

bandpass filtered after mean and linear trend were removed. SV and SH components were Fourier transformed, and the amplitude spectra were smoothed by applying to each a moving-average window of width .02 Hz. The smoothed spectra were corrected for the instrumental response, using the theoretical formulas of Hagiwara [1958]. Spectral ratios were calculated, with a single reference station for each event, and were corrected for geometric spreading using travel-time distance relationships of Hales and Roberts [1970a] and for differences in δt^* (see equation 6) using the technique of Julian and Anderson [1968], with the velocity model SLUTD1 of Hales and Roberts [1970b] and a $Q_o^{-1}(r)$ model equal to Tsai and Aki's [1969] modification of model MM8 [Anderson et al., 1965]. The values of $\delta t_1^* - \delta t_2^*$ were then taken to be the negative of the slopes of the straight lines fit by least squares to the corrected spectral ratios.

In Table 2 are given the measured values of δt^* for shear waves from the transform-fault earthquake of 13 February 1967. Only the SH component was used, because the propagation directions of interest (within a few tens of degrees azimuth of the strike of the fracture zone) are near a maximum in the SH radiation pattern but near a nodal plane for SV. The list of stations included in the table is

exhaustive, in that it represents all WWSSN stations in the distance range 39° to about 70° that recorded clear S waves on both horizontal components. The first four stations in the table are in Europe or the Middle East, the next six are in South and Central America or in the Caribbean, and the last thirteen are in North America. The differential attenuation δt^*_{SH} is determined from the slope of the ratio of the amplitude spectrum at the station indicated to that at the reference station over the frequency band given at the bottom of the table. The frequency band is as wide as can be permitted by the requirement of a reasonable signal-to-noise ratio. At several stations with the highest values of δt^*, all shear-wave energy at frequencies above .15 Hz appears to have been removed (e.g. ALQ in Figure 3). The choice of reference station does not affect the relative values of δt^*, though it does influence the standard deviation of the straight-line fits to the spectral ratios. These standard deviations, also given in the table, are only lower bounds on the actual uncertainty in δt^*. Four of the stations lie very near to the SH nodal plane as predicted from Figure 2; values of δt^* for these stations are considerably less reliable than the others.

Note, from equation (6), that we can determine only differences in δt^* between stations. A constant could be added to all entries in the last column of Table 2 without altering any of the spectral ratios. The stations with larger values of δt^*, corresponding to greater attenuation δQ^{-1}, would, of course, remain as shown.

As a rough check on the validity of our interpretation of spectral slopes, we compared the intercept, c_{12} in equation (6), obtained by extrapolating the straight-line fit to $f = 0$, with the value expected from the radiation pattern and the differences in geometrical spreading for the paths from the source to the respective pair of stations. Except for the stations near a nodal plane, which all recorded amplitudes significantly larger than predicted from the radiation pattern, all values of c_{12} were within a factor of 3 of the predicted values and for half the stations were within a factor of 1.5. Considering the uncertainties in the corrections and the omission of ground motion amplification by local geology or topography, the agreement is fairly good and lends support to the analysis techniques adopted in this work.

Measured values of differential attenuation of shear waves for the ridge-crest earthquake of 2 June 1965 are given in Table 3. For this event only the SV component was used;

SV amplitudes at all but one of the stations in Table 3 are greater than SH amplitudes, and for more than half the stations the SV/SH amplitude ratio is 3 or more, a consequence of the S wave radiation pattern from a normal-faulting earthquake. As with the previous earthquake, the stations in Table 3 include all usable WWSSN records at stations in the distance range 40° to 70°. KTG and AKU are in Greenland and Iceland, respectively; the next eight are in Europe; SDB is in Africa; the next three are in South America; and the last nine are in North America. The time window and frequency band used are slightly different than for the previous event, because of both relatively more energy at higher frequencies and the need to minimize interference from the PL wave. At three stations, noted in the table, there may still be contamination from PL waves at the lowest frequencies in the passband.

We did not compare the intercepts of the straight-line fits to the spectral ratios with their expected values because no fault-plane solution that matched P-wave first motion [e.g. Sykes, 1970a] could fit the S-wave polarization, specifically the direction of first motion of the SH component. The problem lies in the standard projections used to map surface observations of first motion back onto the lower

focal hemisphere. Because of pronounced lateral velocity gradients beneath the ridge crest, body waves do not maintain a constant ray parameter along their path. Such lateral heterogeneity can also account for the apparent non-orthogonality of nodal planes frequently observed for normal faulting earthquakes on the ridge crest [e.g. Sykes, 1967, 1970a] and the discrepancy between focal mechanisms obtained from P-wave first motions and those determined from surface waves [Weidner, 1972]. This subject will be treated in more detail elsewhere [Solomon and Julian, 1973].

DISCUSSION AND INTERPRETATION

The important parameter controlling the differential attenuation measurements presented above, at least controlling the contribution to δt^* from heterogeneous Q^{-1} in the upper mantle near the mid-Atlantic ridge, is the azimuth at the source of the path to each station. This is illustrated in Figure 5, where we plot δt^*_{SH} versus azimuth for the Gibbs fracture zone earthquake of 13 February 1967. A constant (12.4 sec) has been subtracted from each of the

values of δt^* given in Table 2 so that the mean of all values is zero.

The important feature of Figure 5 is the band of very high values of δt^* between azimuths of 273° and 292° ± 2° azimuth. The two edges of this band are interpreted somewhat differently. The sharp increase in δt^* with increasing azimuth at 273° azimuth can be readily explained by noting that for larger azimuths the shear waves must propagate beneath the crest of the mid-Atlantic ridge while for lesser azimuths the waves pass under only older sea floor (see Figure 1). That the value of 273° azimuth does not correspond precisely with the fracture-zone strike or the local direction of plate divergence [Chase, 1972] should not be too disturbing in view of the uncertainties in all of these quantities. The conclusion is clear that Q^{-1} in the shallow mantle beneath the mid-Atlantic ridge is substantially higher than at comparable depths beneath sea-floor 25 to 30 million years old.

The decrease in δt^* with increasing azimuth near 292° azimuth was unexpected. The transition is sharp, and the values of differential attenuation for stations at azimuths of 294° to 330°, even though S waves to these stations must propagate beneath the ridge crest, are comparable to

values obtained at stations in the northeast and southwest quadrants, where S wave paths pass beneath only relatively old sea floor. We infer from this that there exists beneath the crest of the mid-Atlantic ridge a localized zone of very low Q. The boundaries of this zone must be very sharp. The shear waves leaving the fracture zone at azimuths in the range 273° to 292° pass through this low-Q zone, but S waves leaving the source at greater azimuths do not.

Some reasonably firm limits can be placed on the dimensions of the low-Q zone. As a working hypothesis we will treat this zone as a basically two-dimensional feature; i.e., one that is more or less continuous beneath the ridge axis, and that is disrupted only by offsets in the ridge crest. The distance between the ridge crest and the epicenter is an upper bound on the half-width of the low-Q zone, since clearly the earthquake lies outside the zone. The ISC and CGS epicenters place the earthquake, respectively, 60 and 70 km east of the ridge crest to the northwest. Probably the half-width of the low-Q zone is no more than about 50 km. Further the low-Q zone must be shallow. The S-waves leaving the earthquake at azimuths greater than 292° pass beneath the ridge axis at depths equal to or greater than 100 to 150 km, with the range in these depths being due to the

uncertainties in epicentral coordinates, source depth, and S-wave velocity model near the ridge. Thus the low-Q zone immediately beneath the ridge crest can extend no deeper than 100 to 150 km and must be shallower than this away from the crest.

From the approximate dimensions of the low-Q zone, we can estimate a lower bound on Q^{-1} necessary to give the observed difference in δt^*_{SH} of roughly 10 sec between S waves that did and did not pass through the zone. From equation (5) and an approximate path length of 100 km within the low-Q zone, we get $\delta Q^{-1} = .1$, or $Q = 10$ within the zone. This value of δQ^{-1} should be thought of as only a representative value for the frequency band used in this study, in view of the likely frequency dependence of Q in partially melted rock [Walsh, 1969; Solomon, 1972a]. Further, because the dimensions of the low-Q zone are only upper bounds and because the highly attenuated shear waves may not have passed through the full length of the zone, Q for S waves may be less than 10 within the zone. This is a very low value for Q, sufficiently low that the usual treatment of attenuation as a small perturbation to linear elasticity may break down.

It should be emphasized that the high values for δt^*

in Figure 5 are clearly due to attenuation in the upper mantle near the source and cannot be explained by other source or path effects. From Figure 4 and the discussion above, it may be readily seen that rupture propagation on a finite fault cannot produce an apparent differential attenuation that varies as rapidly with azimuth as does δt^* in Figure 5. Further, lateral variation of Q^{-1} in the upper mantle beneath the receivers cannot explain the observed pattern of δt^*. The stations of interest for this earthquake are all in North America, where the attenuation in the upper mantle has been well studied [Solomon and Toksöz, 1970]. Correcting the values of δt^* in Table 2 for the relative differences in upper-mantle attenuation, where known, beneath the respective stations does not change by a substantial amount the pattern of δt^* versus azimuth (see Figure 5). Of some note is that the station with the highest value of δt^* after these corrections is FLO, the nearest station to the epicenter in the azimuth band 270° to 290° and thus the station observing the S wave with the greatest angle of incidence at the source. Other bits of evidence supporting the low-Q zone are the shape of the S-wave spectra for waves which passed through the zone (the logarithm of the spectral amplitude density decreases smoothly and roughly linearly with frequency, as in Figure 3) and the

relatively large fraction of emergent arrivals in the northwest quadrant of the fault-plane solution in Figure 2.

Not all of the shear-wave spectra, we might note, decreased regularly with frequency as in Figure 3. At stations in the northeast and southwest quadrants, the spectra appeared to have the characteristic "corner frequency" at the value (.07 Hz) roughly appropriate to source dimensions of about 30 km [Brune, 1970], consistent with the considerations of "directivity" [Ben-Menahem, 1962] discussed above.

It is possible that properties peculiar to the Gibbs fracture zone, particularly if it is a leaky transform fault, may contribute to the pattern of attenuation given in Figure 5. The high value of δt^* at ATH would support such a notion, though this may just as reasonably be a near-receiver effect. The extent to which a shallow zone of very low Q is a universal feature of mid-oceanic ridges can be ascertained only by further observations.

The measured values of δt^*_{SV} for the ridge-crest earthquake of 2 June 1965 are plotted as a function of azimuth in Figure 6. Again, a constant value (0.9 sec) has been added before plotting to all of the values of δt^* in Table 3 so that the average value of δt^* for this data set is zero.

In at least the two northern quadrants of Figure 6,

there is a small azimuthal dependence for δt^*. The differential attenuation is higher by about 5 sec, on the average, for propagation paths more nearly parallel to the ridge axis (i.e. to European stations) than for paths perpendicular to the strike of the ridge (to North American stations). This could be explained if Q in the asthenosphere increases, or if a low-Q zone decreases in thickness, as a function of distance from the ridge crest.

For this earthquake, we cannot rule out explanations other than true anelastic losses for the pattern of δt^* in Figure 6. From Figure 4, for instance, the possibility that δt^* is controlled by the source must be admitted. Further, the difference in the distributions of Q^{-1} between the upper mantles of Europe and North America is not known. This probably will not provide an explanation for Figure 6, however, because most of the North American stations used are in western United States, where upper-mantle Q is anomalously low [Solomon and Toksöz, 1970; Solomon, 1972a]. Because Q in the upper mantle beneath most of Europe is likely at least as large as that under western U.S., the difference in δt^* between stations in the northeast and northwest quadrants would be accentuated if corrections for near-receiver attenuation were applied

to δt^* values at the European stations. A final complication is that the few data in the southern two quadrants do not mirror the pattern of the northern two, though this can be reasonably ascribed to the offset in the ridge crest south of the epicenter as noted earlier.

As an aside, it might be pointed out that three of the determinations of δt^* that appear most anomalous when compared with values at adjacent azimuths (ATH and SJG in Table 2 and Figure 5, MAL in Table 3 and Figure 6) are at stations about 42° from the epicenter. As noted earlier this epicentral distance may mark a discontinuity in the slope of the travel time curve, so that geometric ray theory may be inappropriate.

The main conclusion to be derived from Figure 6 is that there are no large variations with propagation direction of attenuation of shear waves from an earthquake on the ridge crest. Since our measurements reflect only differences in total attenuation, Figure 6 is still consistent with the evidence discussed above for a zone of very low Q beneath the ridge axis as long as all of the shear waves considered for this event passed through the zone. This requirement allows us to place a lower bound on the thickness of the zone. The bound will depend on the depth and on the velocity model near the source. For the stations closest to the

epicenter, the angle of incidence in the shallow mantle is 30° to 40° for any reasonable upper-mantle velocity model. This implies the half-width of the low-Q zone must be at least 50 to 60 km at 100 km depth or at least 25 to 30 km at half that depth. Since these values are comparable or only somewhat smaller than the upper bounds on the half-width of the low-Q zone derived earlier, the boundaries of the zone are fairly well constrained.

What phenomenon will give rise to a sharply defined zone of extremely low Q? The simplest explanation is that the high attenuation is associated with partial melting, as discussed in the introduction, and that the low-Q zone corresponds to a region where the melt phase occupies a relatively large fraction of the volume. A partially melted region beneath ridge crests has previously been predicted from models of convective upwelling beneath the ridge [Bott, 1965; Oxburgh and Turcotte, 1968; Wyllie, 1971; Forsyth and Press, 1971]. Wyllie [1967], in particular, emphasized the distinction between incipient melting, when temperatures lie above the solidus of mantle material partially saturated with water but below the anhydrous solidus and only a relatively small melt concentration is present, and "normal" or "dry" melting, when temperatures exceed the anhydrous solidus of mantle material and large quantities of melt are present.

From Wyllie's discussion and the extremely low Q present beneath the ridge crest, we identify the low-Q zone with a region of "dry" melting and the boundaries of the zone with the anhydrous solidus of mantle material.

Such an explanation is very plausible from the standpoint of current models for the temperature field in the mantle beneath mid-ocean ridges. In Figure 7 is shown such a temperature field, taken from a convection model of Andrews [1972] incorporating variable viscosity and a lithosphere-spreading half-rate of 1.2 cm/yr. From this temperature field and from the schematic phase diagram of Wyllie [1971] for peridotite in the presence of .1 percent water, the predicted regions of incipient and "dry" melting are as shown in Figure 7. Similar curves were also given by Wyllie and by Oxburgh and Turcotte [1968], both using the temperature field of the latter authors. The broad region of incipient melting corresponds to the normal oceanic asthenosphere, and the region of "dry" or "normal" melting is confined to depths less than 100 km.

Since the model of Andrews [1972] incorporated some arbitrary assumptions and simplifications and Wyllie's [1971] isopleth was not intended to be precise, it is not very meaningful to derive quantitative conclusions from

Figure 7. Nonetheless it is apparent that the region of large melt concentration is much wider in Figure 7 than the low-Q zone inferred above. This is also a feature of the diagrams of Oxburgh and Turcotte [1968] and of Wyllie [1971]. Andrews [personal communication, 1972] has noted that the temperature field scales approximately as the thermal gradient in the lithosphere, which is governed by the somewhat arbitrary values for normal oceanic heat flux and for thermal conductivity in the lithosphere. For instance, if the conductivity in the lithosphere is raised by 6 percent from the value used by Andrews, then the zone of "dry" melting shrinks to the shaded region of Figure 7, 50 km in half-width and shallower than 60 km in depth. Though the match of the dimensions of this region to those estimated for the zone of very low Q may be accidental, it nonetheless illustrates how meaurements of seismic attenuation can serve as useful constraints on models of mantle flow and temperature.

OTHER RELATED OBSERVATIONS

There have been a number of studies and observations which relate to the findings of this paper. All of them are more or less consistent with a shallow, narrow zone of low Q associated with partial melting at temperatures in excess of the dry solidus.

Molnar and Oliver [1969] noted that S_n waves which have propagated across mid-ocean ridge crests are always highly attenuated; but for S_n waves from fracture-zone earthquakes, paths not crossing the ridge often show efficient transmission. Their findings differed somewhat from ours in that some transform-fault earthquakes (including two on the Gibbs fracture zone) located further from the ridge crest than 60 to 70 km displayed inefficient S_n transmission for paths without ridge crossings. Such S_n transmission studies may not be directly correlatable with our work, however, for at least two reasons. The higher frequencies of S_n waves means that lower values of Q^{-1} are needed to damp out most of the energy; thus Molnar and Oliver's observations may bear more on the general elevation of the asthenosphere beneath mid-ocean ridges (see Figure 7) than on a more localized region of exceedingly low Q. Further, the apparent attenuation of S_n waves can

probably be markedly increased by negative velocity gradients with depth, associated with high thermal gradients, in the uppermost mantle [Hill, 1971].

From the apparent velocities of P waves recorded in Iceland from earthquakes on the mid-Atlantic ridge, Francis [1969] deduced that anomalously low velocities extend to 250 km depth in the mantle within 150 km of the ridge axis. Such a half-width and depth are greater than for the low-Q zone mentioned above, though this P-wave data may also primarily reflect lateral variations within the deeper asthenosphere or may merely indicate that the upper mantle beneath Iceland is different from other portions of the mid-Atlantic ridge.

The differential attenuation of shear waves from an earthquake on the crest of the mid-Arctic (Nansen) ridge was reported by Solomon and Toksöz [1970], though the number of data and the azimuthal coverage were more limited than in the present study. After correcting for differences in upper-mantle attenuation beneath the receivers, the values of Δt^* show a marked azimuthal dependence (Figure 8), possibly indicating a difference in Q^{-1} between the upper mantle beneath the oceanic segment of the ridge and that beneath the continental shelf or else unusually high Q^{-1} at several hundred kilometers depth beneath the Lomonosov ridge.

Ward and Toksöz [1971] made a pair of observations similar to those reported in this paper. They determined the difference in attenuation of P waves from two mid-Atlantic earthquakes recorded at the two seismic arrays LASA and NORSAR. For an event west of the ridge crest, the P wave which propagated beneath the ridge (to NORSAR) was more attenuated; while for a ridge-crest earthquake, the difference in attenuation at the two stations was not statistically significant. The former result does not bear directly on the proposed low-Q zone beneath the ridge, because the P wave to NORSAR passed under the ridge crest at about 450 km depth.

It has generally been noted that body-wave magnitudes of ridge crest earthquakes are often anomalously lower than values for earthquakes of comparable surface-wave magnitude located elsewhere [e.g. Solomon, 1972b]. Frequently, in fact, surface waves are observed from mid-ocean ridge earthquakes for which no body waves are detected [Marshall, 1970; Sykes, 1970b]. This phenomenon can readily be explained by a low-Q zone in the shallow mantle beneath ridges; the short-period body waves which pass through the zone are sharply attenuated but surface waves generated by the same earthquake are little affected. Francis and Porter [1972] recently reported some related observations. Two ocean-bottom seismometers 30 km apart, one in the median valley

of the mid-Atlantic ridge and one off the crest, recorded markedly different rates of microearthquake seismicity. The much lower rate of activity off the crest can be attributed to low Q immediately beneath the ridge axis. Francis and Porter also invoked low Q to explain why their seismometers did not record arrivals from several large earthquakes which occurred at relatively close range during the recording period.

Kay et al. [1970] have presented chemical evidence indicating that rocks at mid-ocean ridges are the product of extensive partial melting at shallow depths beneath ridge crests. They suggest that 30 percent melting at depths of 15 to 25 km is indicated. Certainly such large melt concentrations are consistent with and perhaps required by a Q for shear waves of less than 10, though most theoretical models of attenuation in partially melted rock [e.g. Walsh, 1969] break down for such large volume concentrations of the liquid phase. The melting model of Kay et al. has extensive melting confined to a narrow dike (less than 10 km wide), in disagreement with our observation that differential attenuation of shear waves from a ridge-crest earthquake shows no large dependence on propagation direction. The chemical data, however, do not preclude as much as 10 percent melting in the upper mantle at considerable distance from the ridge

crest [Kay et al., 1970]; such melt concentrations would still give rise, in all probability, to very low Q. That extensive melting may persist no deeper than 25 km beneath the ridge axis, as proposed by Kay et al., is not precluded by our attenuation measurements, though for the bottom of the low-Q zone to be so shallow would favor a larger value for the width of the zone, about 100 km, and would require even lower values of Q than discussed above.

CONCLUSIONS

There are pronounced lateral inhomogeneities in seismic attenuation beneath mid-ocean ridges. The variation with propagation direction of the attenuation of shear waves from an earthquake on the Gibbs fracture zone indicates the existence of a zone of very low Q, a zone no wider than about 100 km and no deeper than 100 to 150 km, beneath the axis of the mid-Atlantic ridge. That such a conclusion could be made is due to a fortuitous combination of features of this particular earthquake: (i) the event was offset from the ridge crest; (ii) the azimuthal directions from the source to the boundaries of the low-Q zone corresponded to a lobe

in the SH radiation pattern; (iii) this same range of azimuths included S wave paths to a relatively dense network of stations at appropriate distances; (iv) the upper-mantle attenuation beneath the stations was known. We might note that neither P nor SV waves from transform-fault earthquakes can be used to delineate the low-Q zone, because the direction along the fracture zone corresponds approximately to both P and SV nodal planes. There have been at most a handful of earthquakes on the mid-ocean ridge system in the last decade which satisfy all of the features listed. Such earthquakes merit considerable further study.

We observed little variation with propagation direction of attenuation of shear waves from an earthquake on the crest of the mid-Atlantic ridge, indicating that all waves have seen a similar Q environment. If the earthquake occurred over a shallow low-Q zone, a hypothesis strengthened by other anomalous properties of body-wave amplitudes from ridge-crest events, then such a zone is wider than about 50 km. Thus the combination of observations from the two earthquakes allows us to place reasonably tight constraints on the dimensions of the low-Q zone.

The very low values of Q (10 or less) within such a zone can most readily be explained as due to extensive partial melting, probably because convective upwelling beneath

the ridge axis has raised the peridotitic material of the upper mantle above its anhydrous solidus. Thus the boundaries of such a low-Q zone, when combined with phase diagrams of likely mantle materials, can serve as quantitative input to refine models of temperature and flow beneath mid-ocean ridges.

The Q model proposed in this paper for the shallow mantle beneath ridges can readily be tested by further experiments, the most fruitful of which are likely to be short-range seismic propagation studies near spreading centers using either natural or artificial sources and ocean-bottom sensors.

ACKNOWLEDGMENTS

I thank Joe Andrews, Bruce Julian, and Norman Sleep for helpful discussions.

This investigation was supported by the Advanced Research Projects Agency monitored by the Air Force Office of Scientific Research under contract F44620-71-C-0049.

REFERENCES

Anderson, D.L., A. Ben-Menahem, and C.B. Archambeau, Attenuation of seismic energy in the upper mantle, J. Geophys. Res., 70, 1441, 1965.

Andrews, D.J., Numerical simulation of sea-floor spreading, J. Geophys. Res., 77, 6470, 1972.

Ben-Menahem, A., Radiation of seismic body waves from a finite moving source in the earth, J. Geophys. Res., 67, 345, 1962.

Ben-Menahem, A., S.W. Smith, and T.L. Teng, A procedure for source studies from spectrums of long-period seismic body waves, Bull. Seismol. Soc. Amer., 55, 203, 1965.

Bollinger, G.A., Determination of earthquake fault parameters from long-period P waves, J. Geophys. Res., 73, 785, 1968.

Bott, M.H.P., Formation of oceanic ridges, Nature, 207, 840, 1965.

Brune, J.N., Tectonic stress and the spectra of seismic shear waves from earthquakes, J. Geophys. Res., 75, 4997, 1970.

Chander, R., L.E. Alsop, and J. Oliver, On the synthesis of shear-coupled PL waves, Bull. Seismol. Soc. Amer., 58, 1849, 1968.

Chase, C.G., The N plate problem of plate tectonics, Geophys. J. Roy. Astron. Soc., 29, 117, 1972.

Fairborn, J.W., Shear wave velocities in the lower mantle, Bull. Seismol. Soc. Amer., 59, 1983, 1969.

Fleming, H.S., N.Z. Cherkis, and J.R. Heirtzler, The Gibbs fracture zone: A double fracture zone at 52°30'N in the Atlantic ocean, Mar. Geophys. Res., 1, 37, 1970.

Forsyth, D.W., Rayleigh wave phase velocity variations in a regionalized Pacific (abstract), EOS, Trans. Amer. Geophys. Un., 53, 519, 1972.

Forsyth, D.W., and F. Press, Geophysical tests of petrological models of the spreading lithosphere, J. Geophys. Res., 76, 7963, 1971.

Francis, T.J.G., Upper mantle structure along the axis of the mid-Atlantic ridge near Iceland, Geophys. J. Roy. Astron. Soc., 17, 507, 1969.

Francis, T.J.G., and I.T. Porter, Microearthquake survey of the mid-Atlantic ridge, Nature, 240, 547, 1972.

Fukao, Y., Focal process of a deep-focus earthquake as deduced from long-period P and S waves, Bull. Earthquake Res. Inst., Univ. Tokyo, 48, 707, 1970.

Hagiwara, T., A note on the theory of the electromagnetic seismograph, Bull. Earthquake Res. Inst., Univ. Tokyo, 36, 139, 1958.

Hales, A.L., and J.L. Roberts, The travel times of S and SKS, Bull. Seismol. Soc. Amer., 60, 461, 1970a.

Hales, A.L., and J.L. Roberts, Shear velocities in the lower mantle and the radius of the core, Bull. Seismol. Soc. Amer., 60, 1427, 1970b.

Haskell, N.A., Crustal reflection of plane S_H waves, J. Geophys. Res., 65, 4147, 1960.

Haskell, N.A., Crustal reflection of plane P and SV waves, J. Geophys. Res., 67, 4751, 1962.

Herrin, E., Seismological tables for P, Bull. Seismol. Soc. Amer., 58, 1197, 1968.

Hill, D.P., Velocity gradients and anelasticity from crustal body wave amplitudes, J. Geophys. Res., 76, 3309, 1971.

Kay, R., N.J. Hubbard, and P.W. Gast, Chemical characteristics and origin of oceanic ridge volcanic rocks, J. Geophys. Res., 75, 1585, 1970.

Keen, C., and C. Tramontini, A seismic refraction survey on the mid-Atlantic ridge, Geophys. J. Roy. Astron. Soc., 20, 473, 1970.

Knopoff, L., J.W. Schlue, and F.A. Schwab, Phase velocities of Rayleigh waves across the east Pacific rise, Tectonophysics, 10, 321, 1970.

Le Pichon, X., Sea-floor spreading and continental drift, J. Geophys. Res., 73, 3661, 1968.

Le Pichon, X., R.E. Houtz. C.L. Drake, and J.E. Nafe, Crustal structure of the mid-ocean ridges, 1, Seismic refraction measurements, J. Geophys. Res., 70, 319, 1965.

Marshall, P.D., Aspects of the spectral differences between earthquakes and underground explosions, Geophys. J. Roy. Astron. Soc., 20, 397, 1970.

Molnar, P., and J. Oliver, Lateral variations of attenuation in the upper mantle and discontinuities in the lithosphere, J. Geophys. Res., 74, 2648, 1969.

Oliver, J., On the long-period character of shear waves, Bull. Seismol. Soc. Amer., 51, 1, 1961.

Oxburgh, E.R., and D.L. Turcotte, Mid-ocean ridges and geotherm distribution during mantle convection, J. Geophys. Res., 73, 2643, 1968.

Solomon, S.C., Seismic-wave attenuation and the state of the upper mantle, Ph.D. thesis, Mass. Institute of Technology, Cambridge, 321 pp., 1971.

Solomon, S.C., Seismic-wave attenuation and partial melting in the upper mantle of North America, J. Geophys. Res., 77, 1483, 1972a.

Solomon, S.C., On Q and seismic discrimination, Geophys. J. Roy. Astron. Soc., in press, 1972b.

Solomon, S.C., and B.R. Julian, Seismic constraints on ocean-ridge mantle structure, in preparation, 1973.

Solomon, S.C., and M.N. Toksöz, Lateral variation of attenuation of P and S waves beneath the United States, Bull. Seismol. Soc. Amer., 60, 819, 1970.

Sykes, L.R., Mechanism of earthquakes and nature of faulting on the mid-oceanic ridges, J. Geophys. Res., 72, 2131, 1967.

Sykes, L.R., Focal mechanism solutions for earthquakes along the world rift system, Bull. Seismol. Soc. Amer., 60, 1749, 1970a.

Sykes, L.R., Earthquake swarms and sea-floor spreading, J. Geophys. Res., 75, 6598, 1970b.

Taylor, R.W., Remote determinations of earth structure from relative event analysis with applications to the mid-Atlantic ridge, Ph.D. thesis, Penn. State Univ., University Park, Pa., 188 pp., 1972.

Teng, T.L., Attenuation of body waves and the Q structure of the mantle, J. Geophys. Res., 73, 2195, 1968.

Tsai, Y.B., Determination of focal depths of earthquakes in mid-oceanic ridges from amplitude spectra of surface waves, Ph.D. thesis, Mass. Inst. of Technology, Cambridge, 144 pp., 1969.

Tsai, Y.B., and K. Aki, Simultaneous determination of the seismic moment and attenuation of seismic surface waves, Bull. Seismol. Soc. Amer., 59, 275, 1969.

Udias, A., Source parameters of earthquakes from spectra of Rayleigh waves, Geophys. J. Roy. Astron. Soc., 22, 353, 1971.

Vogt, P.R., and N.A. Ostenso, Magnetic and gravity profiles across the Alpha cordillera and their relation to Arctic sea-floor spreading, J. Geophys. Res., 75, 4925, 1970.

Walsh, J.B., A new analysis of attenuation in partially melted rock, J. Geophys. Res., 74, 4333, 1969.

Ward, R.W., and M.N. Toksöz, Causes of regional variation of magnitudes, Bull. Seismol. Soc. Amer., 61, 649, 1971.

Weidner, D.J., Rayleigh waves from mid-ocean ridge earthquakes: source and path effects, Ph.D. thesis, Mass. Inst. of Technology, Cambridge, 256 pp., 1972.

Wyllie, P.J., Role of water in magma generation and initiation of diapiric uprise in the mantle, J. Geophys. Res., 76, 1328, 1971.

Table 1. Earthquake Source Parameters

Date	Origin Time			Latitude	Longitude	Depth	Magnitude
	h	m	s			km	m_b
2 June 1965	23	40	23.1	15.93°N	46.69°W	27	5.8
						3 ± 2[a]	
13 February 1967	23	14	22.3	52.82°N	34.25°W	17	5.6

Source of data: Bulletin of the International Seismological Centre

[a]From Rayleigh-wave phase spectra [Weidner, 1972].

Table 2. Differential attenuation of S waves from the earthquake of 13 February 1967.

Station	Azimuth degrees	Distance degrees	δt^*_{SH} sec
MSH	64	64.2	3.0 ± 1.6[a]
TAB	71	55.5	6.5 ± 1.0
JER	84	53.3	9.1 ± 1.1
ATH	87	42.2	20.2 ± 1.8
TRN	218	47.4	12.4 ± 1.0
CAR	224[b]	49.7	3.6 ± 1.2
SJG	228[b]	42.6	-0.5 ± 1.4
BOG	229[b]	58.1	10.4 ± 1.2
QUI	231[b]	64.4	10.5 ± 1.9
BHP	237	57.0	9.5 ± 1.3
ATL	262	40.4	12.3 ± 2.4
OXF	267	42.7	10.5 ± 2.3
JCT	272	51.8	14.1 ± 1.3
FLO	273	40.5	25.0 ± 1.5
LUB	276	50.9	19.2 ± 2.3
ALQ	281	52.7	22.1 ± 1.2
TUC	281	57.1	21.4 ± 2.6
DUG	290	52.9	27.6 ± 0.9
BOZ	294	48.8	12.4 ± 2.0
COR	300	55.7	9.1 ± 2.1
LON	301	53.5	7.9 ± 2.1
CMC[c]	324	39.5	0
COL	330	52.0	9.1 ± 1.8

[a] standard deviation of straight-line fit to spectral ratio

[b] near SH nodal plane Time window length: 58 ± 1 sec

[c] reference station Filter bandpass: .015 - .15 Hz

Table 3. Differential attenuation of S waves from the earthquake of 2 June 1965.

Station	Azimuth degrees	Distance degrees	δt^*_{SV} sec
KTG	10	56.5	-1.1 ± 1.4[a]
AKU	14	53.3	5.8 ± 2.1
KON[b]	29	59.6	0
ESK	30	51.5	1.0 ± 1.9
NUR	31	67.1	-2.2 ± 1.5
VAL[c]	31	46.1	4.0 ± 1.6
STU	41	55.9	7.1 ± 1.6
TRI	46	58.2	5.1 ± 2.0
TOL[c]	49	44.0	3.8 ± 1.8
MAL[c]	53	42.8	-10.9 ± 2.1
ATH	55	65.0	1.5 ± 2.6
SDB	114	67.0	8.6 ± 2.5
PEL	205	53.9	-7.7 ± 1.7
ANT	211	45.7	-4.3 ± 2.0
NNA	229	40.7	-3.8 ± 2.2
JCT	296	50.5	-2.6 ± 1.3
TUC	298	59.9	-1.0 ± 1.6
DAL	300	48.2	-7.1 ± 1.7
ALQ	302	56.4	-2.3 ± 0.9
OXF	304	42.5	-6.9 ± 3.8
BKS	305	69.1	-0.7 ± 1.5
BOZ	314	61.3	3.7 ± 1.4
MDS	316	45.6	-3.4 ± 2.6
AAM	317	41.1	-9.2 ± 2.5

[a] standard deviation of straight-line fit to spectral ratio

[b] reference station

[c] possible interference with oceanic PL waves

Time window length: 54 ± 1 sec; Filter bandpass: .028 - .175 Hz

FIGURE CAPTIONS

Fig. 1. Location of earthquakes considered in this study (large dots). Small dots are other epicenters on the mid-Atlantic ridge located by USCGS/NOAA for the years 1962-69. The small arrows denote the sense of relative movement of the adjoining plates for the event of 13 February 1967 and the inferred axis of maximum tension for the event of 2 June 1965 [Sykes, 1970a].

Fig. 2. Fault plane solution from P-wave first motions for the earthquake of 13 February 1967 (equal-area projection). Open circles are dilatations, closed circles are compressions, and crosses indicate proximity to a nodal plane. Smaller symbols are somewhat less reliable than the larger ones, due to lower signal-to-noise ratio or the emergent nature of the arrival. All data were read from long-period records of stations in the WWSSN or the Canadian network. The strike ϕ and dip δ of the nodal planes are also given. If the conversion from distance to

angle of incidence [Herrin, 1968; a velocity of 8 km/sec was assumed at the source] is correct, then ϕ and δ are determined to within about one degree; the actual uncertainty is probably larger.

Fig. 3. A representative determination of δt^*_S. Shown are the SH-wave amplitude spectra at stations ALQ and CMC (reference station), corrected for instrument response. Note the semi-log scale. For clarity, the ALQ spectrum (right-hand scale) has been shifted downward by a factor of 10 with respect to the CMC spectrum (upper left scale). The spectral ratio, corrected for the difference in epicentral distance between CMC and ALQ (including attenuation and geometric spreading) and for the source radiation pattern, is shown over a more limited frequency band. The differential attenuation is determined by a least-squares fit of a straight line to the spectral ratio; δt^* is the negative of the slope.

Fig. 4. The effect of source finiteness on measurements of δt^*_S. The central diagram is in polar

coordinates (r,ϕ), with r given by δt^* (see radial scale, in sec) and ϕ equal to the difference in azimuth between the rupture direction and the direction of shear-wave propagation. Amplitude spectra were calculated following Ben Menahem's [1962] relations for a vertical fault with horizontal rupture propagation, assuming flat source spectra for the equivalent point source and using a rupture velocity of 2 km/sec, an S-wave horizontal phase velocity of 8 km/sec, and the fault length L as indicated. Spectra, smoothed by averaging over a .02 Hz window, are shown in the insert for the three values of L at $\phi = 0$. The differential attenuation $\delta t^*_S(\phi)$ is calculated from the slope of the ratio of the amplitude spectrum at azimuth ϕ to that at $\phi = 0$ over the frequency band .01 to .15 Hz.

Fig. 5. Differential attenuation δt^* of SH waves from the Gibbs fracture zone earthquake. The plot is in polar coordinates (r,ϕ), with r given by δt^* (see radial scale, in sec) and ϕ equal to the azimuth of the respective ray path at the source.

Closed circles are the measured values from Table 2, with a uniform constant subtracted to give the data set zero mean. The error bars are the standard deviations from Table 2. Open circles are the measured values of δt^* corrected for differences in S-wave attenuation in the upper mantle beneath the receivers, where known [Solomon and Toksöz, 1970]. The strike of the fracture zone [Fleming et al., 1970], identical to the strike of the fault plane for this earthquake, and the local direction of plate divergence [Chase, 1972] are indicated by arrows.

Fig. 6. Differential attenuation δt^* of SV waves from the earthquake of 2 June 1965. Coordinates and symbols are as in Figure 5. The approximate strike of the ridge axis, taken from earthquake epicenters, and the local direction of plate divergence [Chase, 1972] are indicated by arrows.

Fig. 7. The shape of a zone of extensive melting beneath a mid-ocean ridge. The regions of incipient melting (temperatures between the water-saturated solidus and the anhydrous solidus) and of "dry"

melting (temperatures between the anhydrous solidus and the liquidus) are determined from the temperature-depth field in a mantle-convection model [Andrews, 1972] designed to simulate sea-floor spreading on the mid-Atlantic ridge and the schematic phase diagram of Wyllie [1971] for peridotite in the presence of .1 percent water. The stippled area is the region of "dry" melting if the thermal conductivity in the lithosphere is 6 percent greater than that used by Andrews (see text).

Fig. 8. Lateral variation of near-source attenuation for shear waves from the Arctic earthquake of 25 August 1964. The difference between δt^*_S determined at several North American stations and δt^*_S (S. Am.) determined from deep South American earthquakes recorded as the same stations is shown as a function of azimuth at the source at right. All data are from Solomon and Toksöz [1970]. The projections onto the earth's surface of several S-wave propagation paths to North America are indicated on a map of the Arctic region (Lambert equal-area projection) at left. The Lomonosov ridge is well-defined by the 2-km isobath [simplified from Vogt

and Ostenso, 1970] while the deeper mid-Arctic (Nansen) ridge follows the trend of earthquake epicenters (crosses; USCGS and NOAA determinations).

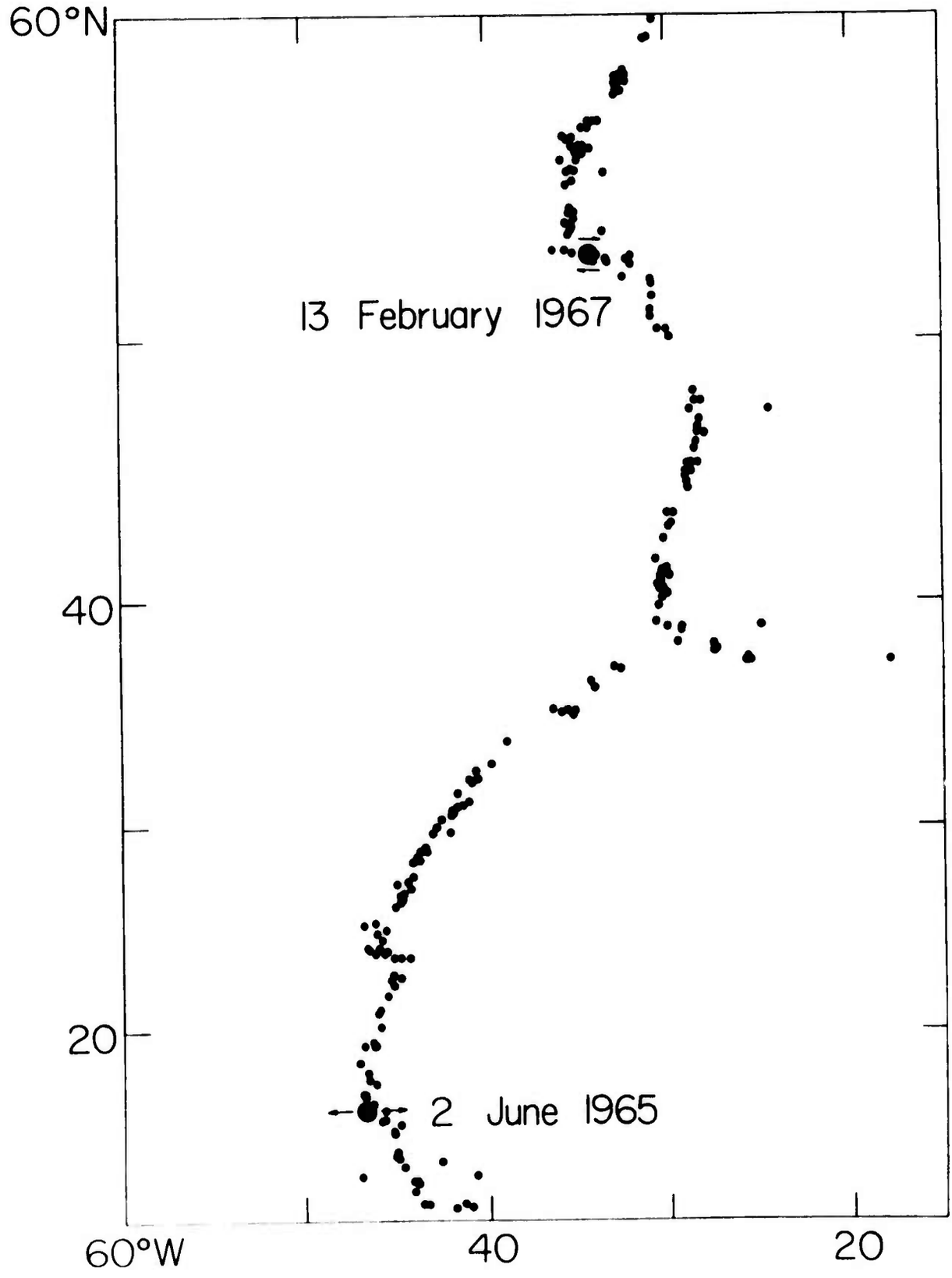

Figure 1

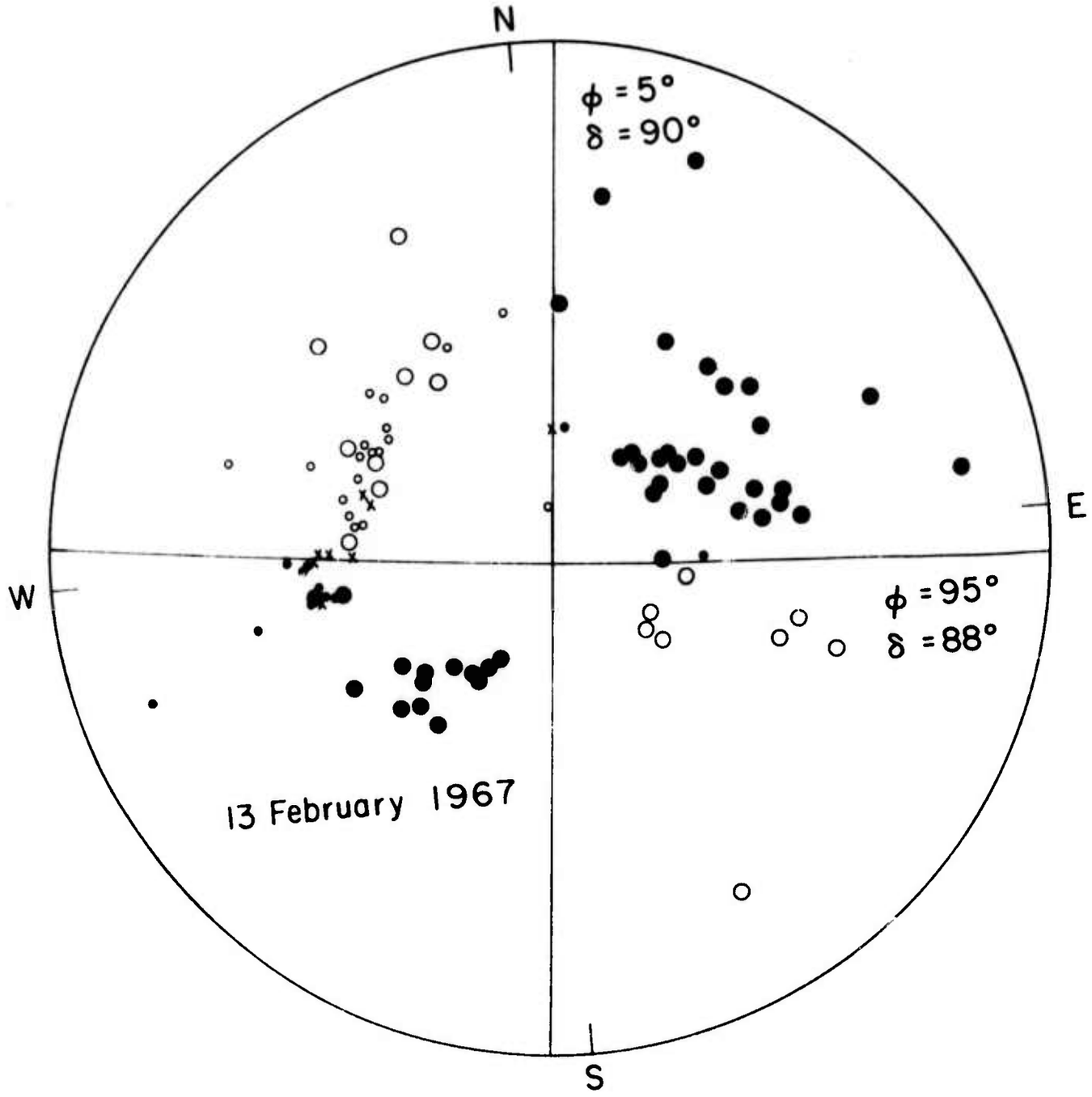

Figure 2

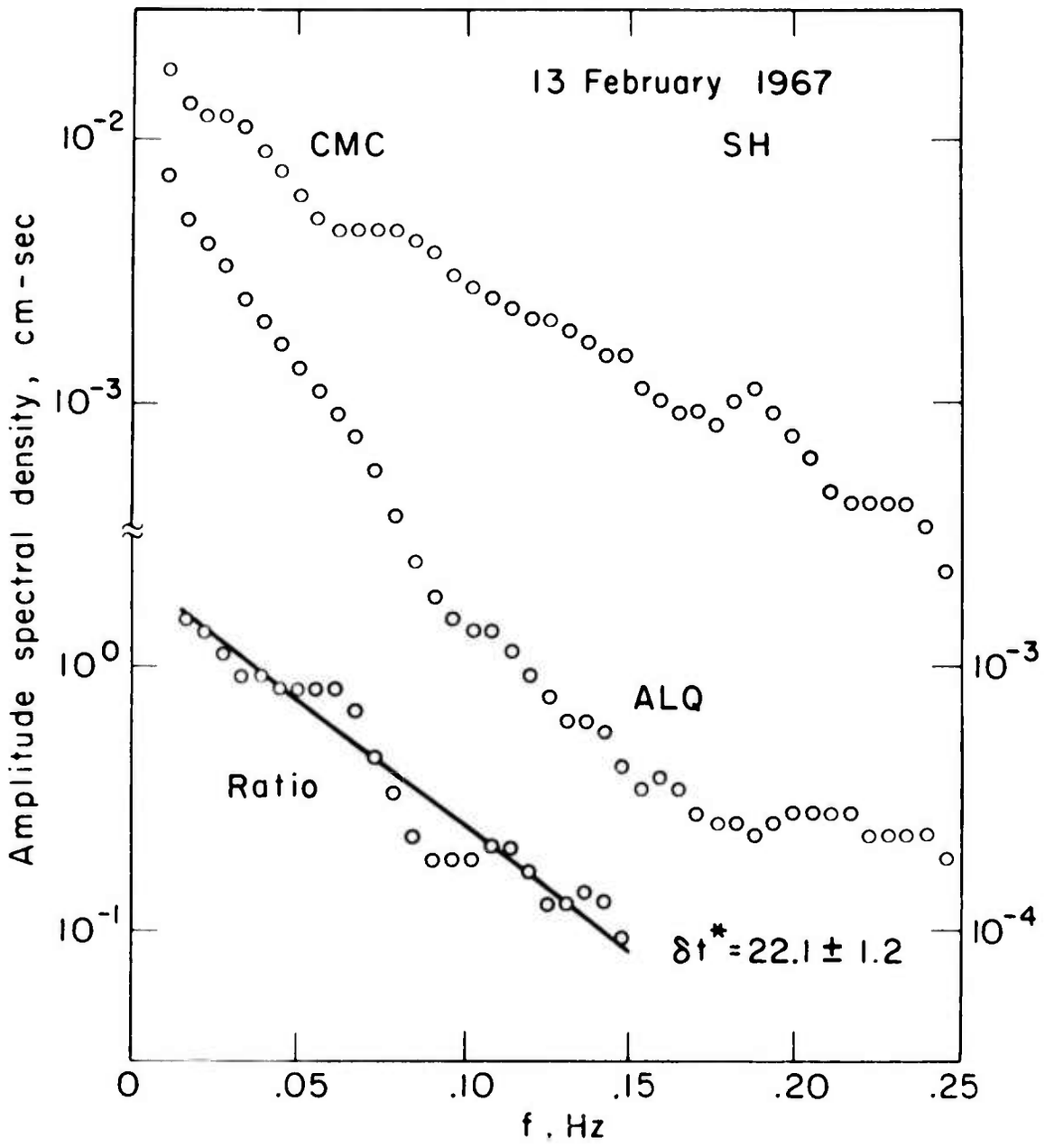
13 February 1967
CMC
SH
ALQ
Ratio
$\delta t^* = 22.1 \pm 1.2$
Amplitude spectral density, cm-sec
10^{-2}
10^{-3}
10^{0}
10^{-1}
10^{-3}
10^{-4}
0
.05
.10
.15
.20
.25
f, Hz

Figure 3

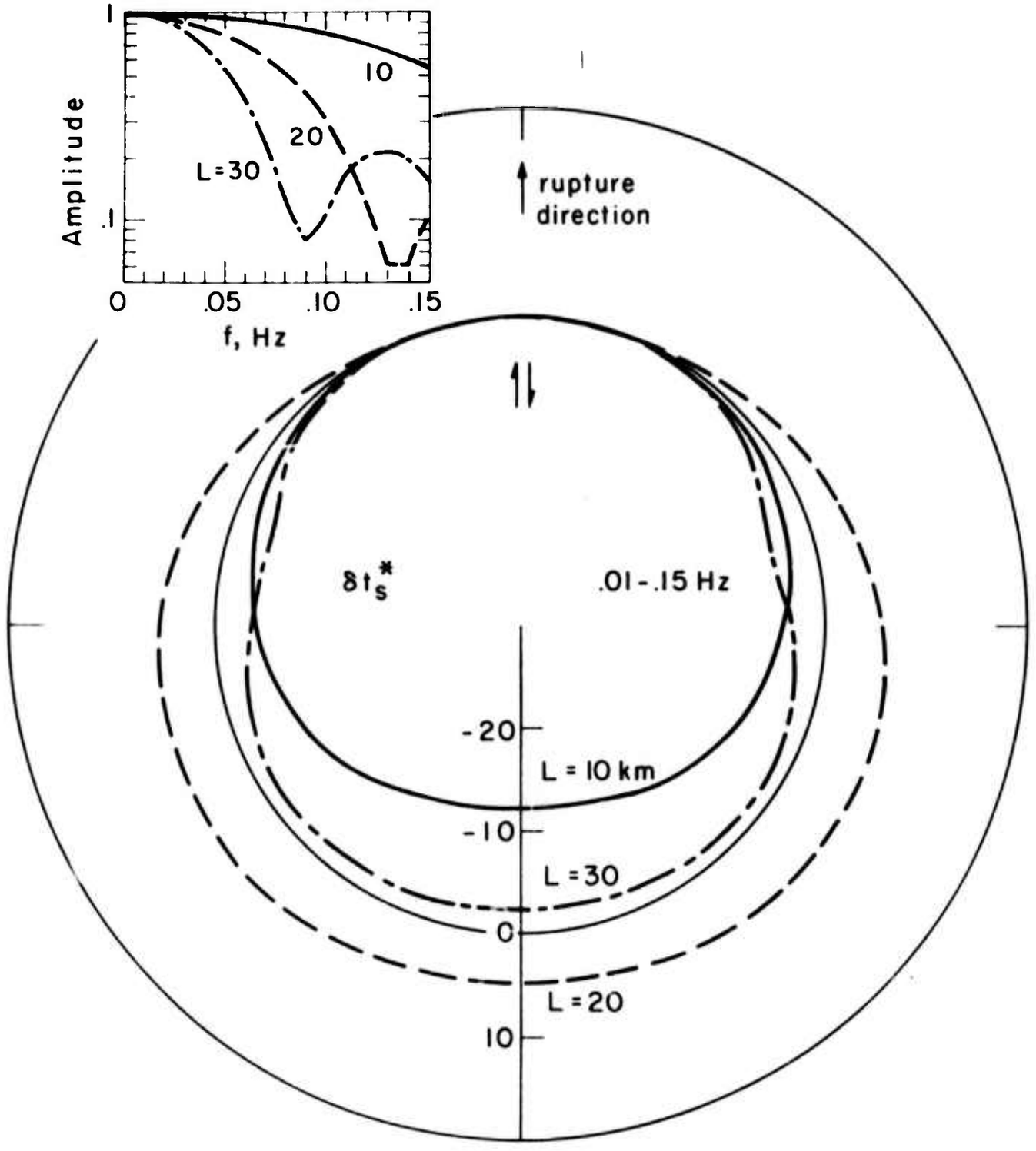
Amplitude
1
.1
0
.05
.10
.15
f, Hz
10
20
L=30
rupture
direction
δt_s^*
.01-.15 Hz
-20
L = 10 km
-10
L=30
0
L=20
10

Figure 4

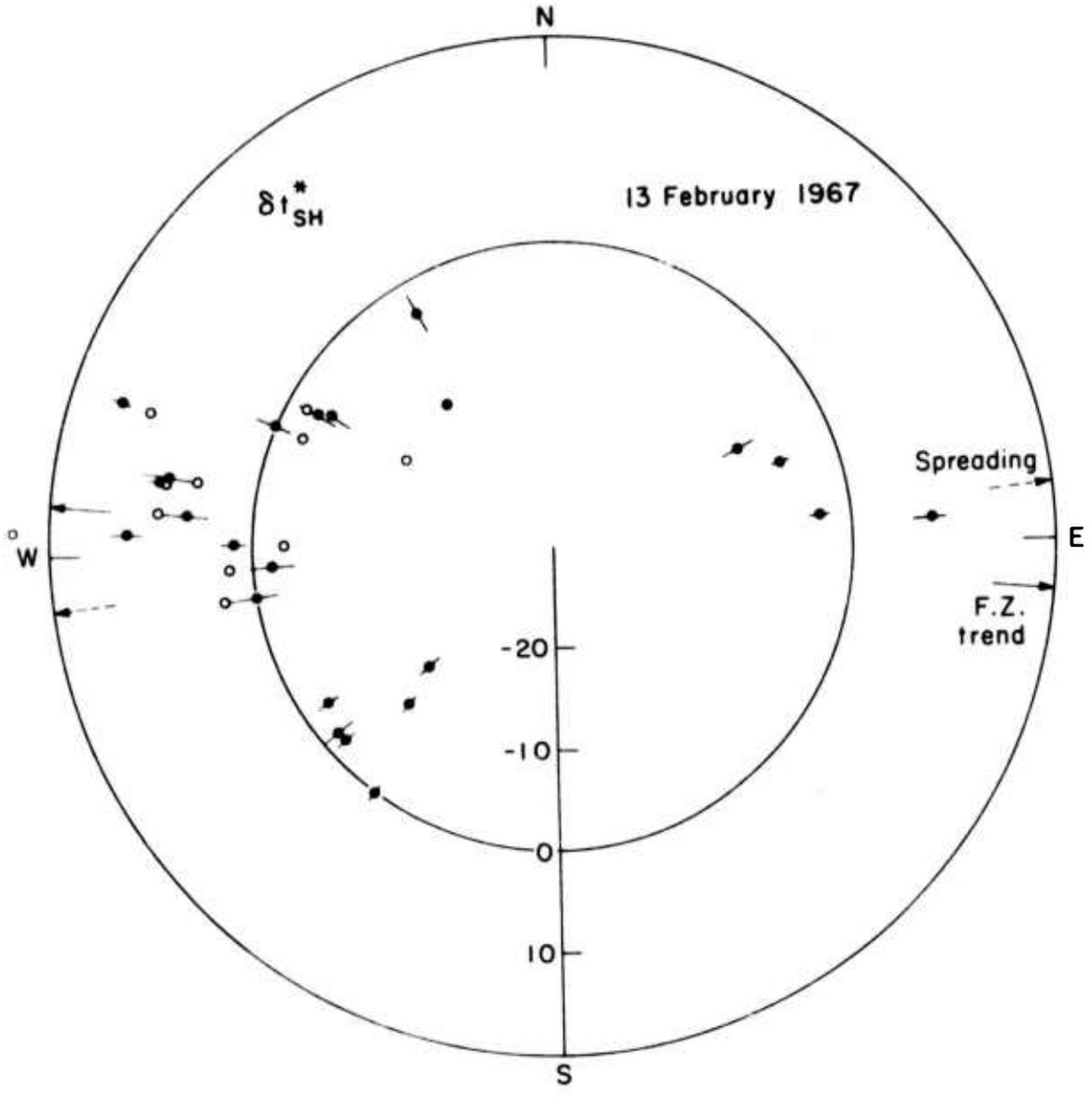

Figure 5

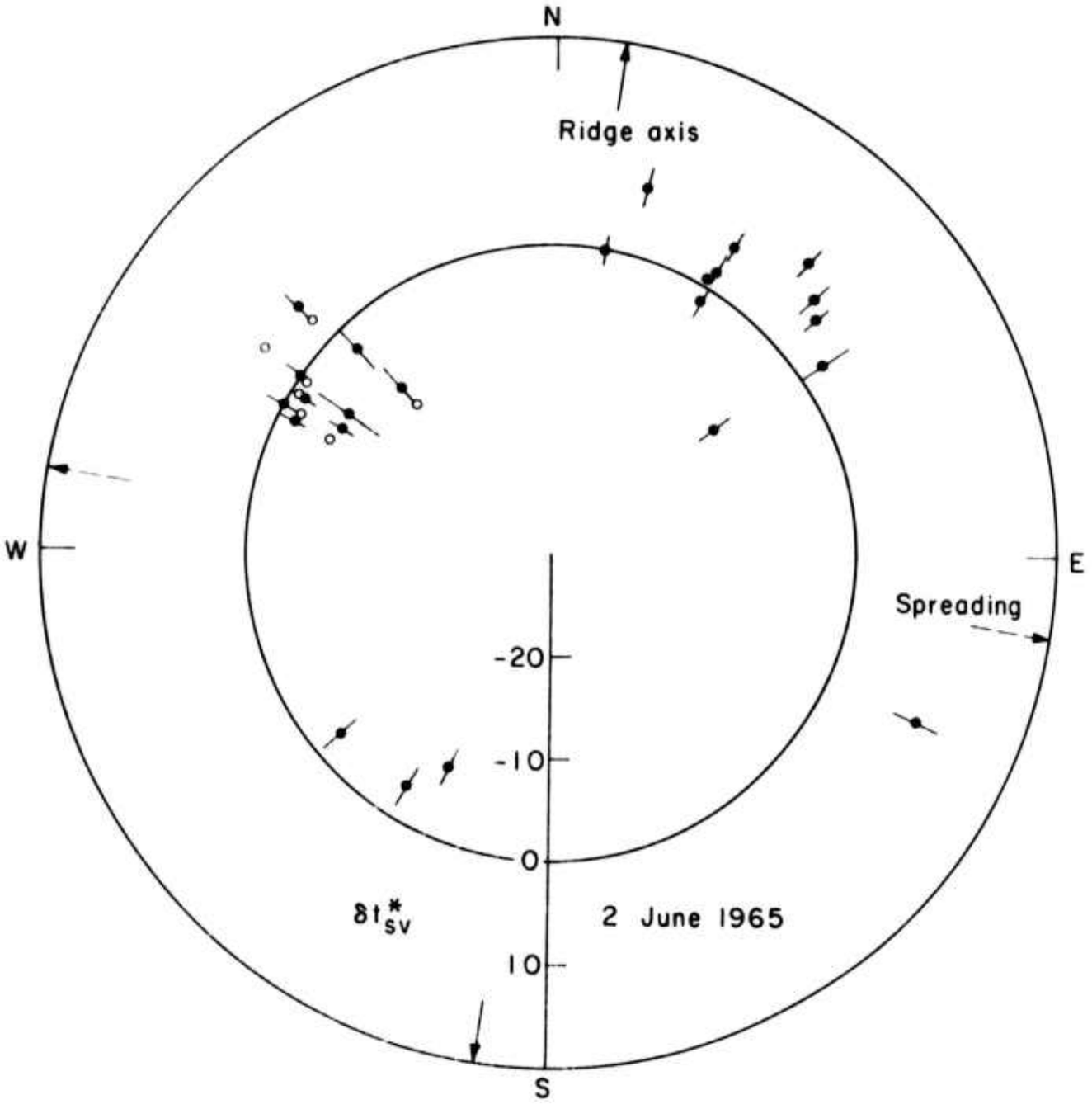

Figure 6

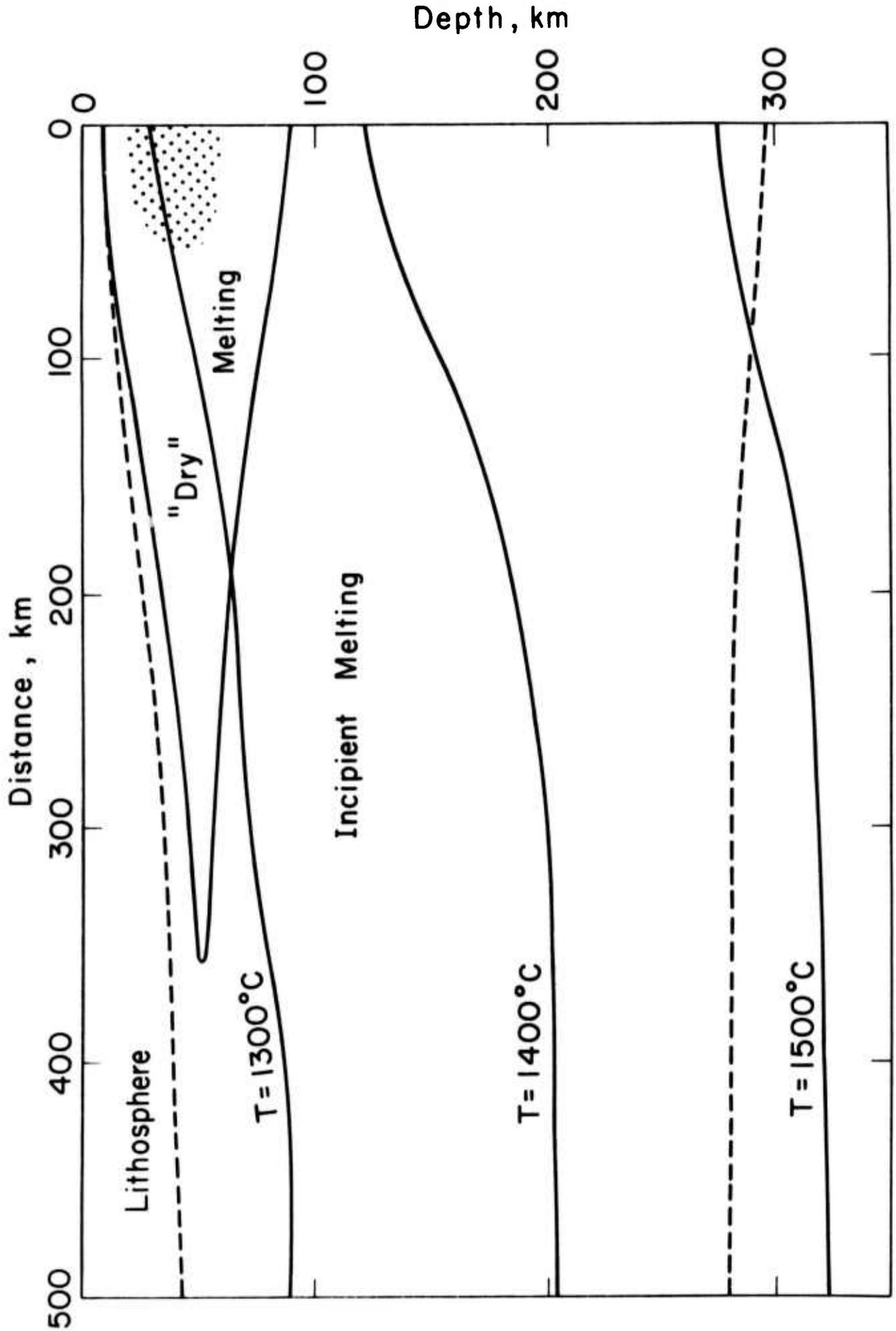
Depth, km
0
100
200
300
Distance, km
0
100
200
300
400
500
Lithosphere
"Dry"
Melting
Incipient Melting
T=1300°C
T=1400°C
T=1500°C

Figure 7

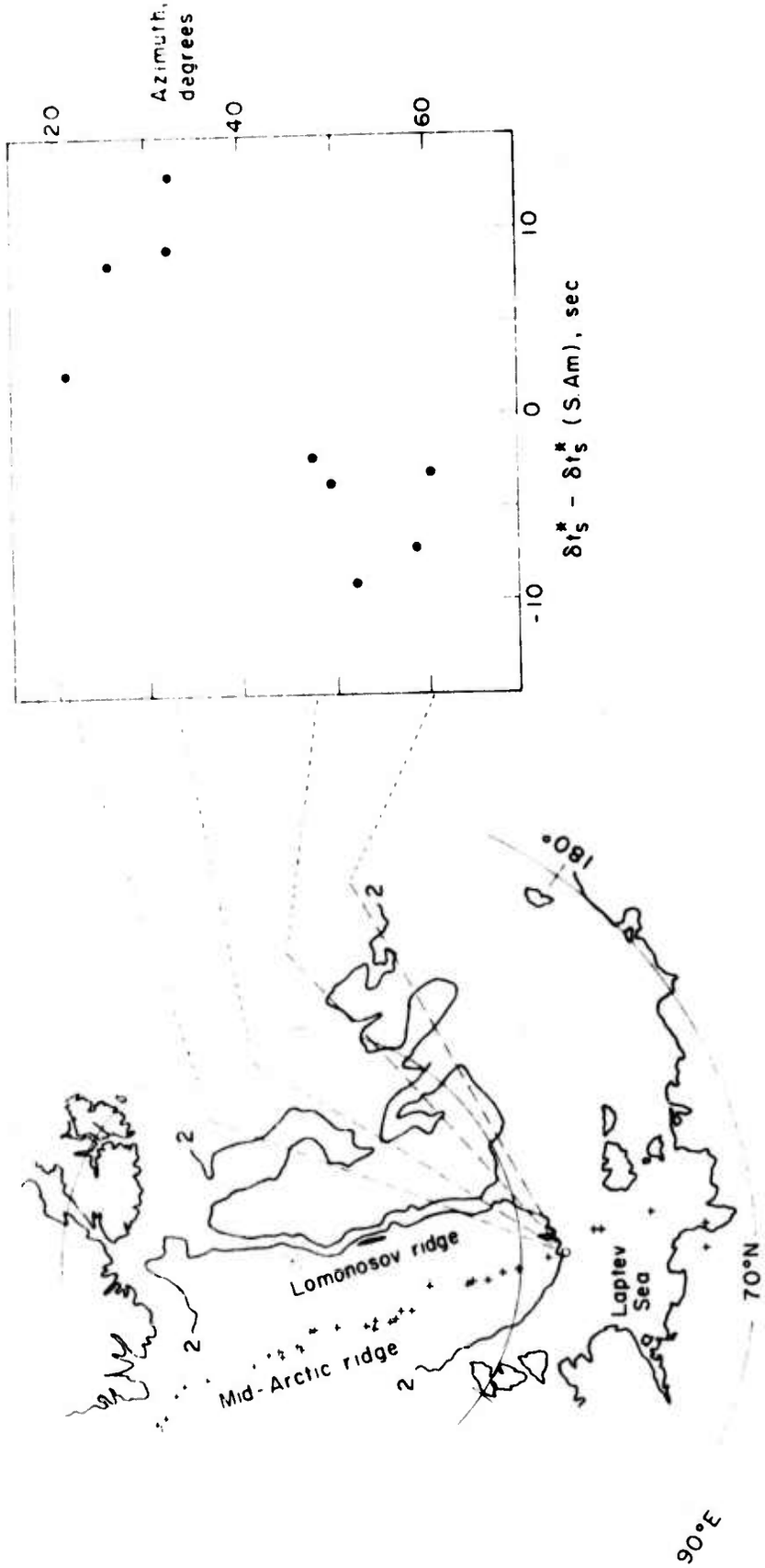
Azimuth, degrees
20
40
60
10
0
-10
$\delta t_s^* - \delta t_s^*$ (S.Am), sec
180°
90°E
70°N
Lomonosov ridge
Mid-Arctic ridge
Laptev Sea
2
2
2
2

Figure 8

3.7 Deep Structure and Geophysical Processes Beneath Island Arcs by N.H. Sleep (Abstract)

The deep structure and geophysical processes associated with island arcs were examined as a problem in heat and mass transfer. Particular attention was given to the thermal behavior of lithosphere as it descends into mantle, seismic transmission through descending slabs, the origin of the magmas which erupt on island arcs, and the cause of crustal spreading in intra-arc basins.

The factors affecting the thermal behavior of a lithosphere slab descending into the mantle are so complicated and numerous that only numerical methods can accurately account for them. A series of finite-difference calculations of the temperature field was made to test the affect of phase changes, the dip of the slab, the thermal conductivity, and the initial geotherm. Reasonable variations in those parameters and geologically permissible variations in radioactive heating and adibatic compression did not greatly affect the gross thermal structure calculated for the slab. Irregularities in slab movement on a time scale of less than 2 million years do not significantly affect the thermal field. Possible factors limiting the maximum depth of seismic zones include thermal assimilation of the slab due to latent heat from phase changes and thermal conduction, mechanical disruption of the slab, and

the lack of stress at great depths due to lower density contrast between the slab and the mantle.

Theoretical ray paths through the numerically calculated thermal models of slabs were computed. The results were in good agreement with observed travel times. First motion amplitudes of P-waves at teleseismic distances were measured from long and short period WWSSN records of intermediate focus earthquakes in the Tonga, Kermadec, and Kuril regions and of nuclear explosions and shallow earthquakes in the Aleutian region. These amplitudes were corrected for source mechanism. The Aleutian data were sufficient to show that intermediate focus earthquakes in that region occur in the colder regions of the slab. At short periods shadowing effects which could be associated with the slab were not very marked, less than a factor of 2 reduction for epicentral distances greater than 50 degrees and possibly more reduction for epicentral distances between 30 and 50 degrees. No systematic effects due to plates were found in the long period data. Some stations in the predicted shadow zone of a Tonga earthquake recorded low amplitude precursors which probably were greatly defocused waves which ran the full length of the slab. Simple diffraction is incapable of explaining the short period results.

Numerical and analytic models were constructed to examine four hypotheses for the origin of island arc volcanics: (1) melting at temperature lowered by inclusion of subducted material; (2) frictional heating related to the descent of the slab; (3) upwelling of material from the asthenosphere into the lithosphere of the island arc; (4) concentration of pre-existing melt in the asthenosphere. Presently available geochemical data are insufficient to resolve whether a significant portion of subducted material erupts on island arcs. This does not create a difficulty in evaluating the other hypotheses, as the observed eruption of temperature of island arc volcanics is similar to that of basalt. The viscosity of the melt and the geometry of the asthenosphere are not conducive to segregation of melt. At low concentrations of melt, the regions with the highest concentration of melt contribute disproportionately to the magma which segregates. About 4 kb of shear stress is needed to cause melting above the slab. Frictional heating is likely to cause the widespread high crustal temperature observed beneath island arcs. Hypothesis 3 involves no obvious thermal or mechanical difficulties although the uncertain rheological properties of the region near the base of the lithosphere preclude the computation of a realistic, detailed model. However, it is both mechanically and thermally reasonable that the slab could entrain intermediate viscosity material near the base of the lithosphere.

An influx of material from the asthenosphere to replace the entrained material could produce high crustal temperatures and provide a source region for island arc volcanics.

The hypotheses and models studied in relation to island arc volcanism are also relevant to spreading in intra-arc basins. Frictional heating above the slab is probably insufficient to cause this spreading. A numerical study was made to see if the extension could be related to viscous flow of material entrained with the slab. This calculated flow had the correct geometry to cause tension behind the island arc. Intra-arc spreading would be most likely to occur if the flow was induced in the intermediate viscosity region between the lithosphere and the asthenosphere.

3.8 Evolution of the Downgoing Lithosphere and the Mechanisms of Deep-Focus Earthquakes by M.N. Toksöz, N.H. Sleep and A.T. Smith

Summary

The thermal evolution of the lithospheric slab at subduction zones and its geophysical effects are numerically calculated. An alternating-direction, implicit, finite-difference scheme is used to compute the thermal

models taking into account all heating sources and phase boundaries. These models, with the appropriate spreading rates and dip angles, are compared with different island arc systems. Temperatures inside the slab are strongly controlled by the conductivity and by the time elapsed since the initiation of descent. The depth to which temperature anomalies persist is generally about 700 km or less.

The thermal results are used to construct the seismic velocities and ray paths, density anomalies, and the resulting stress distribution. Comparing the theoretical stress distribution and the focal mechanism studies of intermediate- and deep-focus earthquakes indicates the importance of both the mantle's rheology and the temperature-dependence of the slab's elastic properties. The intermediate and deep focus earthquakes are located along the coolest region of the slab. The theoretical results explain the source mechanisms and the orientation of principal stresses under major island arcs.

INTRODUCTION

The interest in the distribution and nature of deep-focus earthquakes has been intensive and the circum-Pacific belt has been extensively studied (Honda 1934; Wadati 1935; Gutenberg & Richter 1939, 1954; Oliver & Isacks 1967; Sykes 1966; Kondorskaya & Postolenko 1959). A renewed interest in and much better understanding of island arcs and deep seismicity have emerged in recent years with the sea-floor spreading and the global tectonic hypotheses (Isacks et al. 1971; Griggs 1972; Smith & Toksöz 1972).

In this paper we discuss the thermal regime and the stress field inside a descending lithospheric plate. First we present theoretical models of the thermal evolution of a downgoing slab. Later, we compute the resulting stress fields and compare these with the distribution and mechanisms of intermediate and deep focus earthquakes.

THERMAL EVOLUTION OF A DOWNGOING SLAB

The motion of the descending slab is a continuation of the lithospheric spreading. Once the kinematics of the motion are specified, the calculation of the temperature field becomes practical without solving the full convection problem for the earth.

Studies of the thermal regimes of downgoing slabs have been carried out by several investigators using different models and techniques. McKenzie (1969) used a two-dimensional analytic formulation which assumed the top and the bottom of the slab were isotherms. Griggs (1972) included the phase changes in a numerical solution with similar boundary conditions. Turcotte & Oxburgh (1969) obtained a solution using boundary layer theory. Minear & Toksöz (1970a,b), Hasebe et al. (1970), and Toksöz et al. (1971), used two-dimensional numerical models in which the mantle surrounding the slab was explicitly included so energy was conserved.

In this section we briefly review the numerical calculations following Toksöz et al. (1971). We especially focus our attention to effects of various physical properties and to the questions related to geometry and the rate of descent.

Computation of Temperature Field

The computational scheme used in this study is similar to the method described in detail in an earlier paper (Minear & Toksöz 1970a). The basic model consists of a slab of material moving downward into the mantle at a specified angle. The surrounding mantle material is assumed to be fixed (Fig. 1). The computational scheme consists of translating temperatures downward in the slab and then allowing the slab to warm up over the time interval Δt, which corresponds to the vertical movement d. In essence we assume the dynamics and compute the temperature field given this motion field.

Temperatures are computed from the conservation of energy equation

$$C_p \rho \frac{\partial T}{\partial t} = \nabla \cdot (K \nabla T) + H \qquad (1)$$

where

C_p = specific heat at constant pressure, ρ = density, T = temperature, K = conductivity, and H = heat generation rate per unit volume.

The alternating-direction, implicit, finite-difference scheme (Peaceman & Rachford 1955) is used to solve (1) numerically. The method was described earlier by Minear & Toksöz (1970a).

Physical Parameters and Energy Sources

Certain physical parameters (conductivity, specific heat, density, mantle geotherm) and the energy sources that are incorporated in H (radioactivity, adiabatic compression, phase changes and shear-strain heating) must be specified for solving (1). Some parameters can be specified and remain nearly constant as a function of position. Others strongly depend on temperature and need to be updated at each step and every grid point.

Physical Parameters

In these calculations we used the average density profile of the oceanic model (Press 1970) and a constant specific heat of $C_p = 1.3 \times 10^7$ erg/g °C.

In the thermal conductivity the contributions of both the lattice conduction and radiative heat transfer were taken into account. One set of models was based on the formulation of MacDonald (1959).

$$k = k_1 + (16n^3 sT^3)/(n\varepsilon_0 + 120\pi\sigma_0 \exp(-E/KT)) \qquad (2)$$

where

k_1 = lattice conductivity, 0.25×10^6 erg/cm-sec-°C,

T = absolute temperature, K = Boltzmann's constant,

E = width of energy gap for electronic conduction, 3 e.v., s = Stefan-Boltzmann constant, n = index of refraction (n = 1.7), ε_0 = low temperature opacity (ε_0 = 10 cm^{-1}), and σ_0 = electrical conductivity (σ_0 = 10 $ohm^{-1}cm^{-1}$).

The other set of models used the experimental results of Schatz & Simmons (1972) on olivine. In this case the lattice conductivity is the larger of

$$k_l = (30.6 + 0.21T)^{-1}$$
$$k_l = 0.003 + (3 \times 10^{-6})z \qquad (3)$$

where z is in kilometers, T in °K and the unit of conductivity is cal/cm-sec-°C. The radiative conductivity is given by

$$k_r = 0 \qquad T \leq 500°K$$
$$k_r = 5.5 \times 10^{-6}(T - 500) \qquad T > 500°K \qquad (4)$$

The conductivity change associated with the phase change at 400 km is probably not very large since ferrous iron, which increases opacity and reduces radiative conductivity, enters the common phases on both sides of the transition zone (Ringwood 1970). If iron-free oxides such as MgO, Al_2O_3 or SiO_2 exist as minerals below the 600 km discontinuity, the radiative conductivity would be extremely high.

In earlier studies the unperturbed geotherm of the mantle was either assumed to be adiabatic (McKenzie 1969), the

conductivity geotherm (Minear & Toksöz 1970a,b; Toksöz et al. 1971) or to be controlled by the solidus temperature of peridotite (Griggs 1972). In this paper an approximation to the average geotherm in a convecting earth was also used. The unperturbed geotherm is indicated in each temperature figure in the following section.

Heat Sources

In addition to conduction of heat from the surrounding mantle, the slab is heated by internal heat sources. These consist of radioactivity, adiabatic compression, phase changes, and the shear strain heating along the slab-mantle boundaries.

Radioactive heating. The average radioactivity of the oceanic lithosphere is probably about equal to the radioactivity of the upper mantle, because differentiation at mid-oceanic ridges occurs mainly above 30 km depth (Kay et al. 1970).

Radioactive heating in the upper mantle of the earth is too low to seriously affect the evolution of the slab. A more important effect of radioactive heating is on the unperturbed geotherm of the upper mantle. The estimates of heat generation due to radioactivity cover a wide range: 2.3×10^{-7} erg/gm sec (MacDonald 1959, 1963), 5.4×10^{-8} erg/gm sec (Armstrong 1968), and 1.5×10^{-8} erg/gm sec (Hurley 1968a,b). The larger radioactivity of MacDonald would

increase the temperature only 6°C in the 10 m.y. descent of the slab. In these calculations we have used heat production values of 2.29×10^{-7} ergs/g sec for the upper mantle and 1.67×10^{-8} ergs/g sec for the mantle below 465 km.

Adiabatic heating. As the lithosphere descends into the mantle, it is compressed and heated. The adiabatic temperature gradient is given by

$$\partial T/\partial z = g\alpha T/C_p \tag{5}$$

where g is the gravitational acceleration and α is the volume coefficient of thermal expansion. The rate of thermal energy release at depth h due to adiabatic compression is

$$\left.\frac{dQ}{dt}\right|_h = C_p \rho (\partial T/\partial t)$$

$$= C_p \rho (\partial T/\partial z) V_z = \rho g \alpha T V_z \tag{6}$$

where V_z is the vertical component of the velocity of the downgoing slab. The value dQ/dt can be evaluated at each point by using appropriate values for ρ, g, α, and T (Hanks & Whitcomb 1971). ρ and g are known and T is computed from the previous time step. Laboratory measurements of α tabulated by Skinner (1966) indicated a slight increase in α with increasing temperature and a decrease in α with increasing pressure. For these calculations we expressed the depth

dependence of α by

$$\alpha = \exp(3.58 - 0.0072z) \qquad (7)$$

where z is depth in km and α is measured in 10^{-6} °C^{-1}. Near the surface (z = 0) the value of $\alpha = 36 \times 10^{-6}$ °C^{-1} corresponds to that of olivine at about T = 500°C (Skinner 1966). The exponential coefficient 0.0072, for depth dependence, is somewhat lower than estimates of Birch (1968) and slightly higher than those of Verhoogen (1951). The above expression gives a value of $\alpha = 18 \times 10^{-6}$ °C^{-1} at z = 1000 km, in agreement with the value used by Griggs (1972).

Since α decreases with depth while the temperature is increasing inside the slab, the adiabatic heat generation (dQ/dt) varies slowly, increasing slightly with depth.

Phase changes. Several phase changes may occur in the upper mantle. Seismic velocity profiles indicate the presence of second-order discontinuities at depths of about 350 and 650 km (Toksöz et al. 1967; Johnson 1967; Julian & Anderson 1968; Archambeau et al. 1969) that are most likely caused by olivine to spinel and spinel to post-spinel changes (Anderson 1967). In addition to these, a phase change corresponding to a basalt-eclogite or a plagioclase peridotite-garnet peridotite reaction is considered at shallower depth.

If the vertical velocity through a phase change is fast

enough to disturb the isotherms, the phase boundary will be moved from its normal position (Schubert & Turcotte 1971). To calculate the effects of phase changes, all points in the model were examined at the end of each translation step and the change in the amount of each phase from the previous step recorded. Latent heat was calculated from this change and included as a heat source in the model. The routine for translating temperature was also used to determine the amount of each phase with the slab. This calculation scheme was used for phase changes going both ways whether or not the slab is assumed to move.

Three phase changes were considered in the models. Phase change energies were computed from entropy (S) and volume (V) changes. Because the temperatures vary inside the slab, the phase boundaries were determined from the dP/dT slopes for each phase change, starting from the shallowest. The ΔS values for the three phase changes are taken as -11.7×10^5, -7.13×10^5, and -5.94×10^5 ergs/g°C. Corresponding ΔV values are -6.5×10^{-2}, -2.65×10^{-2}, and -2.62×10^{-2} cm^3/g. These values are averages of those given by Verhoogen (1965), Akimoto & Fujisawa (1968), Ringwood (1970, 1972), Sclar et al. (1964). The parameters for the spinel-post-spinel phase changes are the least reliable. These

reactions were studied indirectly with chemical analogs (Akimoto 1970; Ringwood & Major 1970). Ringwood (1972) takes this reaction to be exothermic (and $dP/dT > 0$) while others (D.L. Anderson 1972, personal communication) suggest that it may be endothermic. Because of these uncertainties, we constrained the phase boundary to remain at 650 km depth, but adopted a positive heat contribution. We also calculated some models without any heat contribution from this phase boundary. No allowance was made for any changes in heat balance due to possible melting of the material.

Shear-strain heating. An accurate estimate of the shear-strain heating is extremely difficult, because we know neither the mechanisms involved in the descent of the slab nor the parameters, such as the thickness of the shear zone and its viscosity. The complexity of the problem even for an idealized fluid model has been illustrated by Turcotte & Oxburgh (1969b).

In the calculations we used several values for shear-strain heating. In all cases viscous heat generation was confined to 14 km thick layers along the top and bottom of the slab. At the top edge, the maximum shear-strain heat generation rates are 1.6×10^{-4} ergs/cm^3 sec, unless specified otherwise. At the lower boundary, the shear-strain heating is 1.6×10^{-5} ergs/cm^3 sec (a factor of ten less than the top)

and it has a negligible effect on the thermal regime.

At the 8 cm/yr subduction rate, the frictional heating used at the top of the slab is equivalent to a stress of a few kilobars (in an extreme case it could be as high as 4 kb). Although this is high compared to apparent stress drop associated with earthquakes, there is evidence that high stresses prevail in the lithosphere at the convergence zones. For example, to produce the observed uplift at the outer rise of the Japan trench, stresses of a few kilobars are needed (Hanks 1971).

Temperature Models

A series of temperature models were computed to demonstrate the evolution of the thermal regime. Only a few models will be shown in this paper in addition to those in the previous papers to demonstrate the effects of important parameters and varying geometry (Minear & Toksöz 1970a,b; Toksöz et al. 1971).

The development of the thermal regime in a downgoing slab is shown in Figs. 2 and 3 as a function of time. Temperature fields shown after 3.6 and 7.1 m.y. (Fig. 2) and 10.7 m.y. (Fig. 3) from the start of downward motion demonstrate the relative effects of time and crossing of phase boundaries. The phase boundaries are elevated by as much as 150 km as a result of the lower temperatures. At the rate of 8 cm/yr, the

interior of the slab remains cooler relative to the surroundings to a depth of at least 600 km. In the coolest zone, the temperature difference is more than 500°C.

The rapid heating of the slab interior below 600 km is primarily due to the higher thermal conductivity (because of increased contribution of radiative heat transfer at higher temperatures) and to the contribution of spinel-post-spinel phase transformation. The thermodynamic parameters of this transformation are not well known and that is why we constrained the phase boundary to a constant depth. However, if the reaction is exothermic, the heat generated tends to raise the temperature to the ambient. When the internal slab temperature approaches the mantle temperature, the heat generated internally cannot be transferred to cooler portions and the source region temperature increases rapidly. As a result the slab loses its integrity and is assimilated into the mantle. Even without any heating from the lower phase boundary, the slab reaches thermal equilibrium at about 750-800 km depth (Toksöz et al. 1971).

Parameters that strongly influence the temperatures inside and around the downgoing lithosphere include the conductivity, and the descent rate. The effect of using the Schatz & Simmons (1972) conductivity is shown in Fig. 4. Comparing this with Fig. 3 [based on conductivity given by

(2)] illustrates that in the case of lower effective conductivity (Fig. 4) temperatures are lower inside the slab.

The temperatures inside the slab are strongly controlled by the time elapsed after the initiation of the descent. A slower moving slab will tend to heat up more because of the increased conduction of heat from the surrounding mantle. For a descent velocity corresponding to 1 cm/yr spreading rate and a total time of 100 m.y., Toksöz et al. (1971) showed that with parameters similar to those of Fig. 3 the slab reaches thermal equilibrium at a depth of about 400 km. Here we expanded these calculations to include stop-and-start type slab motions and differing angles at which the slab penetrates into the mantle.

The temperature field of a slab dipping 29 degrees was computed using the physical parameters of the base model (i.e., Fig. 3) and the results are shown in Fig. 5. Although 16 m.y., as opposed to 11 m.y. for the base model, was required for this slab to penetrate to 650 km, the maximum depth of penetration of both slabs is controlled by the lower phase change. The maximum penetration of mantle isotherms into the slab is about 30 to 100 km less in the shallower dipping model.

It is conceivable that for a period of time a slab may become hung up at a trench such that no subduction occurs. Once subduction ceases it is likely that the slab will detach and sink as it may have done in the New Hebrides. Detachment could also occur if new material were being subducted more slowly than the separation rate. The thermal effects of stopping the motion after the slab penetrated to 650 km are shown in Fig. 6. In these calculations the same slab shown in Fig. 5 was allowed to remain stationary. After 16 m.y. (total age 32 m.y.) the slab was still evident but the temperature anomaly was spread over a larger region. After 48 m.y. only a very broad temperature anomaly remained. It is not likely that a seismic zone could remain active for a long time after subduction ceases. The most likely event is that, once the slab is partially heated, detachment would occur and the cooler slab would sink.

The use of a cooler ("convective") geotherm and the effect of the 600 km phase boundary is shown in Fig. 7. The use of the "convective" geotherm does not greatly alter the temperature field (Fig. 7). The lower phase change was not included in constructing the geotherm of the model. Unlike the models using the strongly superadiabatic MacDonald (1959) geotherm, the temperature field is not greatly influenced by the kinematics assumed for the slab, since motions in the

nearly adiabatic regions of the mantle effect temperatures only slightly. It should also be noted that the effect of a 400 km phase change is evident, although this reaction was explicitly included when constructing the geotherm. The 600 km phase change was not included in these calculations.

The omission of the phase change at 600 km depth increases the depth at which the slab reaches thermal equilibrium. Even in this case, however, the equilibration occurs at about 800 km depth (Toksöz et al. 1971). At these great depths, the contribution of radiative heat transfer becomes substantial and the slab interior warms up rapidly. Continuing the calculations to greater depths results in temperatures inside or around the slab higher than the ambient mantle temperatures. It is reasonable to assume that the slab assimilates into the mantle and becomes part of the general mantle convection pattern after it reaches thermal equilibrium. As long as the subduction continues at some uniform rate, the temperatures inside the slab above the depth at which the slab's interior reaches equilibrium change very little with time. For an 8 cm/yr subduction rate for example, the thermal regime reaches a nearly stable state after about 10 or 12 million years above a depth of 700 km.

Convergence of continental lithospheres. In a separate yet related area to the subduction of the oceanic lithosphere, we

investigated the thermal regime for the convergence of two continental lithospheres. Because of the generally shallower angle of penetration [for example, the dip of the thrust belt is between 10 and 20° for the Zagros convergence zone in Southern Iran (Nowroozi 1972)], slower rate of subduction, continental geotherm, and higher radioactivity in the continental crust, the thermal evolution is expected to be different from that in the oceanic case.

The large scale structure in the region of a continent-continent collision may be in part inherited from the pre-existing active continental margin and in part due to the subducted continental crust. For continental crust to have much effect on temperature during its subduction, either the shear strain heating would have to be high or the subduction rate would have to be low for prolonged radioactive heating. The average radioactive heat production of continental crust is about 4.1×10^{-6} erg/gm-sec (Hurley 1968a,b; Armstrong 1968) and this can cause a maximum temperature increase of 10°C/m.y.

A numerical model of continental convergence is shown in Fig. 8. The subduction rate is 1 cm/yr. A high value of frictional heating (1.6×10^{-4} ergs/cm^3 sec) is used along the upper edge. Radioactive heat generation is 4.1×10^{-6} erg/gm-sec in the crust (hatched region) and 1.5×10^{-8} erg/gm-sec in the mantle. Although this model

shows high geothermal gradients above a subducted continent; this does not seem to be sufficient to cause extensive melting or magmatization associated with orogenies.

Another continental convergence model with lower frictional heatings (1×10^{-5} ergs/cm^3 sec above 35 km depth) is shown in Fig. 9 for two time intervals. Other parameters are the same as those of Fig. 8. After 7.7 m.y. the temperatures are slightly lower inside the slab, except at the boundary below 100 km depth. After about 50 m.y. (lower figure) the temperature returns to steady state. We may conclude that orogeny is most likely to occur during the collision or after about 50 m.y. when the subducted continental material has become heated. In the former case the heat of the orogeny would be related to volcanic activity along the active margin prior to the collision. In the latter it would be radioactive decay in the subducted material.

Geophysical Effects

The strongly varying temperature field of the upper mantle inside and in the vicinity of the slab affects the surface heat flux, volcanism, density, seismic wave velocity and attenuation, as well as the stress field and the occurrence and mechanisms of earthquakes. Most of these effects have been discussed in previous papers (Toksöz et al. 1971; Sleep

1973). Not all surface data are equally revealing about the properties of the deep lithosphere. For example, heat flow is primarily controlled by the temperature field at relatively shallow depth and by convective heat transfer underneath and behind island arcs (Hasebe et al. 1970).

The gravity anomalies associated with downgoing slabs are broad regional anomalies (Minear & Toksöz 1970a,b; Griggs 1972). These are generally obscured by the much sharper anomalies over trenches and island arcs that result from topography and crustal structure. Observed gravity anomalies have been fitted with a model including a slab in the Aleutians (Grow 1972).

The most pronounced effects of the temperature fields of descending slabs are on seismic velocities, Q structure and intermediate and deep focus earthquakes. Velocity and amplitude anomalies of seismic waves have been used to demonstrate the existence of the slab (Davies & McKenzie 1969; Sorrells et al. 1971; Mitronovas & Isacks 1971; Toksöz et al. 1971; Jacob 1970, 1972; Abe 1972a,b; Davies & Julian 1972). The observed travel time anomalies are in close agreement with the theoretical models based on the calculated temperature profiles (Sleep 1973).

The distribution and stress fields associated with these deep focus earthquakes will be discussed in detail in the next section.

DISTRIBUTION AND MECHANISMS OF DEEP FOCUS EARTHQUAKES

Since their discovery the origin and mechanisms of intermediate and deep focus earthquakes have been of great interest. The sea-floor spreading and global tectonic hypothesis with descending slabs has provided an explanation for these deep earthquakes. It is generally accepted that the slab behaves like a stress guide. However, the mechanisms of the intermediate and deep earthquakes show remarkable differences between regions not explained by any simplified hypothesis (Isacks & Molnar 1971). In this section we treat this problem in two steps. First we determine the hypocenters relative to the slab boundaries. Then, computing the stresses arising from subduction, we investigate the mechanisms of these earthquakes.

Distribution of Deep Focus Earthquakes

The shallow earthquakes near island arcs are concentrated in the convergence zones between plates, mostly along the upper boundary of the underthrusting plane of the oceanic lithosphere. For the Aleutians and Japan both the distribution of hypocenters and the source mechanisms of earthquakes support this conclusion (Barrazangi & Dorman 1969; Stauder 1968; Utsu 1971; Isacks & Molnar 1971; Plafker 1972; Engdahl 1972). For intermediate and deep focus earthquakes the

precise location of hypocenters becomes more difficult because of the effect of velocity anomalies within the slab on the seismic ray paths.

In order to further constrain the locations of intermediate earthquakes with respect to the slab, we investigated the central Aleutians. Nuclear explosions LONGSHOT, MILROW and CANNIKIN provided sources of precise location and time for calibrating the velocity models and slab location relative to the trench. Furthermore the network of seismic staticns in the area provided very good locations of the earthquakes. The theoretical ray paths from surface focus events were calculated using seismic velocities deduced from a temperature model of the Aleutian slab. A most likely location of LONGSHOT relative to the slab was determined by comparing the computed travel time delays (Fig. 10) and shadow zone with the observations (Abe 1972a; Jacob 1972; Sleep 1973). The preferred slab location based on the above data is then compared with the hypocenters of earthquakes (Engdahl 1971) in Fig. 11. It is very clear that the intermediate focus earthquakes are located along the coolest region of the slab. Similar distributions are implied for the earthquakes under Japan (Katsumata 1967; Utsu 1971) and the Tonga Kermadec region from travel times and attenuation characteristics of P and S waves (Sykes et al. 1969; Mitronovas et al. 1969; Toksöz et al. 1971; Sleep 1973).

Mechanisms of Deep Focus Earthquakes

Observational data on source mechanisms of intermediate and deep focus earthquakes have accumulated in recent years from fault-plane studies. A comprehensive summary is given by Isacks & Molnar (1971). In this section we describe the calculation of stress field in a downgoing slab and compare this with the earthquake distribution and mechanisms.

Computation of stress fields. The theoretical studies of stress regime (McKenzie 1969; Griggs 1972; Smith & Toksöz 1972) are hampered by both the computational difficulties and the limited knowledge of mantle rheology. Here, following Smith & Toksöz (1972) we utilized a kinematic approach for computing stresses in a subducting slab. We included the direct effects of subduction (i.e., body forces due to density anomalies resulting from cooler temperatures) in the calculations.

In our calculations a slice of mantle, which includes the slab, was modelled as a heterogeneous, temperature-dependent, viscoelastic medium. Using the correspondence principle for viscoelasticity (Christensen 1971), the operators of the viscoelastic problem are replaced by an equivalent elastic modulus which incorporates the temperature and stress dependence for that increment in time. The much simpler elastic problem was

then solved numerically for the stresses (Zienkiewicz 1971). For sufficiently small time increments, this also applies to a nonlinear problem. The model for the slab assumed quasi-static behavior after application of the loads. The time since loading was taken as approximately 100 years; this approximates the frequency of transient phenomena (i.e., deep earthquakes) within the slab. Thus the problem assumes a certain temperature dependent rheology and application time for the loads; the resulting operator E, an effective Young's modulus, is solved as an elastostatic problem for the strains resulting from creep since application of the load.

Using the thermal models in the preceding section and the thermal expansion coefficient (7), the density anomalies were computed relative to the mantle isotherm at each depth. These specify the vertical body forces ($F = g\rho\alpha\Delta T$) at all points inside the slab. For a temperature model similar to Fig. 4, the corresponding body forces are shown in Fig. 12. The density changes and the resulting forces due to phase changes were separately taken into account.

A finite difference scheme incorporating the body forces was then used to compute the stresses for the elastostatic analogy. The scheme uses an integral formulation of the equations together with over-relaxation to obtain a solution (Tillman 1971; Smith & Toksöz 1972); thus, it is essentially a finite-element computation. A 20 km grid spacing was used

to solve the problem for an 840 by 680 km region enclosing the slab and the adjacent mantle. The imposed boundary conditions were that the top face (the earth surface) was free, the vertical boundaries at the sides of the region and the bottom boundary were specified to be rigid. Other boundary conditions were also used for the side boundaries, but the effects were found to be insignificant for the calculated stresses inside the slab.

The rheology of the slab and the surrounding mantle were specified in terms of temperature and pressure dependent constants. For the mantle, the operator E was obtained using effective mantle viscosities (McConnell 1968; Cathles 1971) and the elastic-viscoelastic analogy (Christensen 1971). The slab rheology was assumed to be temperature dependent. For long-term stresses, the temperature dependence of the slab properties are most likely determined by creep processes (Weertman 1970). Two separate relationships were used to express the variation in the effective Young's modulus inside the slab:

$$E_{slab} = E_{mantle} + 5.0 \times 10^{10} \exp(-0.35 \times 10^{-2} \Delta T) \quad (8)$$

and

$$E_{slab} = E_{mantle} \exp[-(1.2 \times 10^{-2} + 5.5 \times 10^{-5} p) \Delta T] \quad (9)$$

where ΔT is the lateral temperature difference between the

mantle and slab, and p is the pressure in kilobars. The latter represents a much stronger temperature dependence. Numerical models calculated with both of these relationships did not alter the stresses significantly (Smith & Toksöz 1972).

The marked effect that the mantle's support has upon the stress distribution inside the slab is illustrated in Fig. 13. Both slab models are identical and include only the body forces due to density anomalies resulting from the thermal contraction. The stress regimes are quite different. With little support or resistance to the descending lithosphere, the tension axis follows the trend of the slab along its full length. On the other hand, when the mantle's support increases with depth (top diagram, Fig. 13), the maximum principle stress becomes compressional along the full length of the slab.

As these two contrasting models indicate, the mantle support and viscosity variation with depth significantly affect the direction of stresses and the focal mechanisms of earthquakes. For short slabs where deepest penetration does not extend below low-velocity or the low viscosity zone, the direction of least compression (i.e., "tension") axis should parallel the slab's axis. For long slabs where penetration to more resistant mantle takes place, the stresses become compressive.

The density anomalies due to phase changes introduce additional stresses in the region of the transformation. Above the phase change, the stress is down-dip tension, and below, it is down-dip compression. For the olivine-spinel phase change, this can add about 200 bars of shear stress (Smith & Toksöz 1972). The effect of these phase changes may be important for variations in deep seismicity. If the post-spinel phase change at 600 km rises within the slab, additional stress would occur below the transformation and help account for the sudden rise in seismicity at about 600 km observed in the Tonga-Kermadec region.

The stresses from convection on the slab in the mantle can be incorporated as surface traction without including body forces. These are then superimposed on the previous solutions. A uniform 50 bar resistance along the upper face of the slab introduces primarily compressive stresses parallel to the axis of the slab. The resulting shear stress does not exceed 100 bars throughout the length of the slab (Smith & Toksöz 1972). These models, however, do not properly simulate the shallow stresses at the island arcs, and that was not their intent. For shallow stresses the boundary conditions at the sides of the region and the fault zone between the two lithospheric plates are important and require further refinements. Yet as formulated they are adequate for the problem at hand: the intermediate and deep stresses

within the slab. Thus there is no inconsistency between the relatively high stresses (1 kb or more) used for shear heating calculations and the models of the stress distribution within the slab's interior. To resolve those problems associated with the bending and thrusting of the descending lithosphere, additional models are necessary.

Comparison with earthquake mechanisms. The comparison of the calculated stress fields with the distribution and mechanisms of intermediate and deep focus earthquakes can now be made in regions where the seismicity is best understood. For this we chose Japan (Honshu) and the Kermadec region.

In Fig. 14 the theoretical stresses and the earthquake hypocenters given by Utsu (1971) for the Japanese island arc are compared. The shallow earthquakes are concentrated primarily along the shear zone between the underthrusting oceanic lithosphere and the continental lithosphere. As far as it can be determined from travel times and attenuation characteristics, intermediate and deep earthquakes are located in the interior of the slab along a band corresponding to the maximum shear stresses.

The correspondence between the theoretical and observed directions of maximum stresses is shown in Fig. 15. In the Honshu case the model dips 30° and has mantle properties as shown in Fig. 13a. The rheology of the slab is defined by

equation (9). On the right the directions of maximum principal stress determined by the earthquake focal mechanisms (Isacks & Molnar 1971) are shown. Both the observed and the theoretical maximum stresses are down-dip compression, which are in good agreement with each other. In the case of Kermadec, where the slab has a higher dip and rheology specified by equation (8), the observed principal stresses are down-dip compression for deep earthquakes and "tension" for intermediate earthquakes. Again, the observations are in good agreement with the theoretical model.

The calculated maximum shear stresses inside the descending slab are approximately 500 bars. Estimates of stress drop are available for a limited number of deep focus earthquakes and are near 100 bars (Wyss & Molnar 1972). This figure is reasonable for an initial (in situ) stress of about 500 bars assuming that a relationship similar to those of shallow earthquakes exists between the initial stress and stress drop.

"Faulting" mechanisms of deep earthquakes. The fault plane solutions obtained for deep focus earthquakes indicate that double-couple type source functions fit the observed radiation pattern (Isacks & Molnar 1971; Stauder 1968). The 650 km deep Colombian earthquake studied in detail by Mendiguren (1972; epicenter 1.5°S, 72.6°W, origin time July 31, 1970,

17h 08m 05.4s, magnitude 7.1) using both first motion polarities and free oscillations verifies a double-couple source. Any volumetric component of this earthquake source contributes no more than 10 percent to the radiated seismic energy.

With the descent of the isotherms inside the slab, could the material fail in a mode seismically equivalent to brittle fracture at a depth of 600 km or more? In the absence of direct laboratory data on rock failure at 200 kb confining pressure, this problem can only be explored indirectly. If we assume diffusion creep to be the mechanism of deformation (Gordon 1965; Orowan 1967; Carter & Ave'Lallemant 1970; Raleigh & Kirby 1970; Weertman 1970; Goetze 1971), we can calculate the strain rate $\dot{\varepsilon}$:

$$\dot{\varepsilon} = 5.37 \times 10^{10} \times \exp\left(-\frac{H+V_{ac}P}{RT}\right)\sigma^{2.3} \qquad (10)$$

where H = activation enthalpy, V_{ac} = activation volume, P = hydrostatic pressure, R = gas constant, T = temperature (°K), and σ = maximum shear stress. We can also compute the effective viscosity η:

$$\eta = \frac{\sigma}{\dot{\varepsilon}} \qquad (11)$$

Taking our calculated value for stress (i.e., σ = 500 bars), and H = 100 kcal/mole, V_{ac} = 40 cm^3/mole (Goetze 1971, and personal communication) and the temperature in the center

of the slab from Fig. 3, we find within 20 km of the center the effective viscosity is greater than $\eta = 10^{27}$ poise for virtually the full length of the slab. This value is indeed very high, and it implies a very low creep rate inside the slab. The slab behaves nearly elastically, and uniform creep cannot relieve the stresses. It is necessary to have either accelerated creep or brittle fracture to occur in response to stress concentrations. In the case of accelerated creep, however, the maximum deformation must take place over a very narrow (low aspect ratio) volume to produce the equivalent of a dislocation model for the seismic source. This mechanism is in agreement with the creep model described by Griggs (1972) based on experiments with dunite.

The maximum depth of earthquakes is also of great interest. No earthquakes have been observed below a depth of 730 km, and many seismic zones terminate at shallower depths. The absence of well-defined travel time anomalies for deep focus earthquakes indicates that a well-defined slab does not exist for a significant distance below the earthquakes (Toksöz et al. 1971; Mitronovas & Isacks 1971; Sen Gupta & Julian 1973). A broad region of somewhat reduced temperature or a weak continuation of the slab below the depth of maximum earthquakes cannot be excluded by the data.

This limited depth of earthquakes may be explained by either the absence of stresses necessary to produce earthquakes

or by the absence of material which would undergo brittle failure. These two are related since the temperature plays a strong role in both cases. Below a depth of 650 km, the interior of the descending slab rapidly reaches thermal equilibrium because of efficient radiative heat transfer. Yet equilibration through thermal conduction is not likely to be the sole cause of a maximum depth for earthquakes, as earthquakes in some seismic zones such as Tonga do not become progressively rarer with depth (Isacks et al. 1968). It is likely that the 650 km phase change rises to shallower depths in the slab and produces the stress for earthquakes below 650 km (Smith & Toksöz 197?). The seismicity of the small deteched segments of the slabs under New Hebrides and under Tonga can also be explained by the stresses due to this phase boundary and the resistance of the lower mantle.

Mechanisms of Shallow Earthquakes in Convergence Zones

There are a large number of shallow earthquakes that also occur in the convergence zones, under or near the trenches. There is a general agreement regarding the mechanisms of these shallow earthquakes. On the basis of locations and source mechanisms these can be divided into two categories:

1. The shallow earthquakes associated with normal faults in the oceanic side of the trenches are probably due to tension in the outer layer of the lithosphere arising

from the bending of the slab and the upward buckling (Stauder 1968b; Hanks 1971; Kanamori 1971). Generally these earthquakes are not very large and do not cut across the lithosphere (the Sanriku earthquake of 1933 may be an exception). The net stress in the lithosphere may be compressive as evidenced from the earthquakes discussed below.

2. The second group of shallow earthquakes associated with subduction occurs along the shear zone between the down-going slab and the continental lithosphere. Many major earthquakes are associated with thrust zones and fall in this category. The dip of the fault plane is generally less than about 30°. Some examples of these are the Chile earthquake of 1960, the Alaska earthquake of 1964 (Plafker 1972), and the Rat Island earthquake of 1965 (Stauder 1968a). This type of earthquake is also prevalent in regions where continental lithospheric plates converge. The earthquakes in the southern Iran thrust belt (Nowroozi 1972) are good examples of this category.

We should clarify that in all the above areas some events not matching the two generalized categories do occur (e.g., strike slip faults). Considering the immensely complicated crustal features, tears in the plates, and localized stress concentrations, faults along other orientations and earthquakes of differing source mechanisms would and do occur.

Thus the previous generalizations about earthquake characteristics represent the predominant types rather than all earthquakes in the convergence areas.

CONCLUSIONS

Our understanding of deep earthquakes and the evolution of the descending lithosphere relies upon what inferences can be extracted from observations and from predictions using theoretical and laboratory work. Here theoretical calculations of the thermal regime, the seismic velocity structure, and the stress in the descending lithosphere provide the predictions; and these are in good agreement with relevant observations. A major contribution of the theoretical calculations - in addition to verifying the hypothetical models - has been their ability to identify the significant parameters that control the evolution and properties of the descending lithosphere. Some major conclusions of this study are:

1. The temperatures inside the slab are strongly controlled by the time elapsed after initiation of the descent and by the conductivity, especially the radiative term. The gross structure of the thermal regime is insensitive to reasonable variations in the parameters.
2. The maximum depth of penetration is strongly influenced by the 650 km phase change, and by the increase in the radiative contribution to effective thermal conductivity. Temperature anomalies do not extend beyond 700 km if the

above phase change is exothermic. In all cases, however, the slab is thermally assimilated into the mantle at some depth shallower than about 800 km.

3. For convergence of continental plates, the underthrusting lithosphere generally does not penetrate very deep. Orogeny associated with continental collisions most likely occurs either during the collision or later when the subducted continent becomes heated.
4. From the comparison of travel time anomalies associated with the LONGSHOT explosion and the calculated values based on theoretical temperatures and velocities, the intermediate depth earthquakes are located within the coolest region of the slab under the Aleutians. This also seems to be the case in the Tonga region and under Japan as inferred from the velocity anomalies and attenuation of seismic waves.
5. Stress calculations show that the maximum shear stress occurs within the coolest region of the slab for a reasonable temperature-dependent rheology.
6. The regional stress patterns depend upon the temperature field, the slab rheology, dip of the slab, and mantle support. The last item, the mantle's support of the slab, may be influenced by the descent velocity, convection, phase changes, and lateral differences within the mantle such as under oceans or continents.

7. The magnitude of the calculated shear stress within the slab is about 500-1000 bars. This is a reasonable value as inferred from estimates of the stress drop for deep-focus earthquakes. The orientation of the theoretical principal stresses are in very good agreement with those determined from focal mechanism studies of intermediate and deep-focus earthquakes. The center of the slab is sufficiently cold to allow either accelerated creep or brittle fracture to occur in response to stress concentrations.

ACKNOWLEDGEMENTS

This research was supported by the Advanced Research Projects Agency of the Department of Defense and was monitored by the Air Force Office of Scientific Research under Contract No. F44620-71-C-0049 and by NSF Grant GA-29358. One of the authors (NHS) was supported by a NSF fellowship during part of the research, and another (ATS) was supported by a Hertz Foundation Fellowship.

REFERENCES

Abe, K., 1972a. Seismological evidence for a lithospheric tearing beneath the Aleutian arc, Earth Planet. Sci. Letters, 14, 428-432.

Abe, K., 1972b. Lithospheric normal faulting beneath the Aleutian trench, Phys. Earth Planet. Interiors, 5, 190-198.

Akimoto, S., 1970. High pressure synthesis of "modified" spinel and some geophysical implications, Phys. Earth Planet. Interiors, 3, 189-195.

Akimoto, S., & Fujisawa, H., 1968. Olivine-spinel solid solution equilibria in the system Mg_2SiO_4-Fe_2SiO_4, J. geophys. Res., 73, 1467-1479.

Anderson, D.L., 1967. Phase changes in the upper mantle, Science, 157, 1165-1173.

Archambeau, C.B., Flinn, E.A. & Lambert, D.G., 1969. Fine structure of the upper mantle, J. geophys. Res., 74, 5825-5865.

Armstrong, R., 1968. A model for the evolution of strontium and lead isotopes in a dynamic earth, Rev. Geophys., 6, 175-199.

Barazangi, M. & Dorman, J., 1969. World seismicity maps compiled from ESSA, Coast and Geodetic Survey, Epicenter Data, 1961-1967, Bull. seism. Soc. Am., 59, 369-380.

Birch, F., 1968. Thermal expansion at high pressures, J. geophys. Res., 73, 817-819.

Carter, N.L. & Ave'Lallemant, H.G., 1970. High temperature flow of dunite and peridotite, Bull. geol. Soc. Am., 81, 2181-2202.

Cathles, L.W., 1971. The viscosity of the earth's mantle, Ph.D. thesis, Princeton University.

Christensen, R.M., 1971. Theory of viscoelasticity - an introduction, pp. 31-78, Academic Press, New York.

Davies, D. & Julian, B., 1972. A study of short period P-wave signals from Longshot, Geophys. J. R. astr. Soc., 29, 185-202.

Davies, D. & McKenzie, D.P., 1969. Seismic travel-time residuals and plates, Geophys. J. R. astr. Soc., 18, 51-63.

Engdahl, R., 1971. Explosion effects and earthquakes in the Amchitka Island region, Science, 173, 1232-1235.

Goetze, C., 1971. Low stress creep measurements on natural rock specimens (abstract), Trans. Am. Geophys. Union, 52, 347.

Gordon, R.B., 1965. Diffusion creep in the earth's mantle, J. geophys. Res., 70, 2413-2418.

Griggs, D.T., 1972. The sinking lithosphere and the focal mechanism of deep earthquakes, in Nature of the Solid Earth, ed. Eugene C. Robertson, McGraw-Hill.

Grow, J.A., 1972. A geophysical study of the central Aleutian arc, Ph.D. thesis, University of California, San Diego.

Gutenberg, B. & Richter, C.F., 1954. Seismicity of the Earth, 2nd ed., 310 pp., Princeton University Press, Princeton, N.J.

Hanks, T.C., 1971. The Kuril trench - Hokkaido rise system: large shallow earthquakes and simple models of deformation, Geophys. J. R. astr. Soc., 23, 173-189.

Hanks, T. & Whitcomb, J., 1971. Comments on paper by J.W. Minear and M. Nafi Toksöz, "Thermal regime of a downgoing slab and new global tectonics," J. geophys. Res., 76, 613-616.

Hasebe, K., Fujii, N. & Uyeda, S., 1970. Thermal processes under island arcs, Tectonophysics, 10, 335-355.

Honda, H., 1934. On the mechanism of deep earthquakes and the stress in the deep layer of the earth's crust, Geophys. Magazine, Tokyo, 8, 179-185.

Hurley, P., 1968a. Absolute abundance and distribution of Rb, K, and Sr in the earth, Geochim. Cosmochim. Acta, 32, 273-283.

Hurley, P., 1968b. Correction to "Absolute abundance and distribution of Rb, K, and Sr in the earth", Geochim. Cosmochim. Acta, 32, 1025-1030.

Isacks, B., Oliver, J. & Sykes, L., 1968. Seismology and the new global tectonics, J. geophys. Res., 73, 5855-5899.

Isacks, B. & Molnar, P., 197[illegible] Distribution of stresses in the descending lithosphere from a global survey of focal-mechanism solutions of mantle earthquakes, Rev. Geophys. Space Phys., 9, 103-174.

Jacob, K., 1970. Three-dimensional seismic ray tracing in a laterally heterogeneous spherical earth, J. geophys. Res., 75, 6675-6689.

Jacob, K., 1972. Global tectonic implications of anomalous seismic travel times from the nuclear explosion Longshot, J. geophys. Res., 77, 2556-2573.

Johnson, L.R., 1967. Array measurements of P velocities in the upper mantle, J. geophys. Res., 72, 6309-6325.

Julian, B. & Anderson, D., 1968. Travel times, apparent velocities and amplitudes of body waves, Bull. seism. Soc. Am., 58, 339-366.

Kanamori, H., 1971. Seismological evidence for a lithospheric normal faulting - the Sanriku earthquake of 1933, Phys. Earth Planet. Interiors, 4, 289-300.

Katsumata, M., 1967. Seismic activities in and near Japan, 3: Seismic activities versus depth (in Japan), J. seism. Soc. Japan., 20, 75.

Kay, R., Hubbard, N. & Gast, P., 1970. Chemical characteristics and the origin of oceanic ridge volcanic rocks, J. geophys. Res., 75, 1585-1613.

Kondorskaya, N.V. & Postolenko, G.A., 1959. Analysis of observations on earthquakes occurring in the Kurilian-Kamchatka region, Akad. Navk. SSSR Isv. Ser. Geofiz., No. 10, 1448-1454.

LePichon, X., 1968. Sea-floor spreading and continental drift, J. geophys. Res., 73, 3661-3697.

MacDonald, G.J.K., 1959. Calculations on the thermal history of the earth, J. geophys. Res., 64, 1967-2000.

MacDonald, G., 1963. The deep structure of continents, Rev. Geophys., 1, 587-665.

McConnell, R.K., Jr., 1968. Viscosity of the earth's mantle, in Proc. Conf. History Earth's Crust, 1966, ed. R.A. Phinney, Princeton University Press, Princeton, N.J.

McKenzie, D.P., 1969. Speculation on the consequences and causes of plate motion, Geophys. J.R. astr. Soc., 18, 1-32.

Mendiguren, J., 1972. Source mechanism of a deep earthquake from analysis of world wide observations of free oscillation, Ph.D. Thesis, Massachusetts Institute of Technology.

Minear, J.W. & Toksöz, M.N., 1970. Thermal regime of a downgoing slab and new global tectonics, J. geophys. Res., 75, 1397-1419.

Minear, J.W. & Toksöz, M.N., 1970. Thermal regime of a downgoing slab, Tectonophysics, 10, 367-390.

Mitronovas, W. & Isacks, B., 1971. Seismic velocity anomalies in the upper mantle beneath the Tonga-Kermadec island arc, J. geophys. Res., 76, 7154-7180.

Mitronovas, W., Isacks, B. & Seeber, L., 1969. Earthquake locations and seismic wave propagation in the upper 250 km of the Tonga island arc, Bull. seism. Soc. Am., 59, 1115-1135.

Nowroozi, A.A., 1972. Focal mechanism of earthquakes in Persia, Turkey, West Pakistan and Afghanistan and plate tectonics of the Middle East, Bull seism. Soc. Am., 62, 823-850.

Oliver, J. & Isacks, B., 1967. Deep earthquake zones, anomalous structures in the upper mantle and the lithosphere, J. geophys. Res., 72, 4259-4275.

Orowan, E., 1967. Island arcs and convection, Geophys. J.R. astr. Soc., 14, 385-393.

Peaceman, D. & Rachford, H., 1955. The numerical solution of parabolic and elliptic differential equations, J. Soc. Ind. Appl. Math., 3, 28-41.

Plafker, G., 1972. Alaskan earthquake of 1964 and Chilean earthquake of 1960: implications for arc tectonics, J. geophys. Res., 77, 901-925.

Press, F., 1970. Earth models consistent with geophysical data, Phys. Earth Planet. Interiors, 3, 3-22.

Raleigh, C.B. & Kirby, S.H., 1970. Strength of the upper mantle, in The mineralogy and petrology of the upper mantle, ed. B.A. Morgan, Mineral Soc. Am. Special Paper, 3, 113-121.

Ringwood, A.E., 1970. A phase transformation and the constitution of the mantle, Phys. Earth Planet. Interiors, 3, 109-155.

Ringwood, A.E., 1972. Phase transformations and mantle dynamics, Earth Planet. Sci. Letters, 14, 233-241.

Ringwood, A.E. & Major, A., 1970. The system Mg_2O_4-Fe_2SiO_4 at high pressures and temperatures, Phys. Earth Planet. Interiors, 3, 89-108.

Schatz, F.J., 1971. Thermal conductivity of earth materials at high temperatures, Ph.D. Thesis, Massachusetts Institute of Technology.

Schatz, F.J. & Simmons, G., 1972. Thermal conductivity of earth materials at high temperatures, J. geophys. Res., 77, 6966-6983.

Schubert, G. & Turcotte, D.L., 1971. Phase changes and mantle convection, J. geophys. Res., 76, 1424-1432.

Sclar, C.B., Carrison, L.C. & Schwartz, C.M., 1964. High-pressure reaction of clinoenstatite to forsterite plus stishovite, J. geophys. Res., 69, 325-330.

Sen Gupta, M. & Julian, B., 1973. P-travel times for deep focus earthquakes, Bull. seism. Soc. Am., to be submitted.

Skinner, B.J., 1966. Thermal expansion, in Handbook of Physical Constants, Geol. Soc. Am. Mem., 97, 75-96.

Sleep, N., 1973. Teleseismic P-wave transmission through slabs, Bull. seism. Soc. Am., in press.

Smith, A.T. & Toksöz, M.N., 1972. Stress distribution beneath island arcs, Geophys. J.R. astr. Soc., 29, 289-318.

Sorrells, G., Crowley, J. & Veith, K., 1971. Methods for computing ray paths in complex geologic structures, Bull. seism. Soc. Am., 61, 27-53.

Stauder, W., 1968. Mechanism of the Rat Island earthquake sequence of February 4, 1965, with relation to island arcs and sea floor spreading, J. geophys. Res., 73, 3847-3858.

Stauder, W., 1968. Tensional character of earthquake foci beneath the Aleutian Trench with relation to sea floor spreading, J. geophys. Res., 73, 7693-7701.

Sykes, L.R., 1966. The seismicity and deep structure of island arcs, J. geophys. Res., 71, 2981-3006.

Sykes, L.R., Isacks, B.L. & Oliver, J., 1969. Spatial distribution of deep and shallow earthquakes of small magnitude in the Fiji-Tonga region, Bull. seism. Soc. Am., 59, 1093-1113.

Tillman, C.C., 1971. On-line solution of elliptic boundary-value problems, Ph.D. Thesis, Massachusetts Institute of Technology.

Toksöz, M.N., Chinnery, M. & Anderson, D., 1967. Inhomogeneities in the earth's mantle, Geophys. J.R. astr. Soc., 13, 31-59.

Toksöz, M.N., Minear, J.W. & Julian, B.R., 1971. Temperature field and geophysical effects of a downgoing slab, J. geophys. Res., 76, 1113-1138.

Turcotte, D.L. & Oxburgh, E.R., 1969. Convection in a mantle with variable physical properties, J. geophys. Res., 74, 1458-1474.

Turcotte, D.L. & Oxburgh, E.R., 1969. A fluid theory for the deep structure of dip-slip fault zones, Phys. Earth Planet. Interiors, 1, 381-386.

Utsu, T., 1971. Seismological evidence for anomalous structure of island arcs with special reference to the Japanese region, Rev. Geophys. Space Phys., 9, 839-890.

Verhoogen, J., 1951. The adiabatic gradient in the mantle, Trans. Am. Geophys. Union, 32, 41-42.

Verhoogen, J., 1965. Phase changes and convection in the earth's mantle, Trans. Roy. Soc. London, A, 258, 276-283.

Wadati, K., 1935. On the activity of deep-focus earthquakes in the Japan Island and neighborhood, Geophys. Magazine, Tokyo, 8, 305-326.

Weertman, J., 1970. The creep strength of the earth's mantle, Rev. Geophys. Space Phys., 8, 145-168.

Wyss, M. & Molnar, P., 1972. Source parameters of intermediate and deep focus earthquakes in the Tonga arc, Phys. Earth Planet. Interiors, 6, 279-292.

Zienkiewicz, O.C., 1971. The Finite Element Method in Engineering Sciences, 521 pp., McGraw-Hill, London.

FIGURE CAPTIONS

Fig. 1 Schematic representation of the computational scheme, input parameters, and boundary conditions used to calculate thermal models of slabs (Modified after Minear & Toksöz 1970a).

Fig. 2 Temperatures inside the base slab model after 3.6 m.y. and 7.1 m.y. were calculated using the parameters given in the text. The velocity of the slab is 8 cm/yr.

Fig. 3 The slab in Fig. 2 after 10.7 m.y. Penetration through the phase transition at 600 km depth, and the latent heat of the phase transition help heat and thermally equilibrate the slab interior below this depth.

Fig. 4 Temperature field of the slab calculated using Schatz & Simmons (1972) conductivity. All other parameters same as those in Fig. 3. Due to lower conductivity, this slab penetrates the 600 km phase change.

Fig. 5 Temperature field of the slab (shown in Fig. 3) after 16 m.y. The penetration of the slab was stopped at 10.7 m.y., and the slab remained at rest for 5.3 m.y.

Fig. 6 The thermal fields of the slab in Fig. 5, after additional rest periods. The temperature anomaly becomes progressively broader with time.

Fig. 7 Temperature field in a slab penetrating into a mantle having a "convective" geotherm. The parameters used for this slab are self-consistent with the geotherm. Penetration of the slab was stopped at 10.7 m.y., and the lower right slab was allowed to equilibrate with the mantle for 3.6 m.y. The phase boundary at 650 km was not taken into account in this model, but the higher phase (350 km) boundary was included.

Fig. 8 Temperature field in subducted continent after 10 m.y. with extreme model of frictional heating along the fault plane. The highly radioactive continental crust is indicated by hatching.

Fig. 9 The temperature in a subducted continent after 7.7 m.y. (above), and after remaining stationary for an additional 47 m.y. (below). A thermal maximum has formed in the subducted crust. "M" indicates the base of the crust.

Fig. 10 Observed and calculated P-wave travel time anomalies for LONGSHOT explosion. The observed delays are station corrected and averaged over intervals of azimuth and distance as given by Abe (1972a). The fit is obtained by assuming the strike of the arc is N82W, and adjusting the slab relative to the LONGSHOT location.

Fig. 11 Temperature regime and the distribution of earthquake hypocenters in the Central Aleutians near Amchitka. The thermal model is obtained by combining the isotherms from two slabs dipping at different angles. The earthquake hypocenters are from Engdahl (1971). The focal mechanisms of two representative earthquakes show normal faulting in the oceanside of the trench and thrusting in the convergence zone beneath the arc. Note how intermediate earthquakes are in the coolest region of the slab and not in the shear zone.

Fig. 12 Density anomaly in gm/cm^3 within the descending slab using a typical thermal regime (in this case Fig. 2 of Smith & Toksöz, 1972). Only thermal volume contraction is used for the density calculations.

Fig. 13 Calculated maximum shear stress models for two different mantle supports, using the 30° dipping slab shown in Fig. 12. On the left the mantle support is given in terms of an 'effective' Young's modulus, E, versus depth. Section A-A' depicts the modulus within the slab which is temperature dependent. The arrows indicate the direction of the principal stress closest to down-dip, and the contours are maximum shear stress in bars. Shear stresses within the mantle are not contoured, but are generally lower than 200 bars.

Fig. 14 Comparison of theoretical model (top model, Fig. 13) to the seismicity of Japan given by Utsu (1971).

Fig. 15 Theoretical stresses and earthquake focal mechanisms for Honshu and Kermadec. On the left are the theoretical models. Both models have increasing support with depth for the mantle and strong temperature dependence for the slab rheology, although each is slightly different. The dips of the slabs are specified by the seismicity. On the right are focal mechanism solutions for each region, taken from Isacks & Molnar (1971), superimposed upon the plane of seismicity. Open circles show down-dip compression; filled circles indicate down-dip extension.

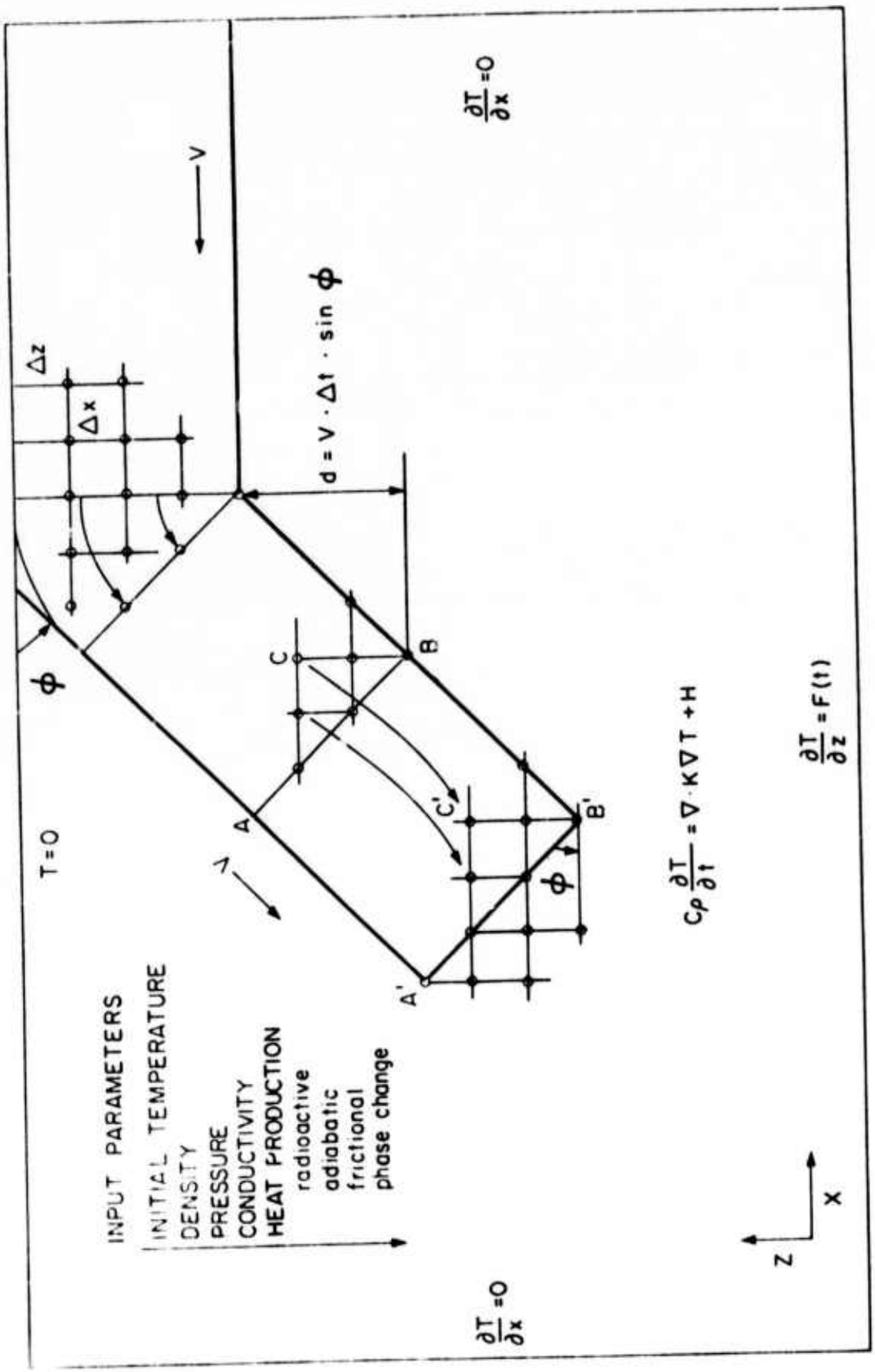
INPUT PARAMETERS
INITIAL TEMPERATURE
DENSITY
PRESSURE
CONDUCTIVITY
HEAT PRODUCTION
radioactive
adiabatic
frictional
phase change
T=0
$\frac{\partial T}{\partial x}=0$
$\frac{\partial T}{\partial x}=0$
$\frac{\partial T}{\partial z}=F(t)$
$C\rho\frac{\partial T}{\partial t}=\nabla\cdot K\nabla T+H$
$d=V\cdot\Delta t\cdot\sin\phi$
Δz
Δx
V
ϕ
A
B
C
A'
B'
C'
Z
X

Fig. 1

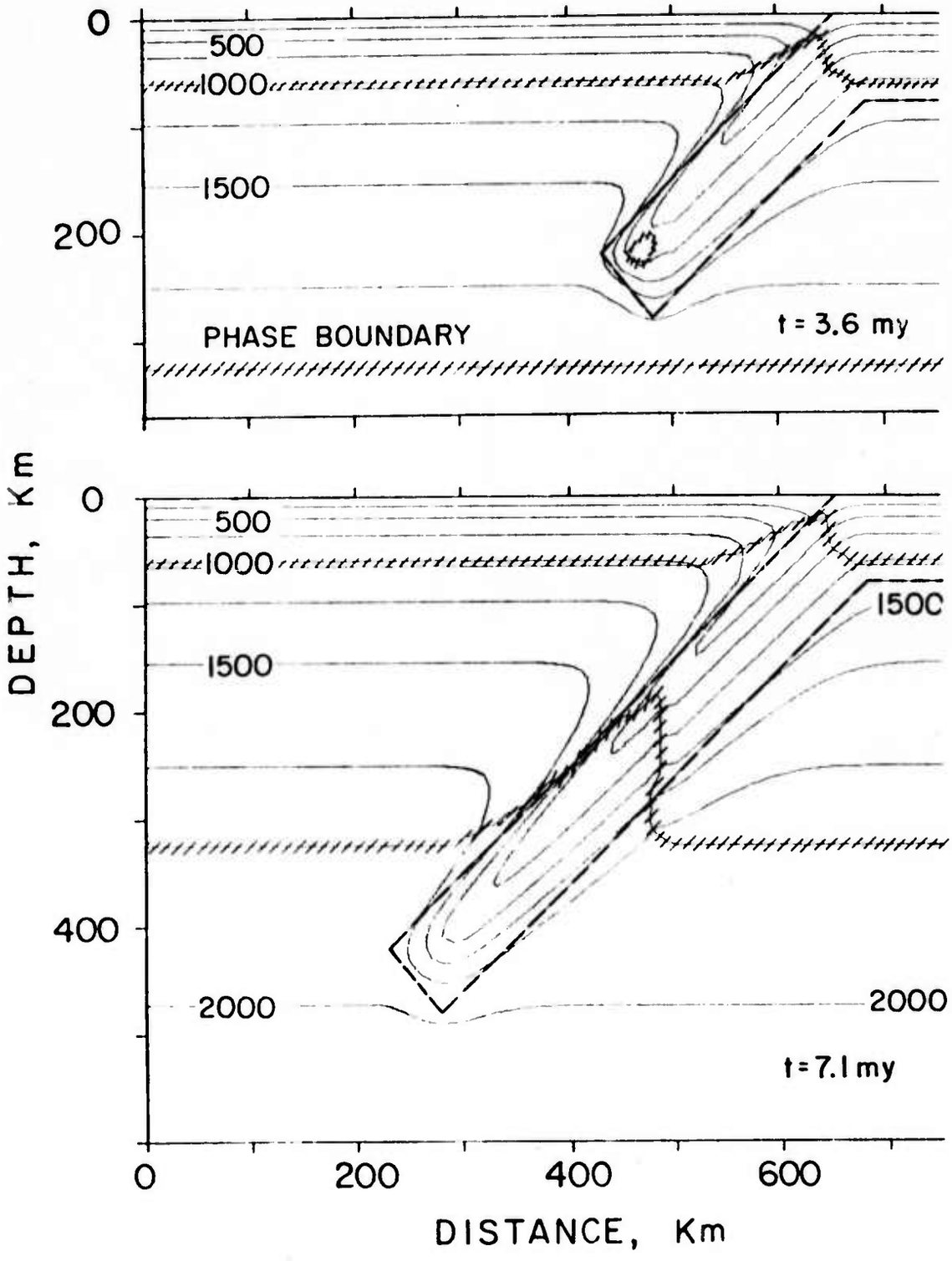
0
500
1000
1500
200
PHASE BOUNDARY
t = 3.6 my
DEPTH, Km
0
500
1000
1500
1500
200
400
2000
2000
t = 7.1 my
0
200
400
600
DISTANCE, Km

Fig. 2

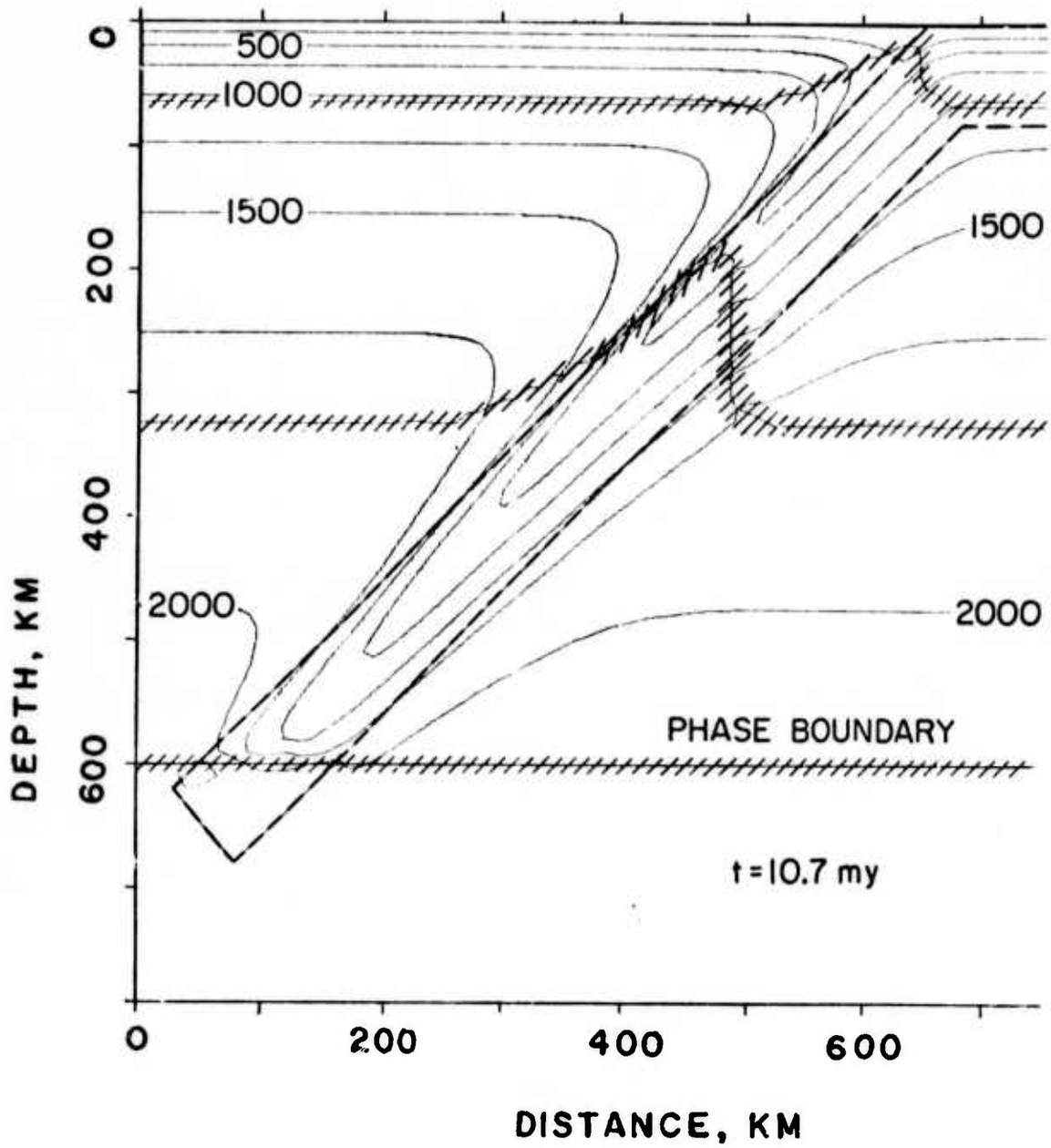
0
200
400
600
DEPTH, KM
500
1000
1500
2000
1500
2000
PHASE BOUNDARY
t = 10.7 my
0
200
400
600
DISTANCE, KM

Fig. 3

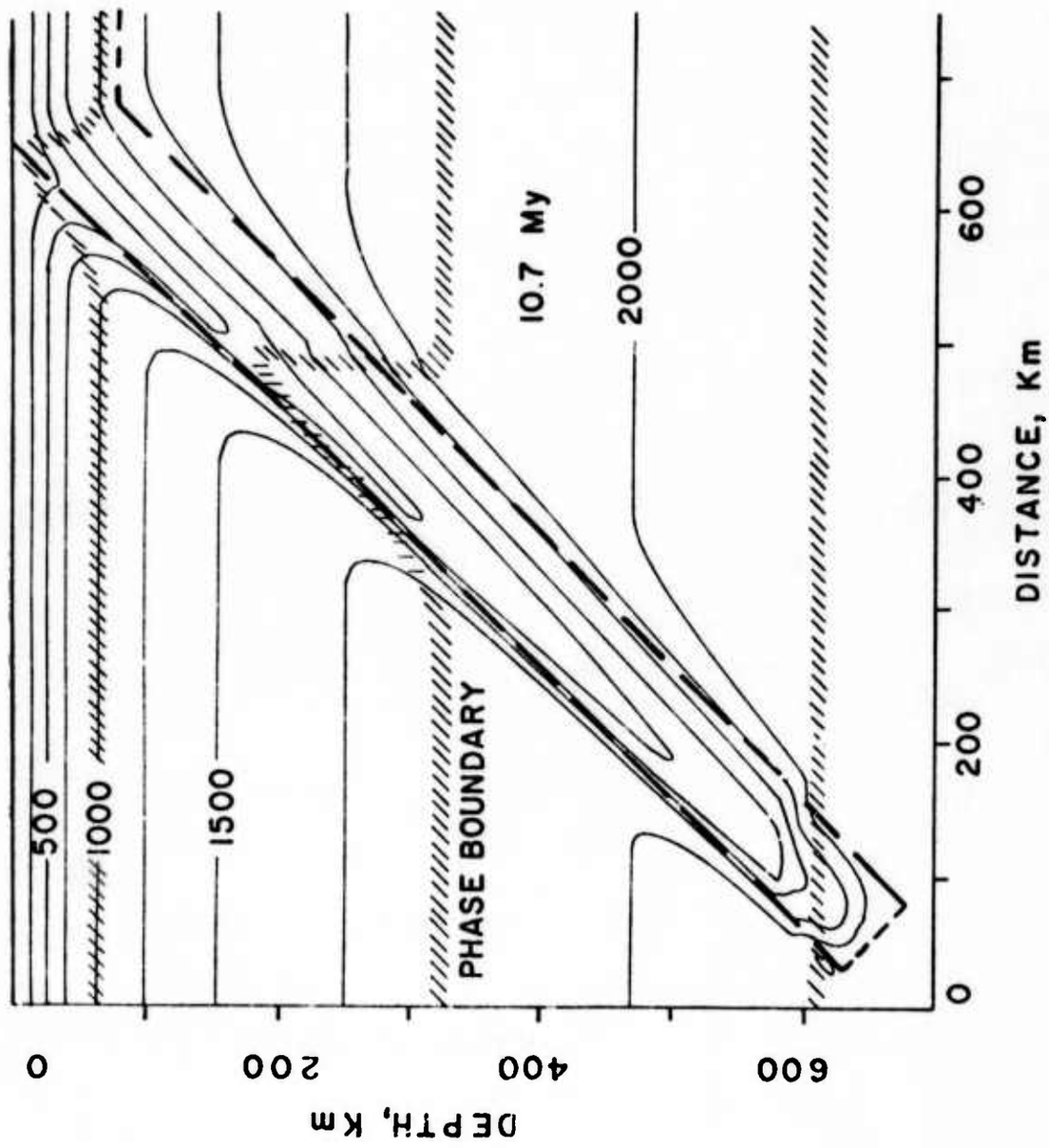
500
1000
1500
2000
10.7 My
PHASE BOUNDARY
0
200
400
600
DISTANCE, Km
0
200
400
600
DEPTH, Km

Fig. 4

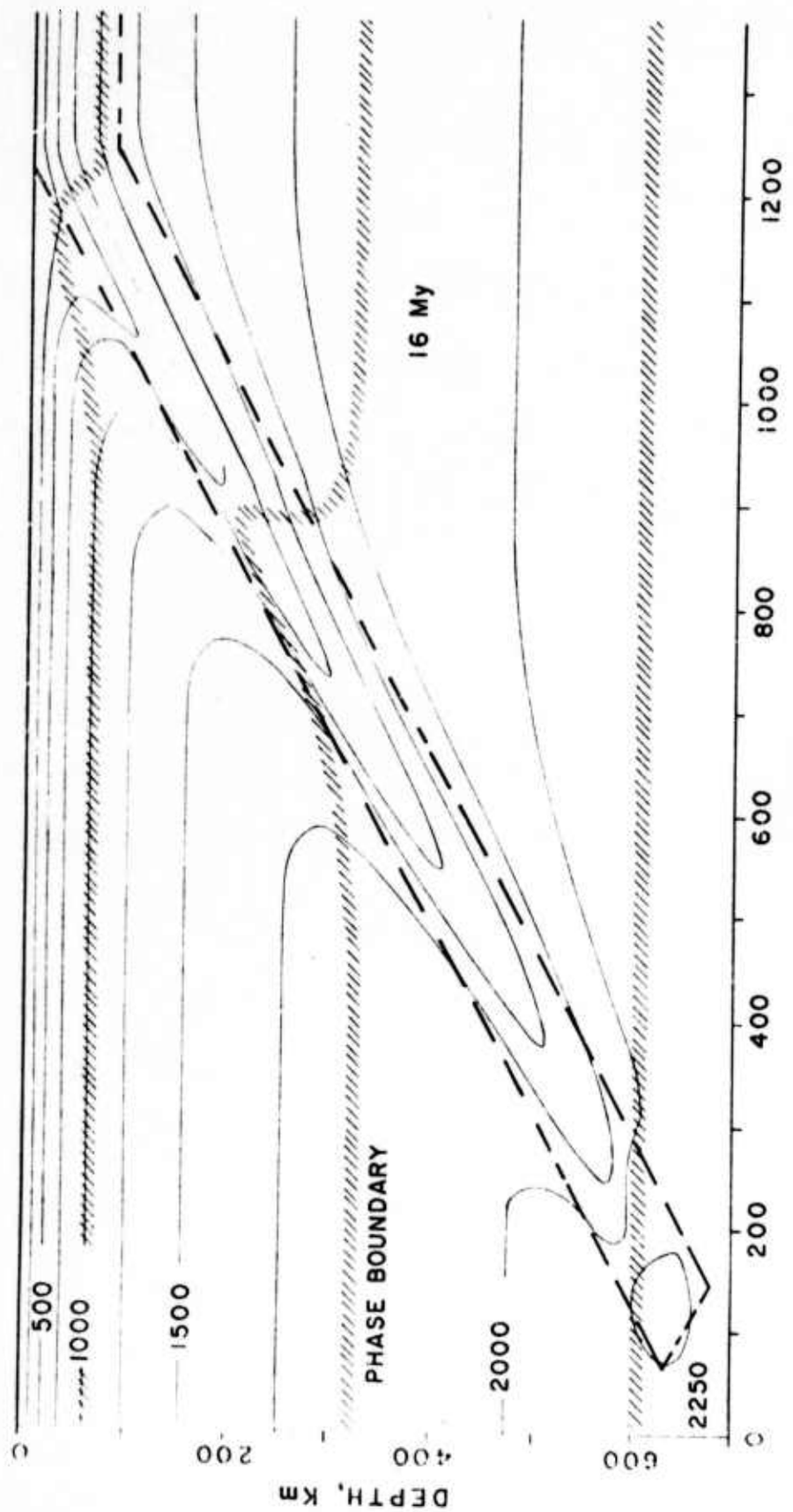
16 My
PHASE BOUNDARY
500
1000
1500
2000
2250
0
200
400
600
800
1000
1200
DISTANCE, Km
DEPTH, Km
0
200
400
600

Fig. 5

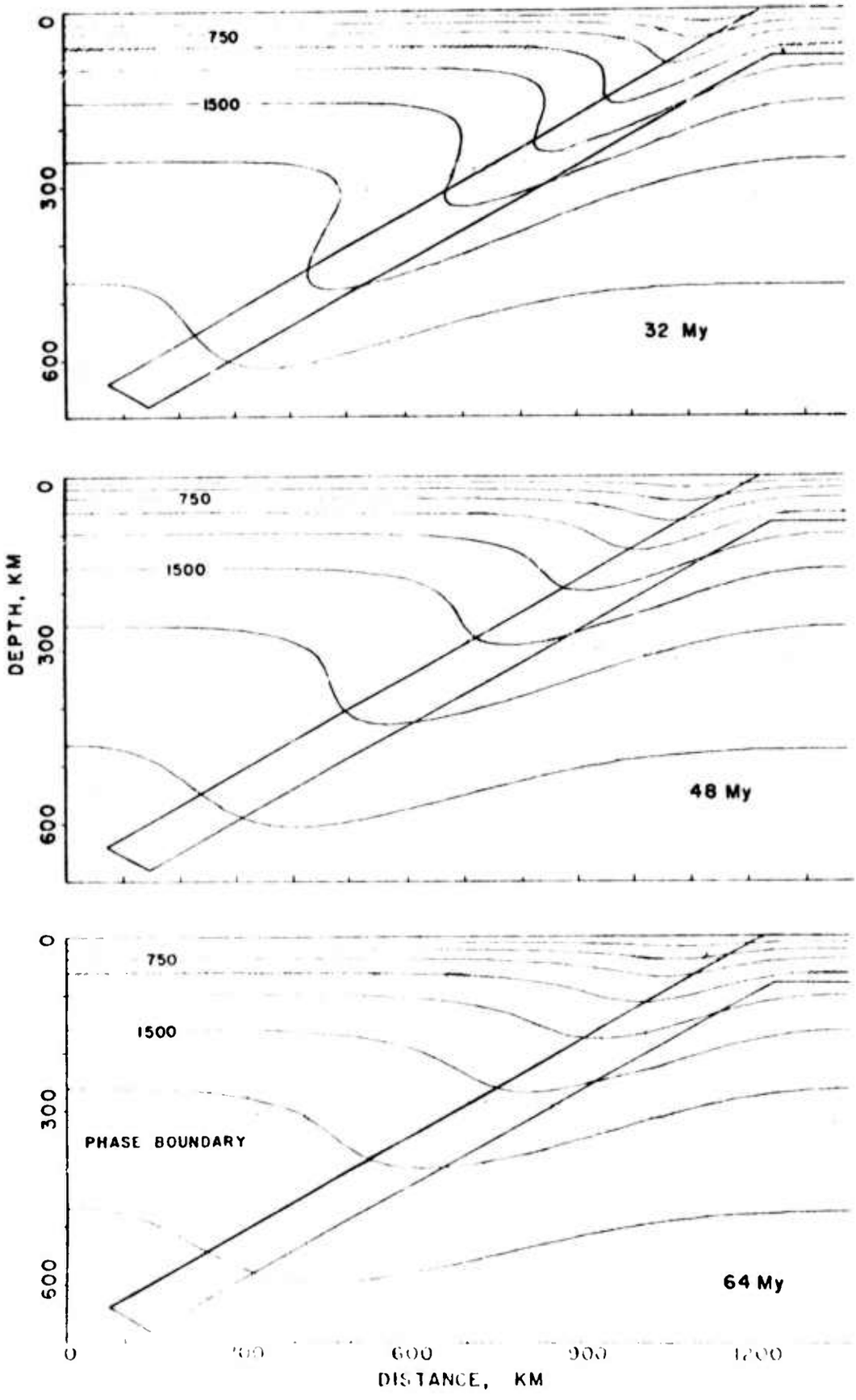
0
300
600
750
1500
32 My
48 My
64 My
DEPTH, KM
PHASE BOUNDARY
0
600
900
1200
DISTANCE, KM

Fig. 6

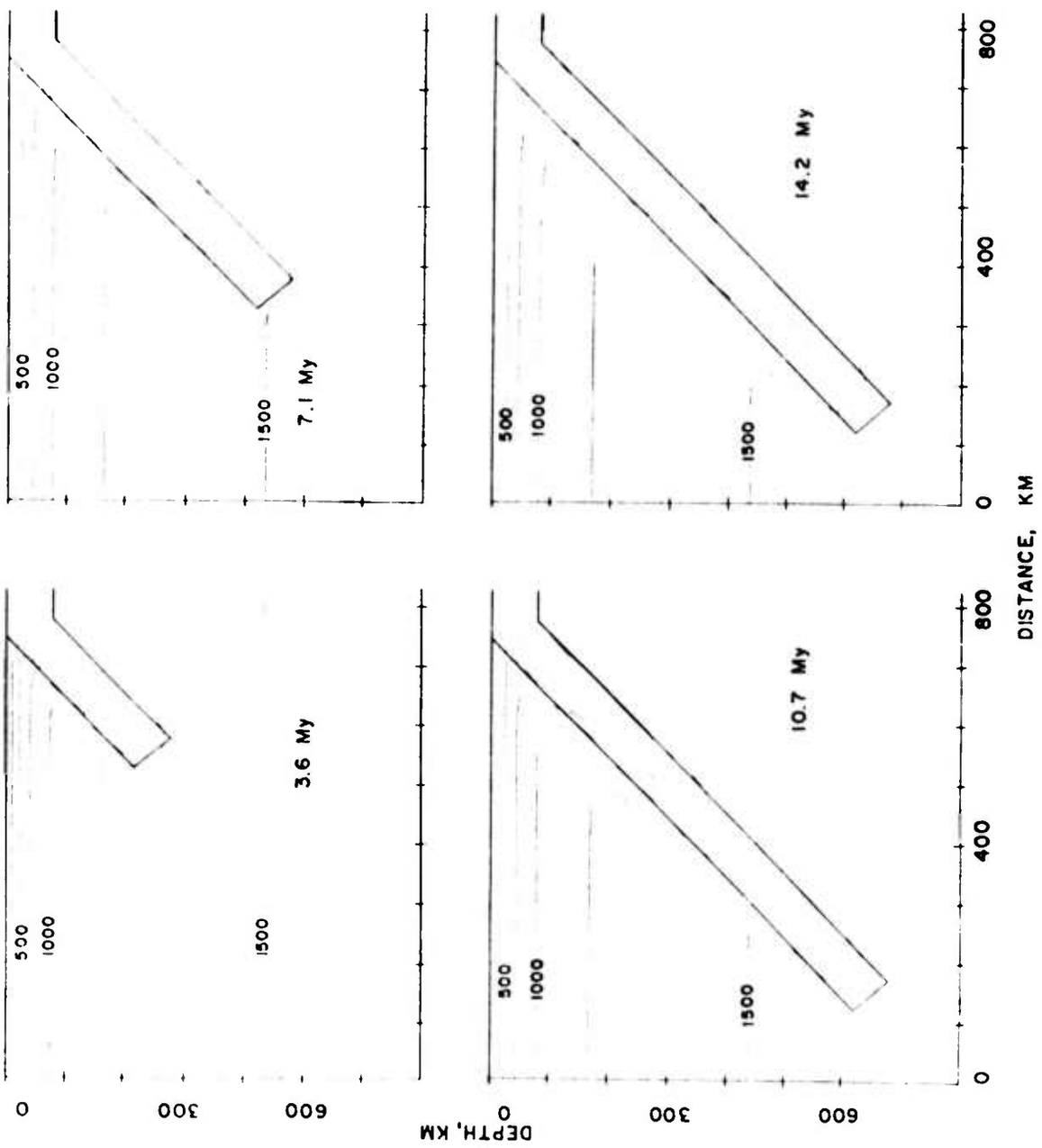
3.6 My
7.1 My
10.7 My
14.2 My
500
1000
1500
0
300
600
400
800
DEPTH, KM
DISTANCE, KM

Fig. 7

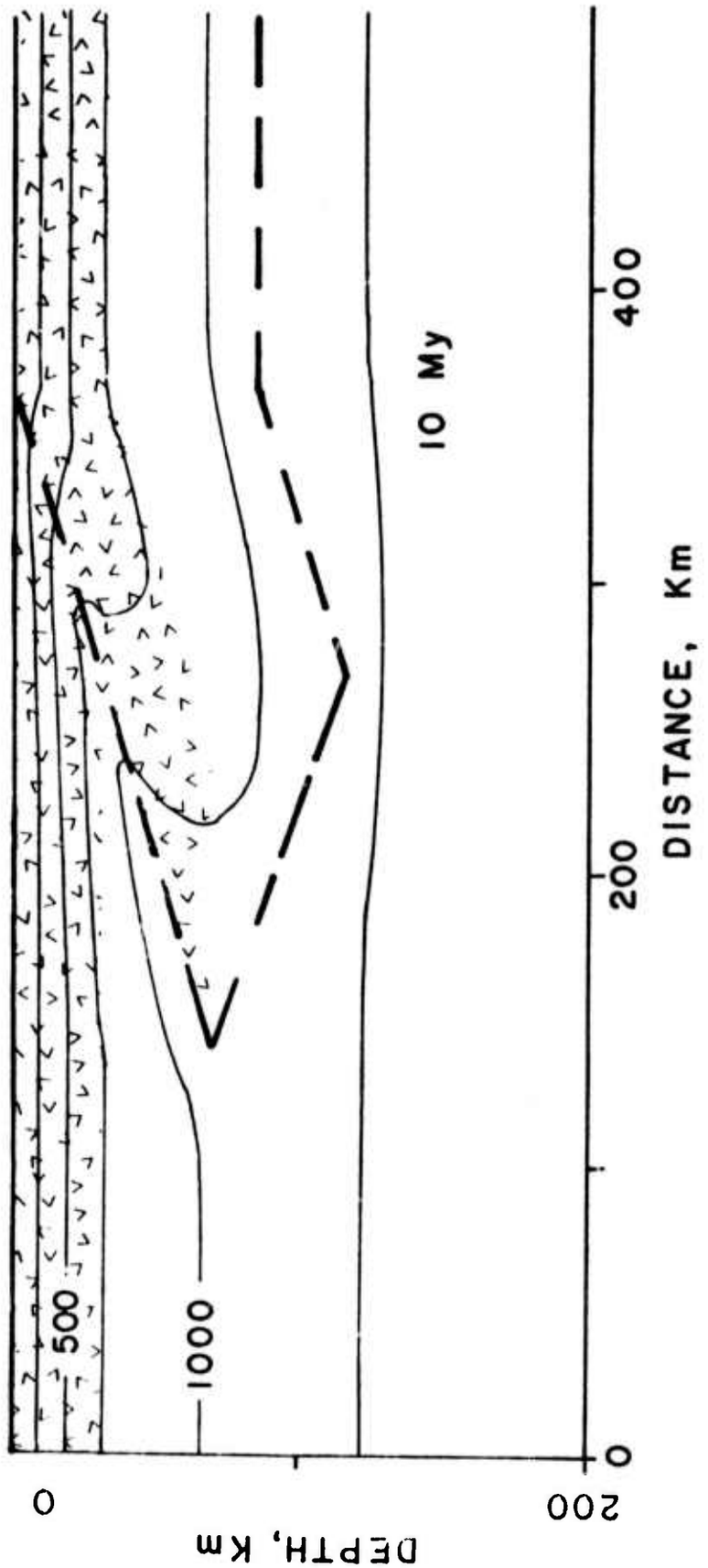

Fig. 8

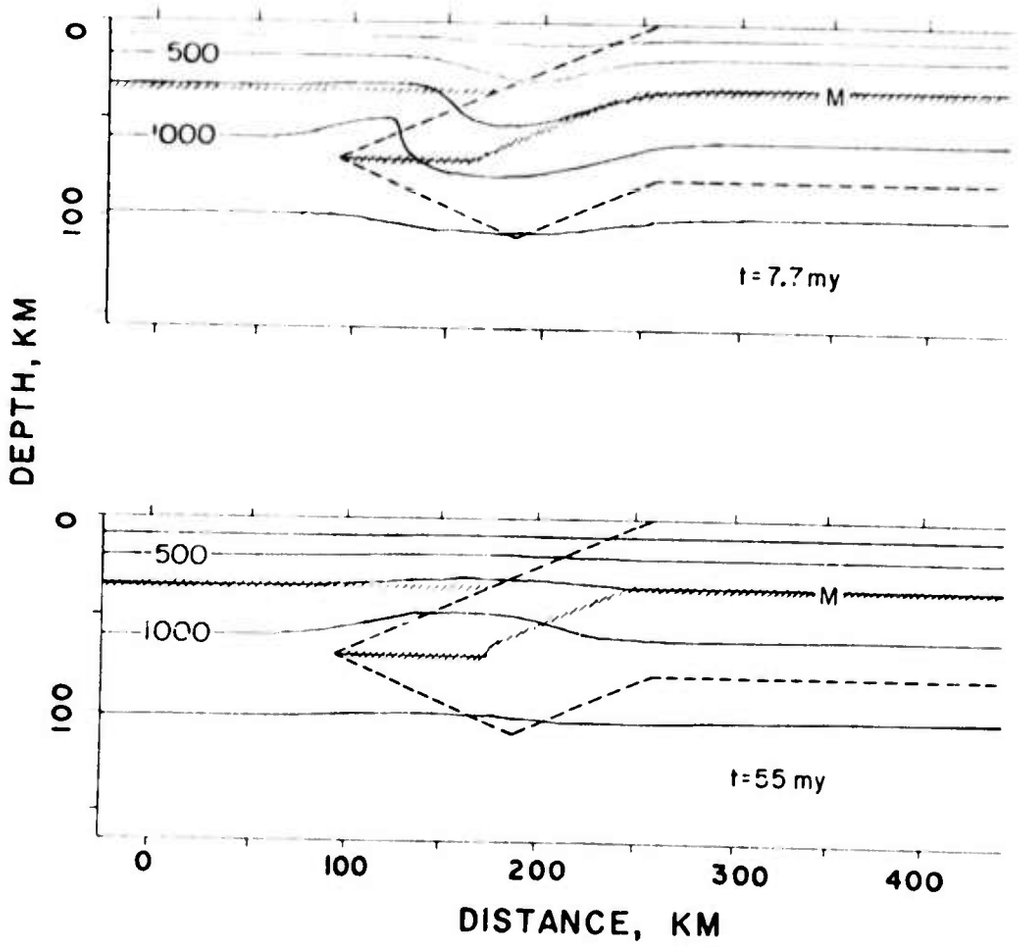
0
500
1000
M
100
t=7.7my
DEPTH, KM
0
500
1000
M
100
t=55 my
0
100
200
300
400
DISTANCE, KM

Fig. 9

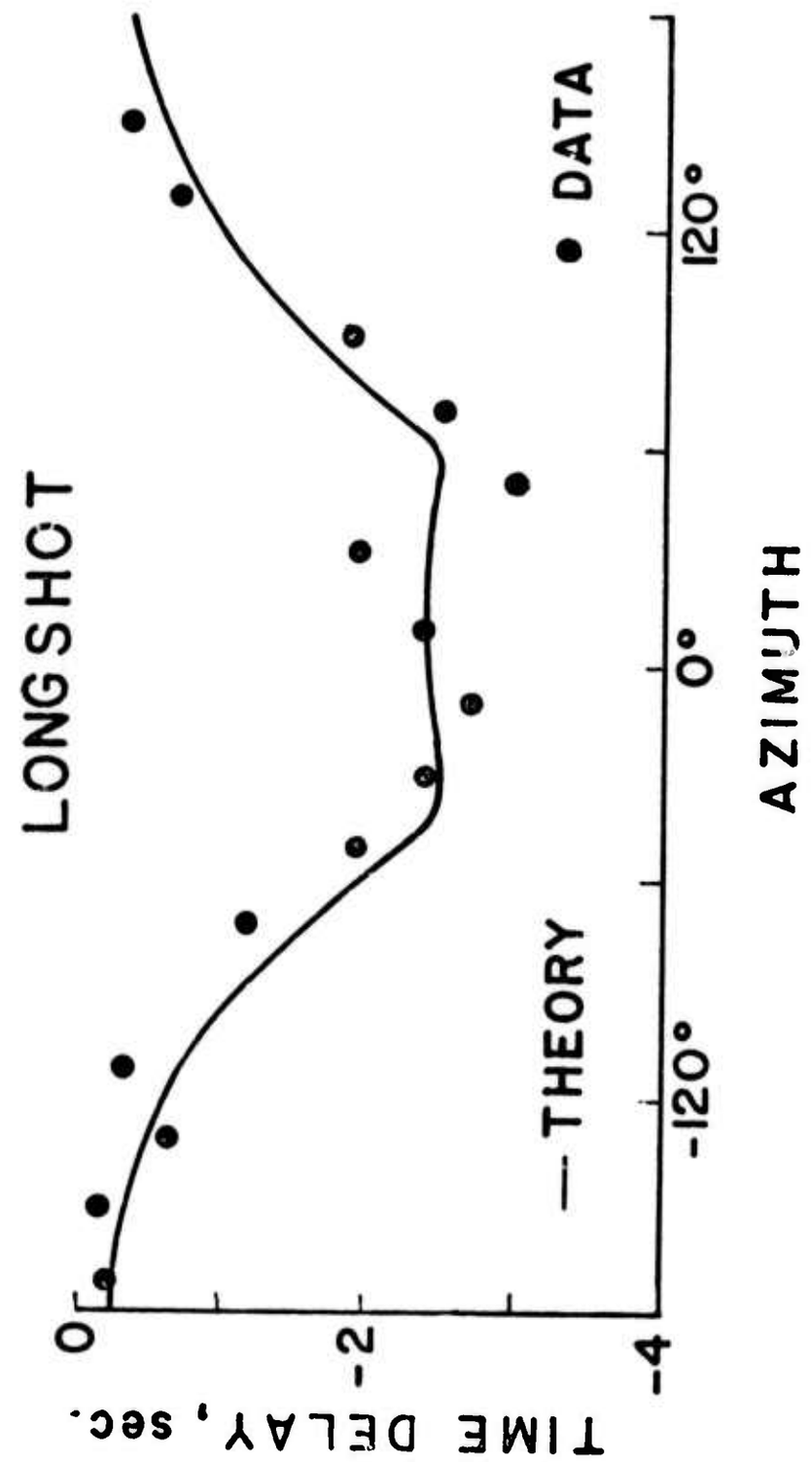

Fig. 10

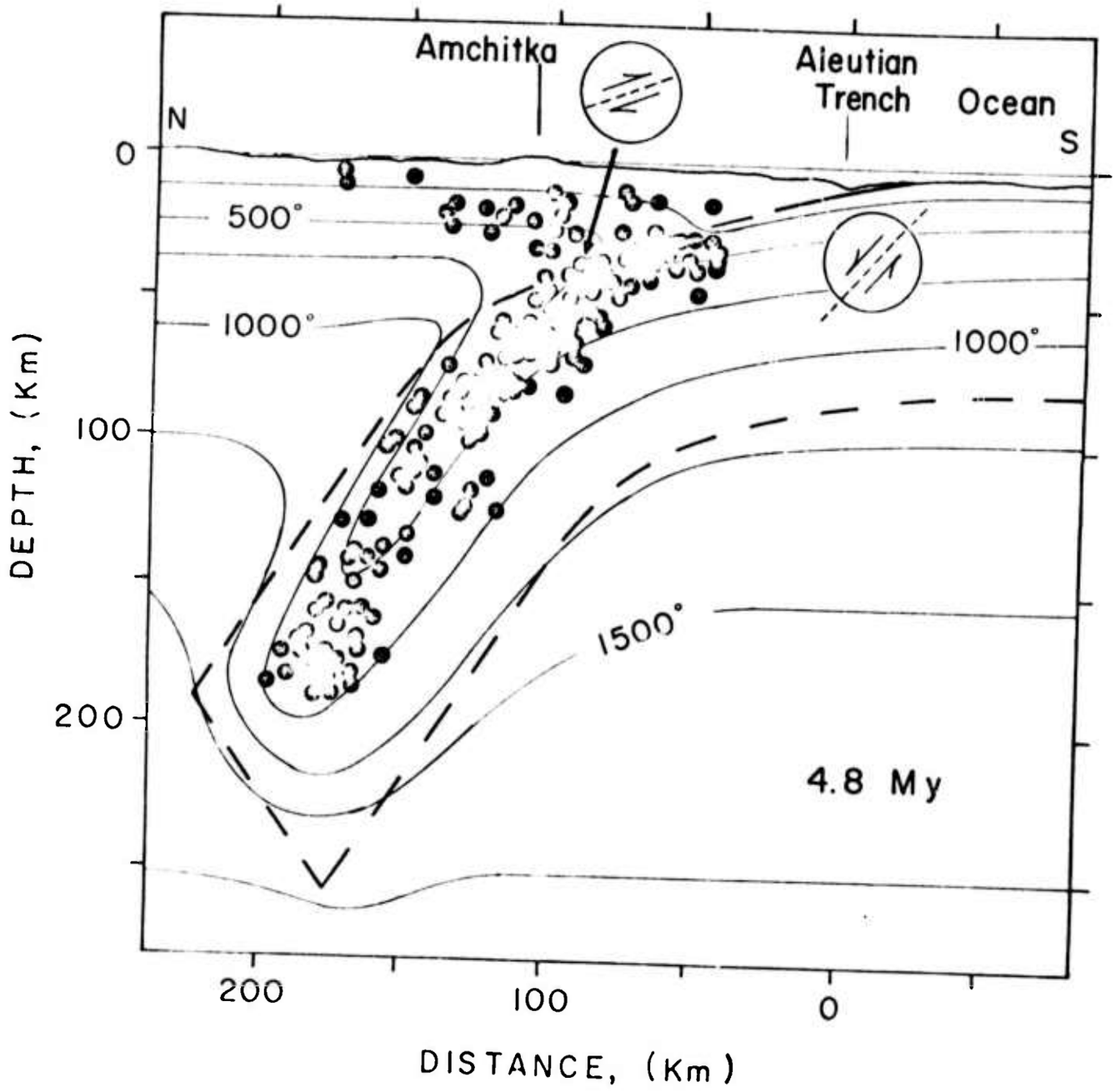
Amchitka
Aleutian
Trench
Ocean
N
S
0
500°
1000°
1000°
100
1500°
200
4.8 My
DEPTH, (Km)
200
100
0
DISTANCE, (Km)

Fig. 11

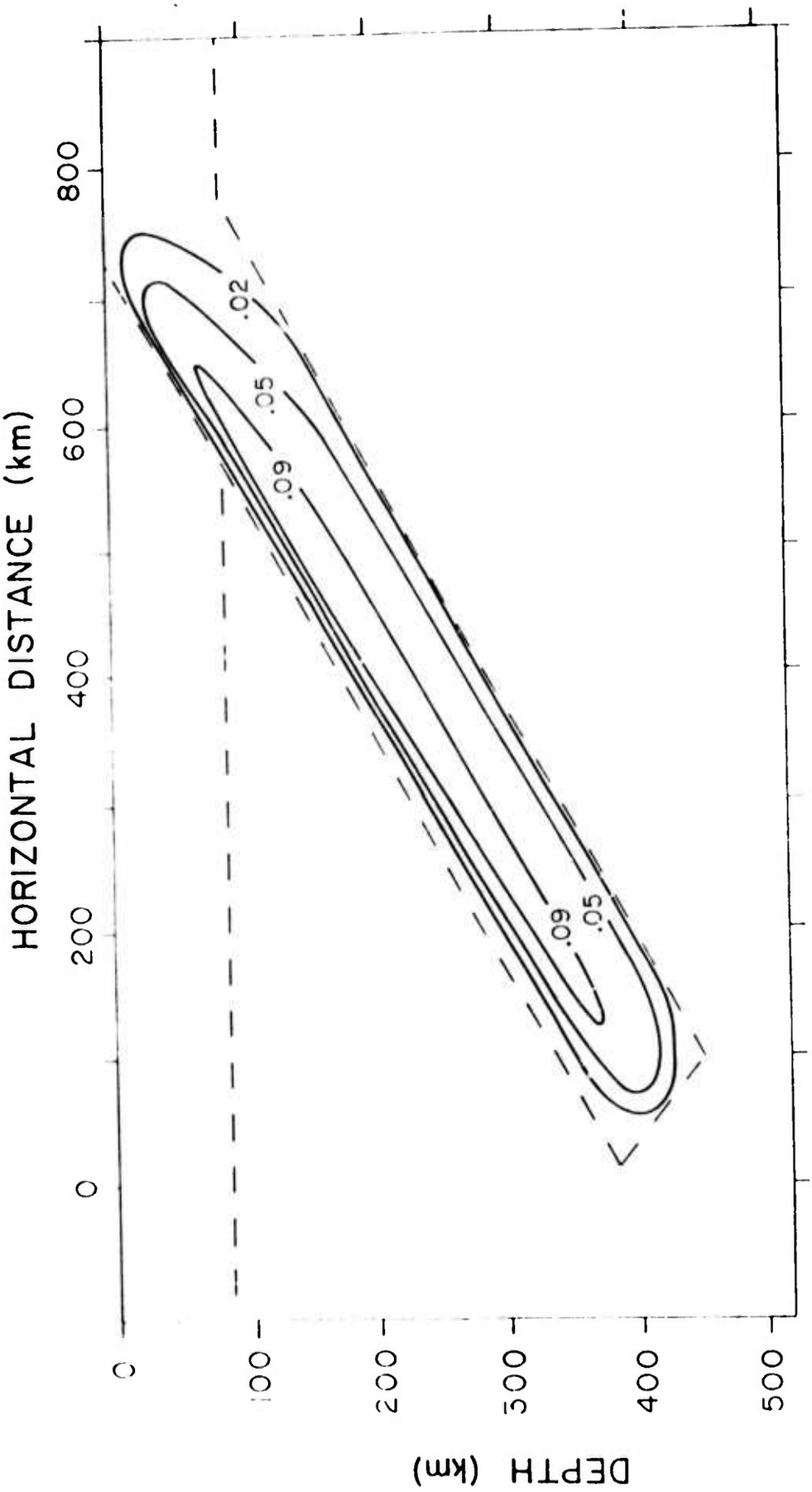
HORIZONTAL DISTANCE (km)
0
200
400
600
800
DEPTH (km)
0
100
200
300
400
500
.02
.05
.09
.09
.05

Fig. 12

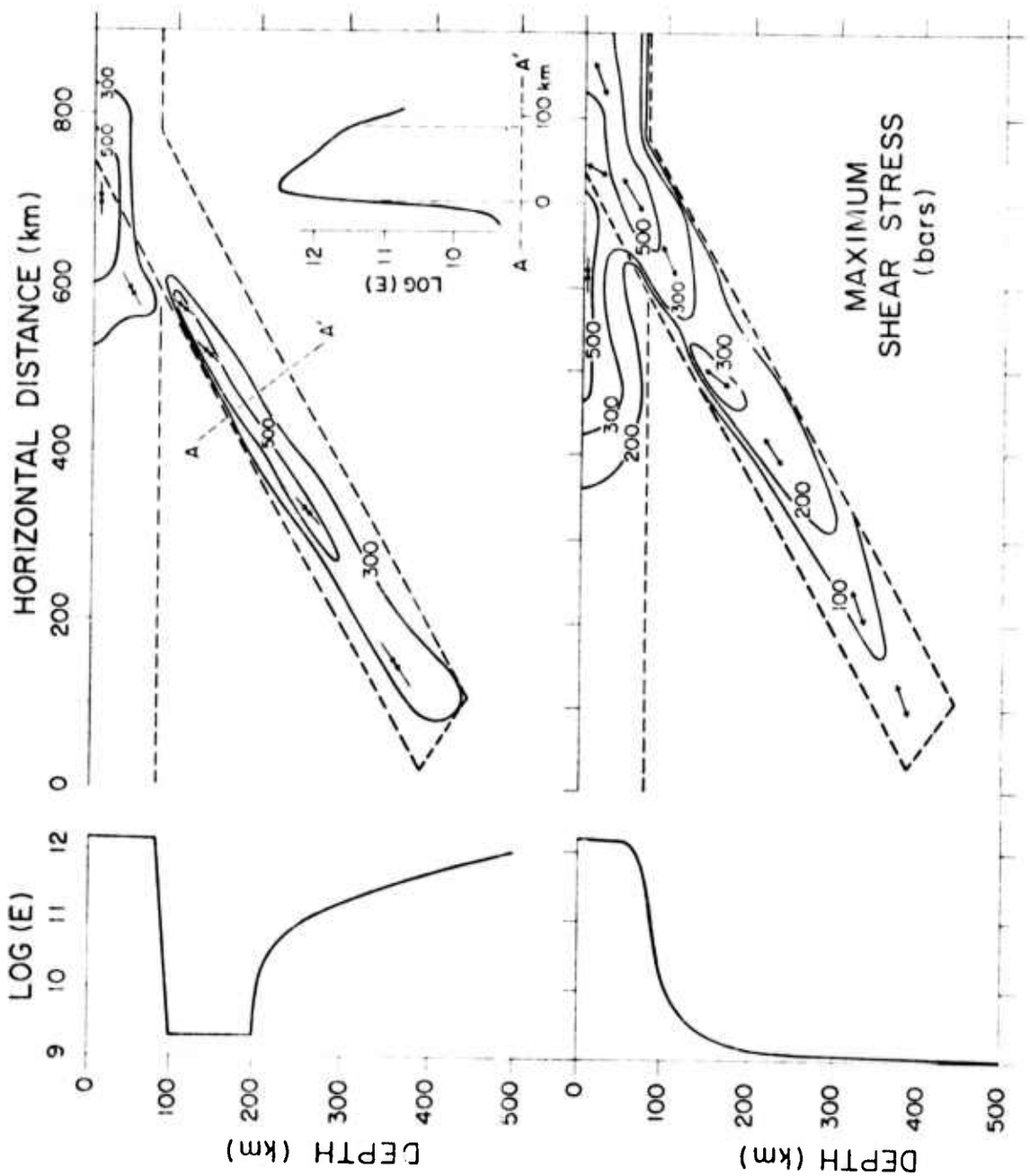
HORIZONTAL DISTANCE (km)
0
200
400
600
800
300
500
A
A'
LOG (E)
12
11
10
A
A'
100 km
0
MAXIMUM
SHEAR STRESS
(bars)
100
200
300
500
LOG (E)
9
10
11
12
DEPTH (km)
0
100
200
300
400
500

Fig. 13

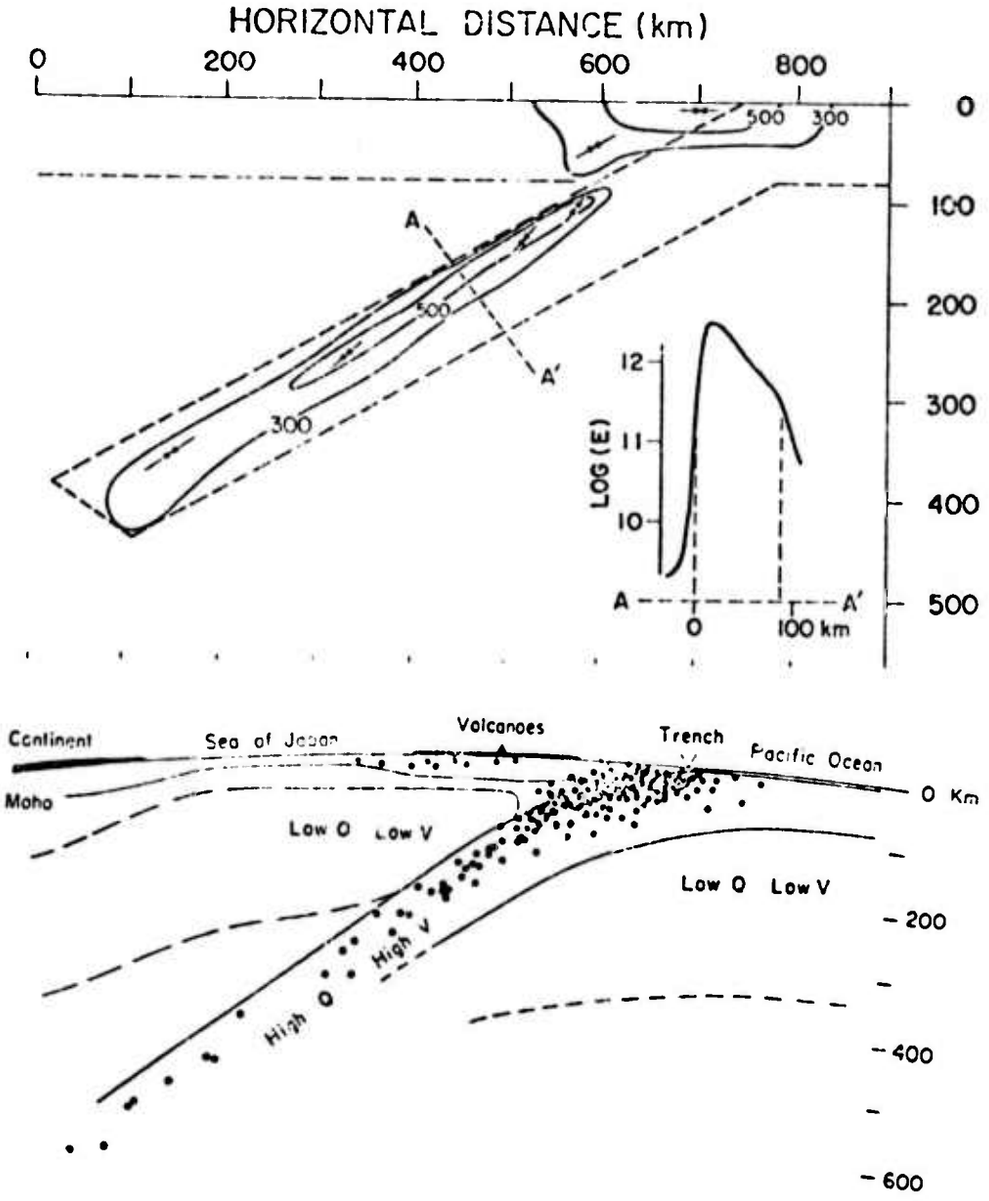
HORIZONTAL DISTANCE (km)
0
200
400
600
800
0
100
200
300
400
500
500
300
A
A'
300
LOG (E)
12
11
10
A
A'
0
100 km
Continent
Sea of Japan
Volcanoes
Trench
Pacific Ocean
Moho
0 Km
Low Q Low V
Low Q Low V
High V
High Q
200
400
600

Fig. 14

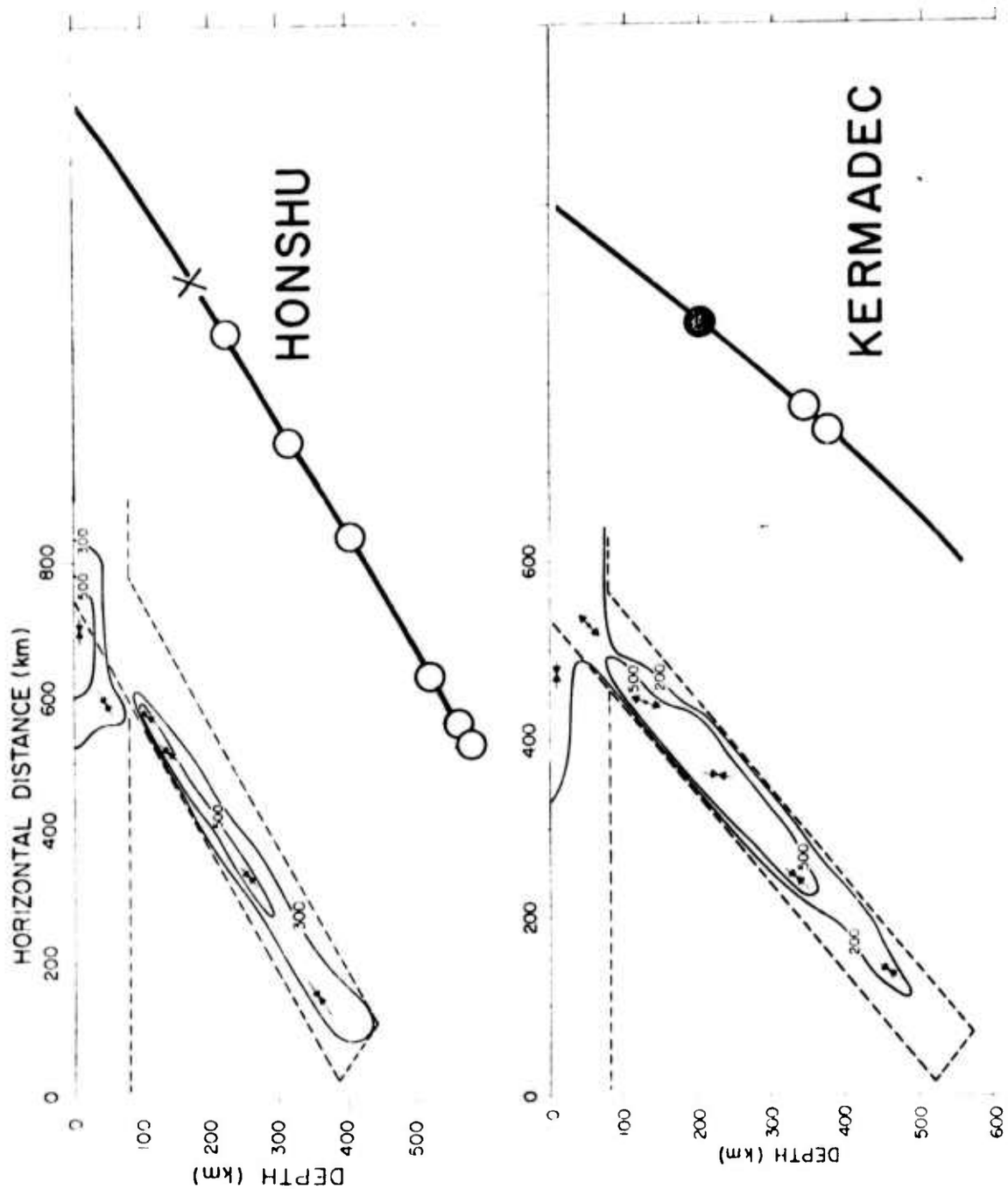
HONSHU
KERMADEC
HORIZONTAL DISTANCE (km)
DEPTH (km)
DEPTH (km)
0
200
400
600
800
100
200
300
400
500
600
300
500

Fig. 15

4. ARRAY STUDIES

4.1 Automatic Classification of Seismic Detections From Large Aperture Seismic Arrays by S. Shlien

(Abstract)

The large-aperture seismic arrays in Montana (LASA) and Norway (NORSAR) make on-line signal processing a necessity if these arrays are to be used at their full capability. Using the outputs of the detection processors of the respective arrays, the feasibility of automatic classification of seismic signals into the various body phases P, PKP, PcP, ScP, SKP, PP, PKKP and P'P' was confirmed. It was shown how these later phases can be used to advantage in improving the location capability using the combination of the two arrays.

One of the byproducts of this study was an estimation of the detection and location capabilities of the arrays. It was estimated that LASA detects more than 50 real seismic signals a day, of which less than 10% are due to later phases. LASA's detection capability extends almost one body wave magnitude below ERL's capability based on reported epicenters. The discrimination between very weak seismic signals and false alarms due to spurious noise was found difficult on the basis of only the

detection logs.

Only a little more than 8 earthquakes a day were found common between LASA and NORSAR arrays. It is expected that this number will increase with the improved signal processing that the two arrays recently implemented.

4.2 Automatic Event Detection and Location Capabilities of Large Aperture Seismic Arrays by S. Shlien and M.N. Toksöz

Summary

The detection and location capabilities of large aperture seismic arrays (LASA in Montana and NORSAR in Norway) were determined on the basis of the Detection Logs, Summary Bulletins and NOAA-ERL Preliminary Determination of Epicenters. Estimates of signal and false alarm distributions indicated that LASA can detect on the average 60 seismic signals a day and NORSAR about 20. The probability of detection of an event was estimated for LASA and NORSAR as a function of distance and magnitude.

A method of obtaining theoretical estimates of the location capability of an array as a function of beam resolution, phase type, and slowness, $dT/d\Delta$, is described. Theoretical estimates of the array's location capability compared to observed estimates imply that the arrays are operating close to their expected limits.

INTRODUCTION

The detection and location of earthquakes in real time can be accomplished with the utilization of large aperture seismic arrays. About 30 earthquakes a day are reported in the LASA Summary Bulletin on a routine basis. In this paper the present detection and location capabilities of LASA and NORSAR were estimated. Because of improvements of processing schemes, the present paper updates some earlier studies (Dean et al., 1971; Evernden, 1971; IBM Final Report, 1972).

The preparation of the Summary Bulletins can be divided into three basic steps, indicated by the block diagram in Figure 1. In the first step, the Detection Processor attempts to flag all the possible seismic signals arriving at the array of short-period seismometers. These potential signals are recorded into the Detection Log in real time together with rough estimates of the Signal to Noise Ratio (SNR), signal slowness vector, and signal intensity. In the following step, the Event Processor selects the detections with the larger SNR and then refines the estimates of signal slowness and intensity of these detections. The event epicenter, origin, and magnitude are computed from the estimates. The last step involves the editing of the output of the Event Processor into the Summary Bulletin. This step is performed by analysts who verify the output of

the Event Processor using the actual waveforms from the subarrays.

In this study both the Detection Logs and Summary Bulletins from LASA and NORSAR were used to evaluate the capabilities of the arrays. Data were available for two periods: the "summer period" from May to mid-August 1971 and the "winter period" of 20 February to 19 March 1972. The epicenter determinations published by the Environmental Research Laboratory (ERL) were used as an outside standard. Since ERL uses the LASA bulletin as a primary source in addition to other single seismic stations, ERL estimates have a small dependence on LASA measurements. Except for magnitude estimates of small earthquakes this effect may be neglected.

Heavy emphasis was placed upon the Detection Logs in the estimation of the detection capabilities of the arrays. The Detection Logs were the most complete list of possible signals observed at the arrays. A detailed description of these logs is given in the second section. The location capabilities of the arrays were determined mainly from the Summary Bulletins which contained the most accurate estimates of the signal parameters. These are discussed in the fourth section.

THE DETECTION PROCESSOR AND THE DETECTION LOG

The Detection Processor for a large aperture seismic

array was designed and developed by IBM and went into operation as of April 1969. Except for a few minor details the LASA and NORSAR Detection Processors run in a similar manner. Descriptions of the LASA and NORSAR systems are given in the IBM Final Report (1972) and in Bungum et al. (1971), respectively. Here we include a brief summary of the procedures, in order to facilitate the understanding of the later parts of the paper.

The Detection Processor accomplishes two basic operations: (1) it increases the SNR by beam forming and filtering, and (2) it decides whether a signal is present. A teleseismic signal arrives at the array approximately in the form of a plane wave with a specific slowness and azimuth, depending upon the location of the earthquake and the phase type. The noise, on the other hand, is generally diffuse and incoherent. Beam forming increases the SNR by screening out the noise from all directions and slowness except that of the actual signal, while leaving the signal approximately intact. Several hundreds of beams are generated in real time by the LASA and NORSAR Detection Processors by delaying and summing the subarray signals. Each beam is presteered towards a specific direction.

The Detection Processors deploy two sets of overlapping beams. The first partition consists of narrow beams which cover mainly the seismic regions and other areas of special interest. This partition is plotted on the world map in

Figure 2 for the P and PKP phases. The second partition consists of broader beams which cover the entire signal space.

Each of the beams is filtered and rectified by the Detection Processor. The filter was designed to deemphasize those frequency components where the SNR is low. In the case of the LASA array the signal is confined to a narrow band centered at 1 Hz. The signal at NORSAR covers a broader frequency band, between .5 and 5. Hz. The rectified beams then pass through two integrators of different time durations. These integrators compute a Short Term Average (STA) and a Long Term Average (LTA). The LTA is determined over a 28-second interval and is supposed to be a measure of the natural noise. The STA is computed for a 1.8-second time interval and is a measure of the amount of signal, if present. The LTA and STA are measured in so-called quantum units where 1 quantum unit was set at .0028 millimicrons for LASA and at .0010 millimicrons for NORSAR. The STA and LTA are updated every 0.6 and 1.8 seconds respectively. If $20 \log_{10}$ (STA/LTA) is above 8 db for at least two seconds, then the particular beam is declared to be in the detection state.

A large signal will usually trigger several beams simultaneously. The beams with the maximum STA in each of the beam partitions are recorded onto the detection log for that particular time cycle. A large seismic signal usually

has several bursts of energy so that as many as 15 beam detections could be recorded for just a P phase.

The detection log is a record of the parameters of every detection declared by the processor. The beam number, the Maximum STA (MSTA), the LTA prior to the detection state, and the start and stop times of the detection are recorded into the log in chronological order. On the average there were 450 detection entries in the LASA log and 140 detection entries in the NORSAR log per day for the period 20 February to 19 March 1972. Most of these detections occured in groups of two or more. The cumulative number of detection groups per day versus the maximum MSTA of the group is plotted for LASA and NORSAR for the winter period in the upper half of Figure 3. (A detection was defined to belong to the same group if it occurred within 30 seconds of the previous detection).

The detection groups with large MSTA were confined mostly to beams pointed towards seismically active areas. In contrast the numerous detection groups with low MSTA's occurred indiscriminately among the beams directed towards seismic and aseismic areas. This observation coupled with the fact that detections with low MSTA have a low SNR, strongly suggested that the low MSTA detections are predominantly false alarms.

Estimation of the distribution of false alarms and signals could be determined only indirectly. The top part of Figure 3 shows the cumulative distribution of detections versus the maximum MSTA of the group. For large MSTA's the SNR precludes the possibility of the detection group being a false alarm and the MSTA distribution obeys a Pareto (power law) distribution. This distribution was observed by Milne and Davenport (1969) and follows directly from Gutenberg and Richter's magnitude distributions. On account of the clipping of very large signals by the Detection Processor, the distribution departs from the power law at high MSTA. As the MSTA decreases below a certain value the number of detections starts to increase abnormally due to the inclusion of many false alarm groups. The MSTA distribution of the signals was estimated for low MSTA by extrapolating the distribution to the right of MSTA = 300 for LASA and MSTA = 2000 for NORSAR with a function of the form

$$N = A(MSTA)^{-b} \qquad (1)$$

where A and b were chosen to yield the best fit. This is indicated by the dashed line.

The false alarm distribution was determined by subtracting the presumed cumulative signal distribution from the cumulative detection group distribution. The probability of a detection being a false alarm, given MSTA, was determined

by taking the ratio of false alarm groups to detection groups in given MSTA ranges. This was plotted in the lower half of Figure 3. The false alarm probability functions obtained in this manner agreed with those determined independently using a set of aseismic beams described by Shlien (1972).

It is apparent that in order to limit false alarm occurrences the MSTA threshold must be raised above 200 for LASA and 750 for NORSAR. With MSTA = 200, as many as 50 seismic signals are detected in the case of LASA.

In the next section the detection capabilities of LASA and NORSAR are estimated as a function of magnitude and distance of the event.

DETECTION CAPABILITIES OF LASA AND NORSAR

The detection capabilities of seismic instruments are limited primarily by microseismic noise. The noise level is considerably larger at NORSAR in the signal band on account of its proximity to the coast (IBM Final Technical Report, 1971; Felix et al., 1972). A large aperture seismic array allows one to enhance the SNR by appropriate beam forming. If the noise is uncorrelated and the signal is coherent between the sensors, the maximum SNR gain achievable with an array goes

as $\sqrt{N}$ where N is the total number of sensors.

For two reasons neither LASA nor NORSAR can attain this optimum gain. First, the signal amplitude and shape vary by almost an order of magnitude across the array. This is believed to be caused by path differences between source and sensors and by the multipathing and scattering of the signal underneath the array (Mack, 1969; Larner, 1970). The signal variations are consistent with events from the same location but change unpredictably when the epicenter is shifted by a few degrees. Finally, the seismic signal arrives as a distorted plane wave due to local and deep lateral heterogeneities (Greenfield and Sheppard, 1969; Davies and Sheppard, 1972). Unless special velocity-dependent station corrections were incorporated into the beam forming process severe signal losses would be sustained. Both LASA and NORSAR had an improved set of station corrections since February 1972. As a result there has been a slight improvement in the detection and location capabilities of LASA and NORSAR since that time.

Using the ERL preliminary epicenter determinations

as a standard we estimated the capabilities of LASA and NORSAR by counting the number of matches that could be made with the detection log. The arrival time of the P or PKP phase was calculated at either array using the ERL catalog and travel time tables. The signal was taken to be detected by the array if it could be matched to a detection in the log within ±10 seconds of the expected arrival time. Periods when the Detection Processor was down were taken into account in the analysis.

To reduce the probability of a spurious match with a signal or false alarm, detections below MSTA = 250 for LASA and MSTA = 1000 for NORSAR were disregarded. With this rule it was estimated that the probability of making a false match was about 1 percent for either array. In Figure 4 the percentage of ERL events detected per 10 degree distance intervals are plotted for LASA and NORSAR. Data for the 20 February to 19 March 1972 period are indicated by the dashed lines. Both arrays had made slight improvement in their detection capabilities. Most of the improvement is due to the incorporation of more accurate station corrections into the systems before the winter period data were taken.

The detection capabilities of the arrays are consistently inferior for local events and distant events

in the vicinity of the shadow zone (100-110 degrees). Local events are difficult to detect by the present processors for the following three reasons. (1) The signal is emergent and spread out, (2) the wavefront is too spherical and cannot be approximated by a plane wave, and (3) the $dT/d\Delta$ varies so rapidly with distance in this range that a prohibitive number of beams would be needed. LASA has no beams in the near zone. Beyond 90 degrees the P wave becomes diffracted and highly attenuated by the core-mantle boundary. Low magnitude earthquakes are easily missed. In the diffraction zone the $dT/d\Delta$ versus Δ curve becomes nearly constant. Hence it is very difficult to locate earthquakes from this zone. The LASA Summary Bulletin does not attempt to report any events beyond 100 degrees. NORSAR appears to miss an unusual number of events coming from the Aleutians and the western part of the United States. This is evidenced by the dip in the detection capability beyond 60 degrees.

In Figure 5 the detection capabilities of LASA and NORSAR are shown as a function of magnitude. The percents of ERL events detected between 0 and 80 degrees (upper half) and between 80 and 180 degrees (lower half) distance from the array in question were plotted versus magnitude units. Newer data from the winter period (1972) are distinguished by the dashed lines. Due to the rapidly decreasing sample

sizes at the higher magnitudes, the percent of events detected sometimes decreases with increasing magnitude. LASA detects almost all ERL events greater than magnitude 4.5 and less than 80 degrees. Considerable improvement in both NORSAR's and LASA's detection capability after February 1972 is evident in the lower plots.

It is evident that NORSAR's detection capability is overall inferior to LASA's. Unlike LASA, a considerable amount of the signal energy in NORSAR is concentrated at high frequencies (Harley, 1972). However, since the noise is also higher in the high frequency band at NORSAR the problem of discriminating the signal from noise is more acute. In addition, the effect of inaccurate station corrections is worse for high frequency signals.

The analysis so far has shown that LASA can detect over 90 percent of the reported (ERL) events in the distance range of 30 to 80 degrees and that NORSAR likewise can detect close to 60 percent of the ERL events. It is not apparent so far how many additional events the arrays detect that are not on the ERL list. To make this determination we resorted to the Summary Bulletins generated by LASA and NORSAR.

In Figure 6 the frequency-magnitude distribution of events reported in the Summary Bulletins are plotted with the ERL frequency-magnitude distribution. Events further than 95 degrees of the array in question were not included in either distribution. It is seen that LASA reports many more low magnitude events than ERL. The peak of the LASA distribution m_b = 3.7 is one magnitude unit to the left of the ERL distribution. NORSAR apparently reports slightly more low magnitude events than ERL and the peak lies 0.5 magnitude units to the left of ERL's mode.

The leftward shift of the frequency-magnitude distribution can also be partially attributed to a bias in the magnitude estimates. Correlation plots of LASA and NORSAR's magnitudes versus ERL magnitude are shown in Figure 7. They suggest that part of the shift in the distributions can be explained by small magnitude-dependent biases.

These results have demonstrated that LASA and NORSAR have detection capabilities comparable to ERL at least for earthquakes in the range of 30 to 80 degrees distance. Similar results have been disclosed by the IBM Final Technical Report (1971) and by Dean et al. (1971). On the other hand the location capability of an array would not be as accurate as that obtained with a network of seismometers due to its

finite aperture. Epicenter locations accurate to a tenth of a degree can be achieved with seismic stations suitably spaced around the earthquake's focus as was shown by Evernden (1971).

In the next section a theoretical analysis of the location capability of the arrays was carried out and the actual performance of arrays in locating events is described.

LOCATION CAPABILITY OF LASA AND NORSAR

With a large aperture seismic array one can determine the direction and velocity of the arriving signal. This permits an estimate of the event's epicenter. Studies on the location capabilities of seismic networks and arrays have been performed by Evernden (1971) and Gjoystdal et al., (1972).

For the P phase there is a single valued transformation between the signal's inverse phase velocity (slowness) vector and the epicenter's location. The distance, Δ, of the event depends only on the magnitude of the slowness,

$dT/d\Delta$, and the azimuth of the event is the same as that of the signal.

Due to the limited resolution of the array there is always an uncertainty σ in the determination of the slowness. The size of this uncertainty is proportional to T/A where T is the period of the signal and A is the aperture of the array. The associated error in the event's location is dependent upon its distance from the array on account of the nonlinear transformations involved.

Distance is determined from $dT/d\Delta$ using an empirical transformation $\Delta = \Delta(dT/d\Delta)$ based on the present models of the earth. Since each phase type has its own transformation it is important to have the signal properly classified at this point. Supposing the measured inverse phase velocity is $(dT/d\Delta)_o$ with uncertainty σ, then the uncertainty in the corresponding distance is given by

$$\delta\Delta = \Delta[(dT/d\Delta)_o + \sigma/2] - \Delta[(dT/d\Delta)_o - \sigma/2] \qquad (2)$$

If σ is sufficiently small, then this can be approximated by

$$\delta\Delta = \left(\frac{\sigma d\Delta(dT/d\Delta)}{d(dT/d\Delta)_o}\right) = \frac{\sigma}{\left(\frac{d^2T}{d\Delta^2}\right)_o} \qquad (3)$$

In Figure 8, $dT/d\Delta$ and $d^2T/d\Delta^2$ curves are plotted versus Δ after Herrin et al. (1968) for the P phase. Around 90 degrees $d^2T/d\Delta^2$ approaches zero rapidly, resulting in very poor distance determinations. This effect is apparent in Figure 9, where the distance and azimuth of all earthquakes triggering specific beams in the LASA high resolution beam partitions over a certain time period are plotted. Though the beams have identical resolution in inverse velocity space, it is very clear that closer to the shadow zone the region of epicenters that can trigger the same beam becomes broader. The areas represented in the figure (Aleutians, Japan, and Tonga) are extensive seismic regions.

The azimuth resolving power of an array is also dependent upon $dT/d\Delta$. If $dT/d\Delta$ is small in comparison to σ, the zone of uncertainty of the slowness vector is centered close to the origin and the uncertainty in azimuth is large. This corresponds to a seismic signal coming nearly vertical.

In order to estimate analytically the error in azimuth it was assumed that the error in the slowness vector $dT/d\Delta$ determination is normally distributed with zero mean and standard deviation σ. Let u be the magnitude and α

the azimuth of the actual slowness vector, and let ν be the measured magnitude and β the measured azimuth. Then by assumption the probability of measuring ν and β given that the actual values are u and α is

$$p(\nu,\beta|u,\alpha) = \frac{\nu}{2\pi\sigma^2} \exp\left(-[\nu^2+u^2-2\nu u \cos(\alpha-\beta)]/2\sigma^2\right) \quad (4)$$

$$0 \leq \nu \leq \infty$$

$$0 \leq \alpha \leq 2\pi$$

(This is the same model for the radar problem of narrow band signal with additive normal noise.)

Then

$$p(\beta|u,\alpha) = \int p(\nu,\beta|u,\alpha)\,d\nu \quad (5)$$

$$= \frac{1}{2\pi} \exp(-a_o^2)\ [1 + 2\sqrt{\pi}a_o\cos\gamma \frac{1+\mathrm{erf}(a_o\cos\gamma)}{2} \exp(a_o^2\cos^2\gamma)]$$

where $a_o^2 = u^2/2\sigma^2$ and $\gamma = \beta-\alpha$ (Schwartz, 1970). For large a_o^2, the curve may be approximated by a Gaussian distribution with mean α and variance $(2a_o^2)^{-1}$. The standard error of β is plotted versus a_o in Figure 10. (The standard error was determined numerically for small a_o.)

As an example, the theoretical resolution of LASA over a frequency band 1.0 - 2.0 Hz is about $\sigma = 0.2$ seconds/degree (IBM Final Report, 1972). This corresponds to an error of distance of $\delta\Delta = 2.5$ degrees in the distance range of 40 to 85 degrees and an error of $\delta\Delta = 20$ degrees in the shadow zone. Clearly, azimuth error is much smaller than distance error. Azimuth errors do not become appreciable except for phases with small $dT/d\Delta$ such as PKP (DF branch), P'P' (DF branch) and PKKP (BC branch).

This analysis had not considered the effect of station residual, which can introduce large biases in the estimation of $dT/d\Delta$. Nor are the effects of lateral velocity variations included in the figures. For this reason these theoretical results should be regarded as lower bounds on the location uncertainty to be attained with accurate station corrections.

In Figure 11 the distribution of distance and azimuth errors is plotted for LASA and NORSAR. All earthquakes in the Summary Bulletin that could be matched with ERL epicenter determinations for the specific time periods were represented in the distribution. Events with large distance and azimuth errors were generally associated with events in the shadow zone. Biases in distance and azimuth determinations were apparently negligible implying that station residual effects have been properly compensated for in the

Event Processor. The magnitude of these location errors also indicates that the arrays are fairly close to their theoretical resolution limit.

DISCUSSION AND CONCLUSIONS

In this study, the capabilities of LASA and NORSAR were evaluated on the basis of their present signal processors. The effectiveness of this analysis was limited by several factors. First, since the study was restricted to data that had been partially reduced by the Detection Processor, the Event Processor and the analyst, the tendency would be to underestimate the ultimate capabilities of the arrays. For instance, faulty station corrections incorporated into the Detection Processor for the May through August 1971 period deteriorated its performance. Second, there was a lack of a firm and large standard data base from which to evaluate the full capabilities of LASA and NORSAR. The only set of known earthquakes available at the time of the study was the Environmental Research Laboratory (ERL) list of epicenter determinations. This list omitted many low magnitude events which LASA and NORSAR were capable of observing. Finally, major modifications of the signal

processing system to improve its performance and to remove recently discovered errors made uniform data over a long time span unavailable.

Notwithstanding these factors, it has been made apparent that excellent detection capability can be achieved by these arrays, LASA in particular. The location capabilities of the arrays, although not as good as those of a network of seismometers adequately spaced around the epicenter, are close to their theoretical capability.

The determination of hypocenter depth by a single array has not been successful due to the problem of recognizing and distinguishing the depth phases pP and sP consistently. For this reason depth determinations were not included in this study.

The main conclusions of the study are listed below.

1. LASA detects over 90 percent of the events reported by ERL in the distance range 30 to 80 degrees. NORSAR detects about 60 percent of the reported ERL epicenter determinations in the same distance range.
2. LASA's detection capability is at least 0.5 magnitude lower than ERL's capability on the basis of the frequency magnitude distributions of the LASA Summary Bulletin and ERL epicenter determinations.

(ERL reports only the events that it can locate within a specified accuracy. There are many more events that they detect but do not list in their bulletin.) NORSAR's detection capability is just slightly better than ERL's.

3. By extrapolation of the Maximum Short Term Average (MSTA) of detection group distribution of signals to low MSTA's it was estimated that as many as 120 seismic signals a day were detected by LASA and 35 by NORSAR. The problem of distinguishing signals from false alarms limits the number of seismic events that can be reported to those with high signal-to-noise ratios.
4. LASA and NORSAR are able to locate events to within 3 degrees. Errors in azimuth determinations are smaller than errors in distance determination, which is in agreement with the theoretical model presented. It appears that both arrays are locating events at nearly their resolution limit, imposed by the aperture of the arrays.
5. NORSAR underestimates the magnitude of an earthquake by one half a unit relative to ERL. LASA's magnitude bias is negligible and magnitude dependent.

ACKNOWLEDGMENTS

We would like to thank Dr. J. Capon, Dr. R. Lacoss and Mr. R. Sheppard of Lincoln Laboratory for their comments and suggestions at various stages in the preparation of the manuscript. Dr. Lacoss' continued support has helped lead this work. Also, we would like to thank Dr. C. Felix, Mr. S. Sarmiento (IBM), Dr. W. Dean, Mr. G. Moore (Geotech-Teledyne), and Dr. E. Husebye (NORSAR) who assisted us in obtaining the Detection Logs and Summary Bulletins. Critical comments from Dr. R.O. Ahner, Dr. W. Dean, Dr. J. Evernden, and Dr. T.W. Harley were invaluable in the preparation of the paper.

S. Shlien was supported by a Chevron Oil Research Fellowship from 1971-1972, during part of the time of this study. This project was supported by the Advanced Research Projects Agency monitored by the Air Force Office of Scientific Research under contract no. F44620-71-C-0049 and contract no. AF49(638)-1763.

REFERENCES

Bungum, H., E.S. Husebye, and F. Ringdal (1971). The NORSAR array and preliminary result of data analysis. Geophys. J. Roy. Astron. Soc. 25, 115-126.

Davies, D., and R.M. Sheppard (1972). Lateral heterogeneity in the earth's mantle. Nature 239, 318-323.

Dean, W.C., R.O. Ahner, and E.F. Chiburis (1971). SAAC Evaluation of the SAAC/LASA System. Teledyne-Geotech technical report under contract no. F33657-71-C-0510.

Evernden, J.F. (1971). Location capabilities of various seismic networks. Bull. Seism. Soc. Am. 61, 241-273.

Felix, C.P., W.L. Gilbert, and S.G. Wheeler (1972). Preliminary results from NORSAR short period system. Proceedings from the Seminar on Seismology and Seismic Arrays, 1971, Oslo (ed. Husebye, E.S. and H. Bungum), 143-163.

Gjoystdal, H., E.S. Husebye, and D. Rieber-Mohn (1972). Simulating array event location capabilities. Proceedings from the Seminar on Seismology and Seismic Arrays, 1971, Oslo (ed. Husebye, E.S. and H. Bungum), 271-280.

Greenfield, R.J., and R.M. Sheppard (1969). The Moho depth variations under the LASA and their effect on $dT/d\Delta$ measurements. Bull. Seism. Soc. Am. 59, 409-420.

Harley, T.W. (1972). Preliminary evaluation of the NORSAR short period and long period arrays. Proceedings from the Seminar on Seismology and Seismic Arrays, 1971, Oslo (ed. Husebye, E.S. and H. Bungum), 165-192.

Herrin, E., et al. (1968). Seismological tables for P phases. Bull. Seism. Soc. Am. 58, 1193-1241.

IBM Final Technical Report (1971). Integrated Seismic Research Signal Processing System. ESD-TR-72-139 under Contract No. F19628-68-C-0400.

IBM Final Report (1972). Large-Aperture Seismic Array Signal Processing Study. Prepared for Advanced Research Projects Agency, Contract No. SD-296.

Larner, K.L. (1970). Near-receiver scattering of teleseismic body waves in layered crust-mantle models having irregular interfaces, Ph.D. Thesis, Massachusetts Institute of Technology.

Mack, H. (1969). Nature of short period P-wave signal variations at LASA. J. Geophys. Res. 74, 3161-3170.

Milne, W.G. and A.G. Davenport (1969). Distribution of earthquake risk in Canada. Bull. Seism. Soc. Am. 59, 729-754.

Schwartz, M. (1970). Information Transmission, Modulation and Noise. McGraw-Hill.

Shlien, S. (1972). Automatic classification of seismic detections from large aperture seismic arrays. Ph.D. Thesis, Massachusetts Institute of Technology.

FIGURE CAPTIONS

Fig. 1. Upper: block diagram of the LASA signal processor. Lower: block diagram of the LASA Detection Processor.

Fig. 2. P and PKP phase locations of LASA beams (high resolution partition) as given by the Seismic Array Analysis Center and plotted on an equidistant projection centered at LASA.

Fig. 3. Upper: cumulative distribution of the number of detection groups (dots) and inferred number of signal groups (dashed curve) versus MSTA for LASA (left) and NORSAR (right), determined for the winter period 1972. Lower: estimated false alarm probability given MSTA for LASA(left) and NORSAR (right). Magnitude given for earthquake at a distance of 60°

Fig. 4. Percentage of ERL events detected in 10 degree intervals of distance for LASA (left) and NORSAR (right). Dots and solid lines denote summer 1971 period; X's and dashed lines denote winter 1972 period.

Fig. 5. Percentage of ERL events detected in half magnitude units for LASA (left) and NORSAR (right). Upper

plots include only events less than 80 degrees distance from the respective array. Lower plots contain the events further than 80 degrees. Solid line - summer 1971, dashed line - winter 1972.

Fig. 6. Frequency magnitude distribution of earthquakes less than 95 degrees from their respective arrays determined from LASA and NORSAR Summary Bulletins and the ERL epicenter determinations. LASA's distribution was determined for summer 1971 and NORSAR's distribution for winter 1972.

Fig. 7. Correlation plots of LASA magnitude versus ERL magnitude (summer 1971) and NORSAR magnitude versus ERL magnitude (winter 1972).

Fig. 8. $dT/d\Delta$ and $d^2T/d\Delta^2$ versus Δ for P phase.

Fig. 9. Distance and azimuth of epicenter triggering specific LASA high resolution beams assuming P phase.

Fig. 10. Standard error in azimuth versus a_o.

Figl 11. Histogram of distance and azimuth location errors determined for LASA (left - summer 1971) and NORSAR (right - winter 1972).

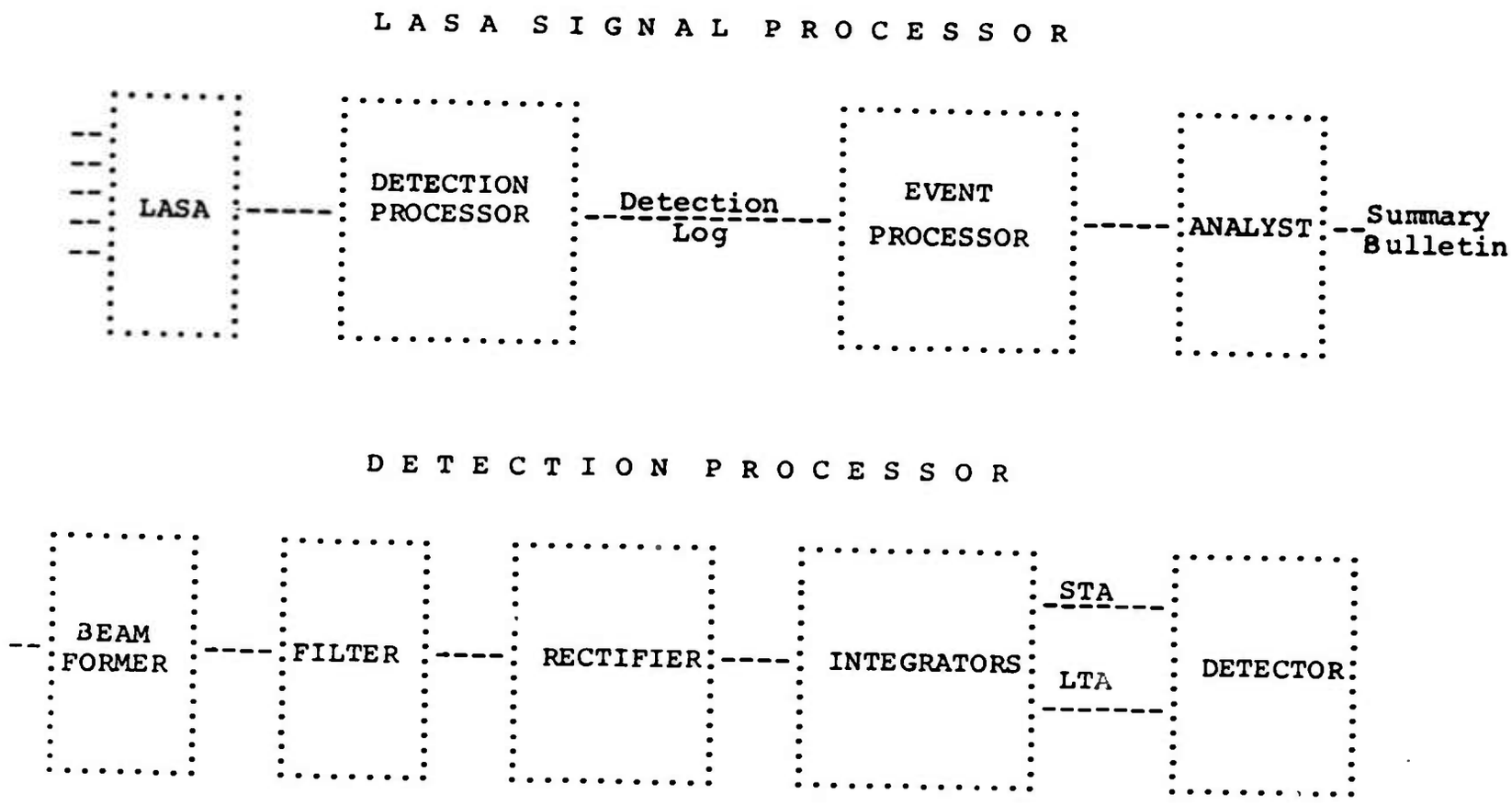
LASA SIGNAL PROCESSOR
LASA
DETECTION PROCESSOR
Detection Log
EVENT PROCESSOR
ANALYST
Summary Bulletin
DETECTION PROCESSOR
BEAM FORMER
FILTER
RECTIFIER
INTEGRATORS
STA
LTA
DETECTOR

Figure 1

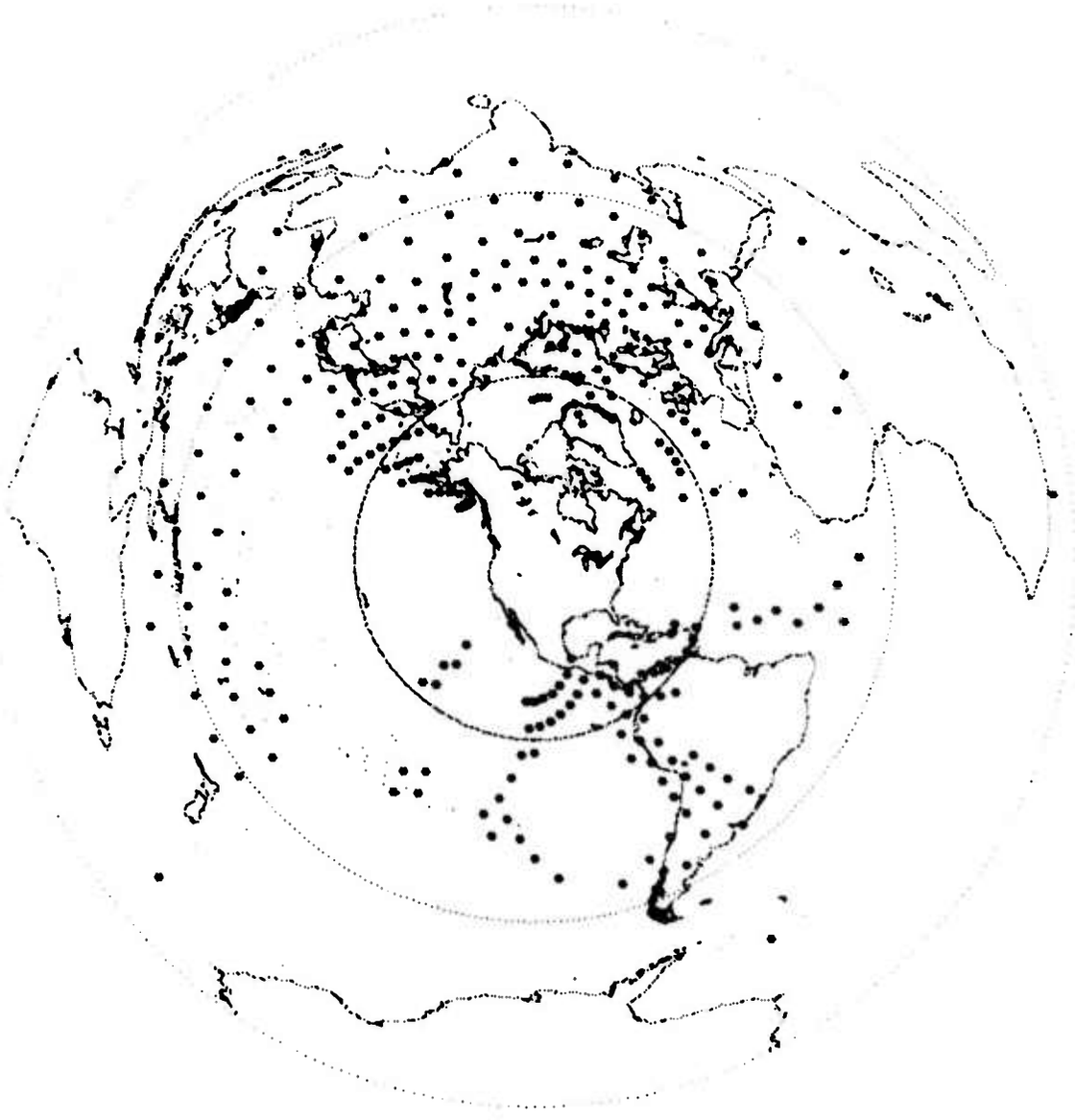

Figure 2

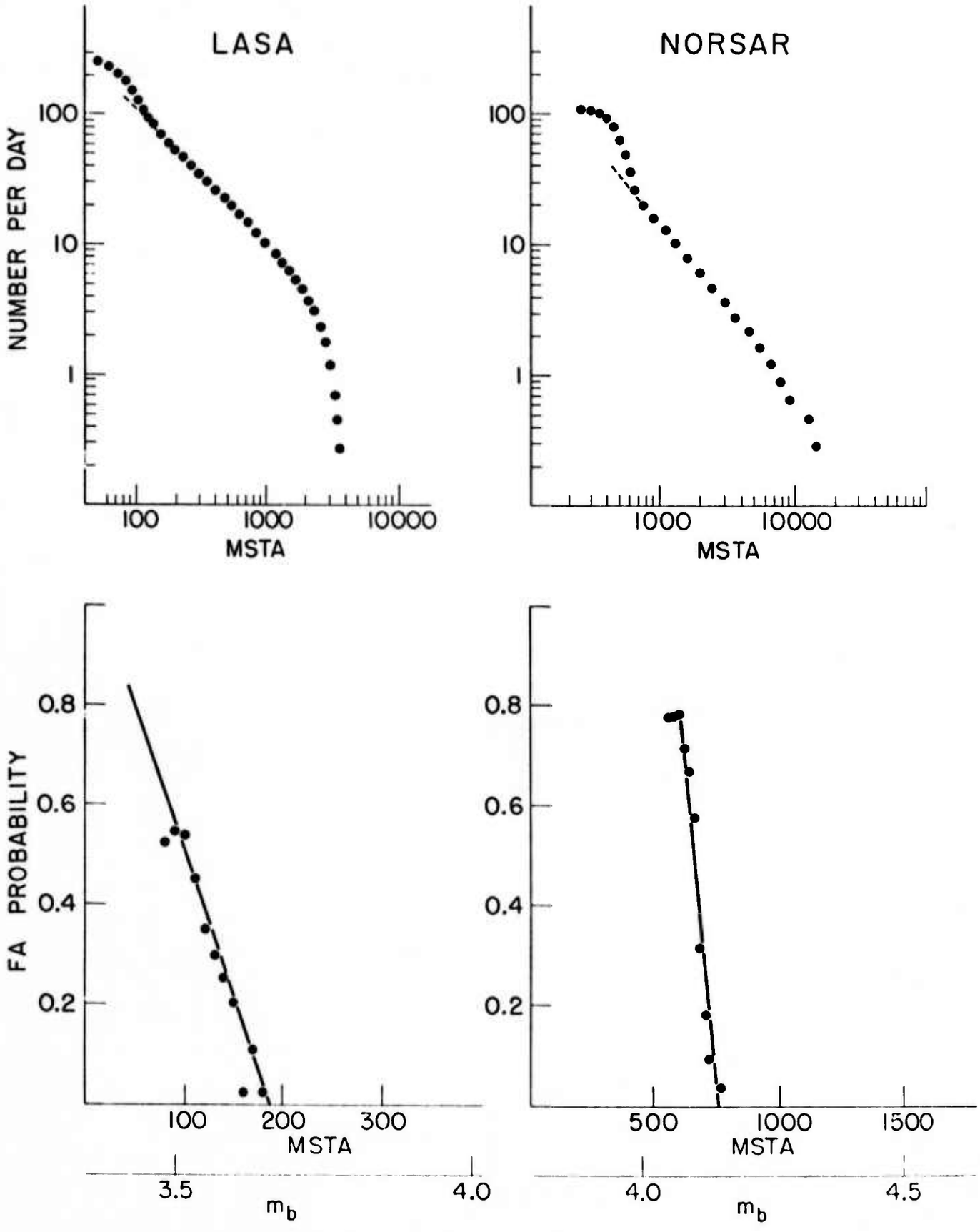
LASA
NORSAR
NUMBER PER DAY
100
10
1
100
1000
10000
MSTA
1000
10000
MSTA
FA PROBABILITY
0.8
0.6
0.4
0.2
100
200
300
MSTA
3.5
4.0
m_b
500
1000
1500
MSTA
4.0
4.5
m_b

Figure 3

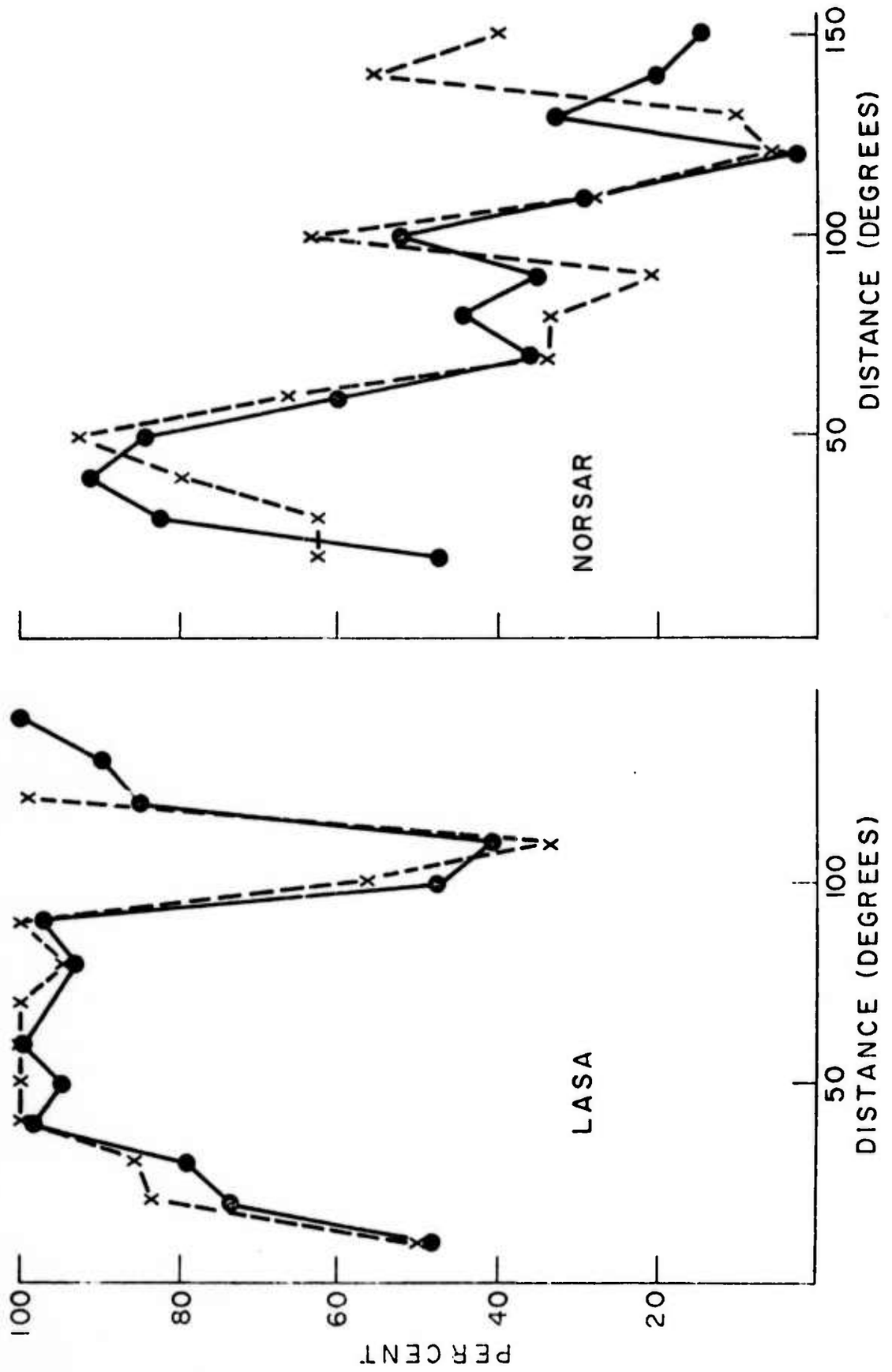
PERCENT
100
80
60
40
20
LASA
50
100
DISTANCE (DEGREES)
NORSAR
50
100
150
DISTANCE (DEGREES)

Figure 4

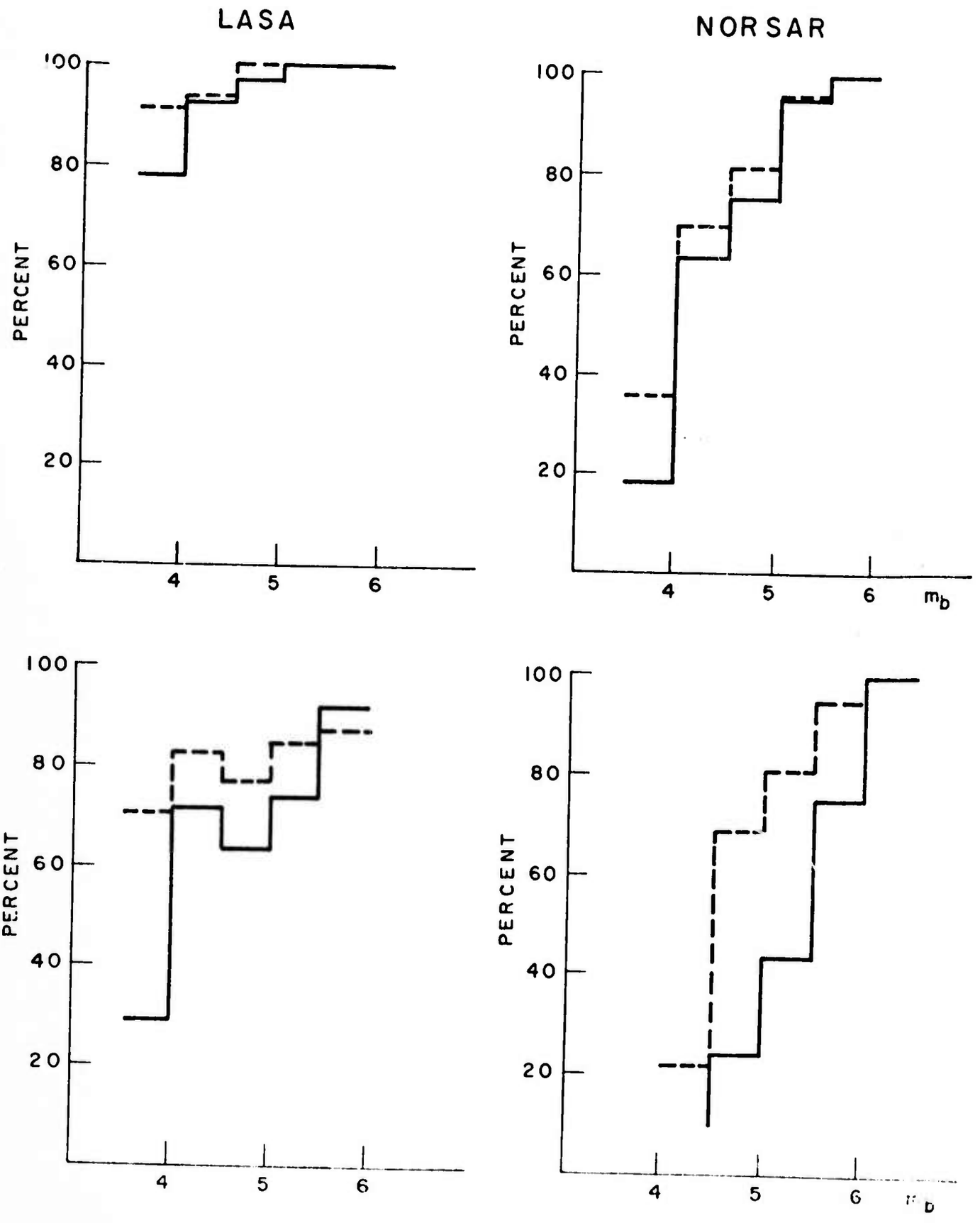

Figure 5

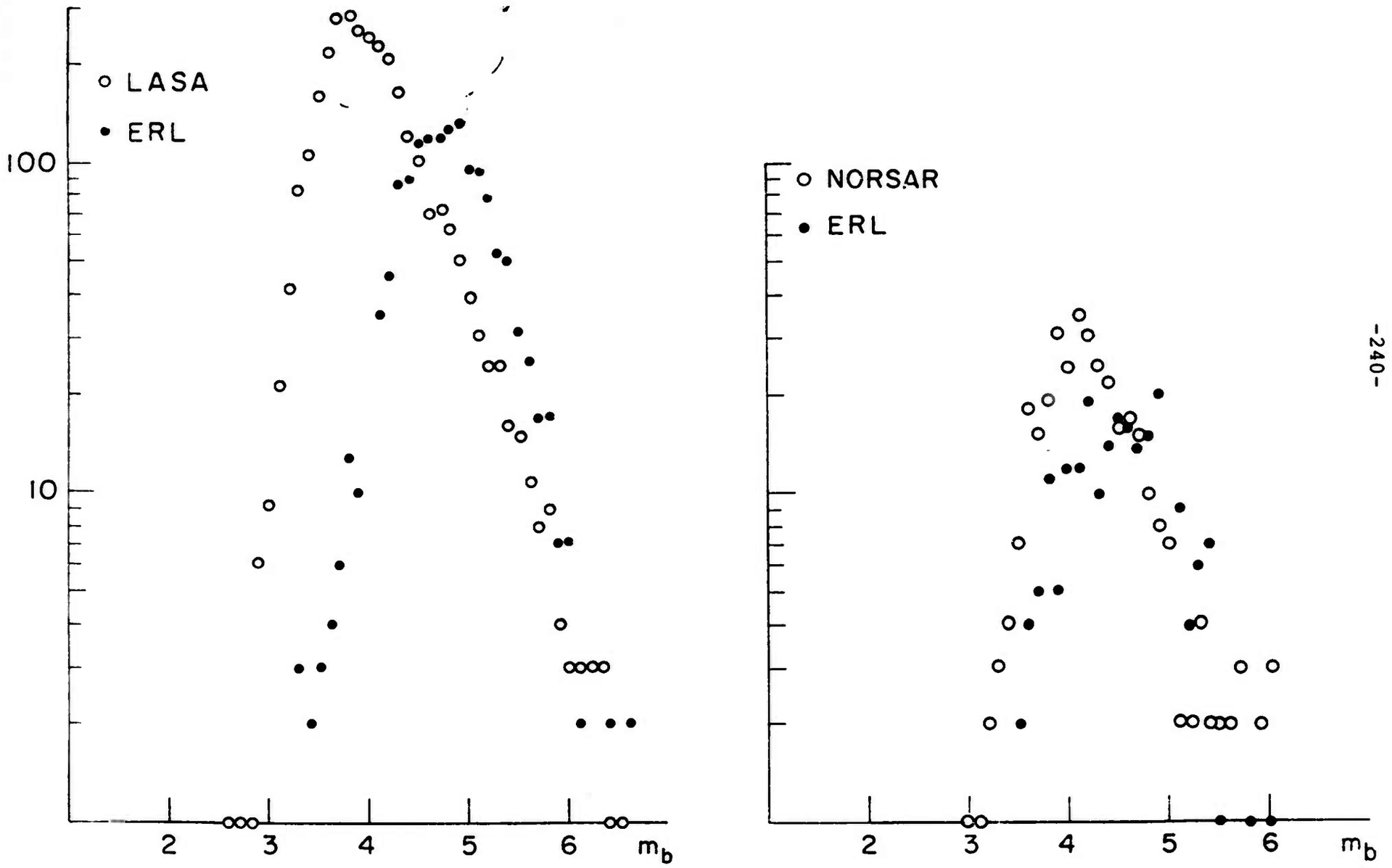
FREQUENCY - MAGNITUDE
LASA
ERL
100
10
2
3
4
5
6
m_b
NORSAR
ERL
2
3
4
5
6
m_b

Figure 6

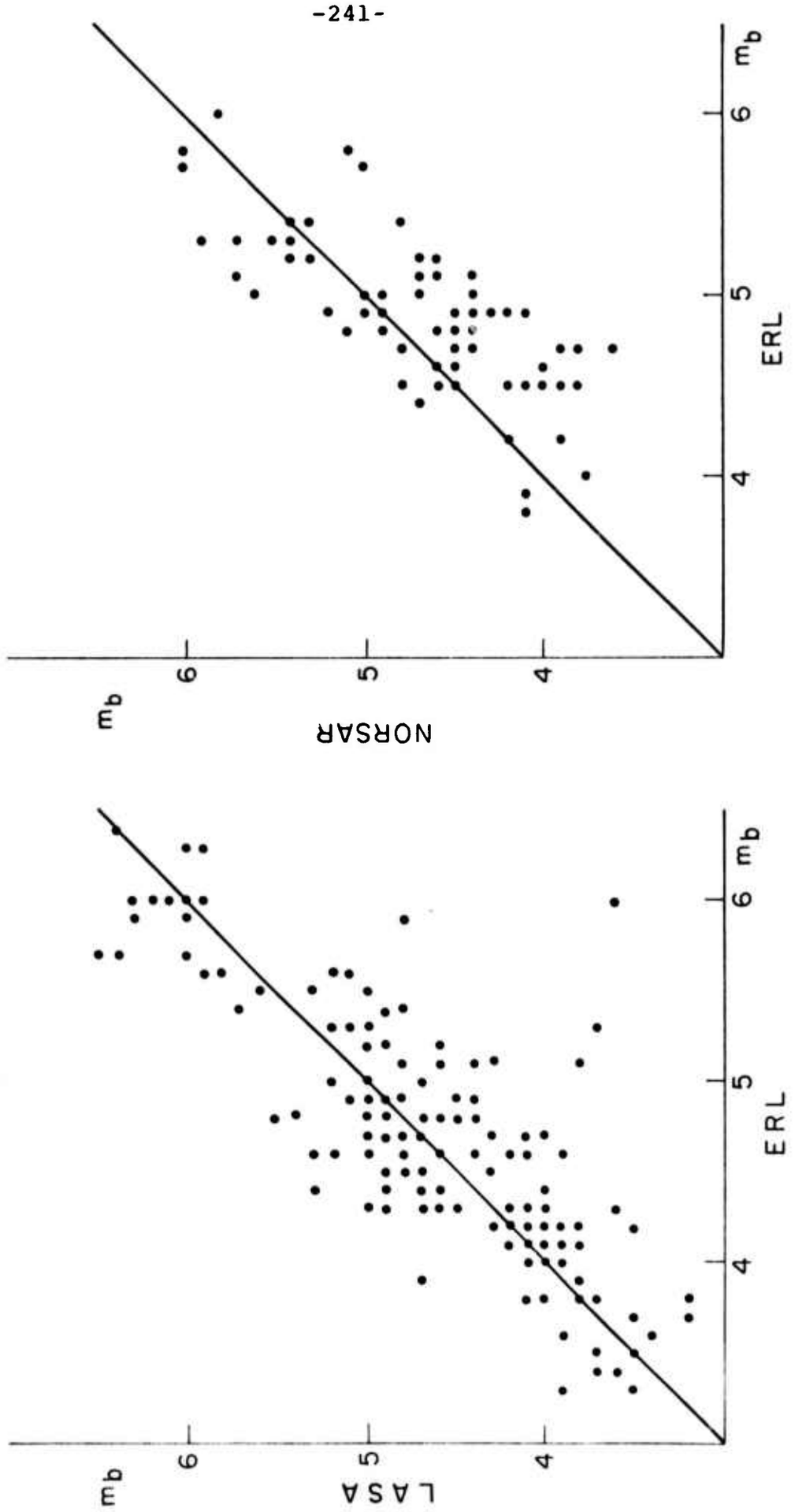

Figure 7

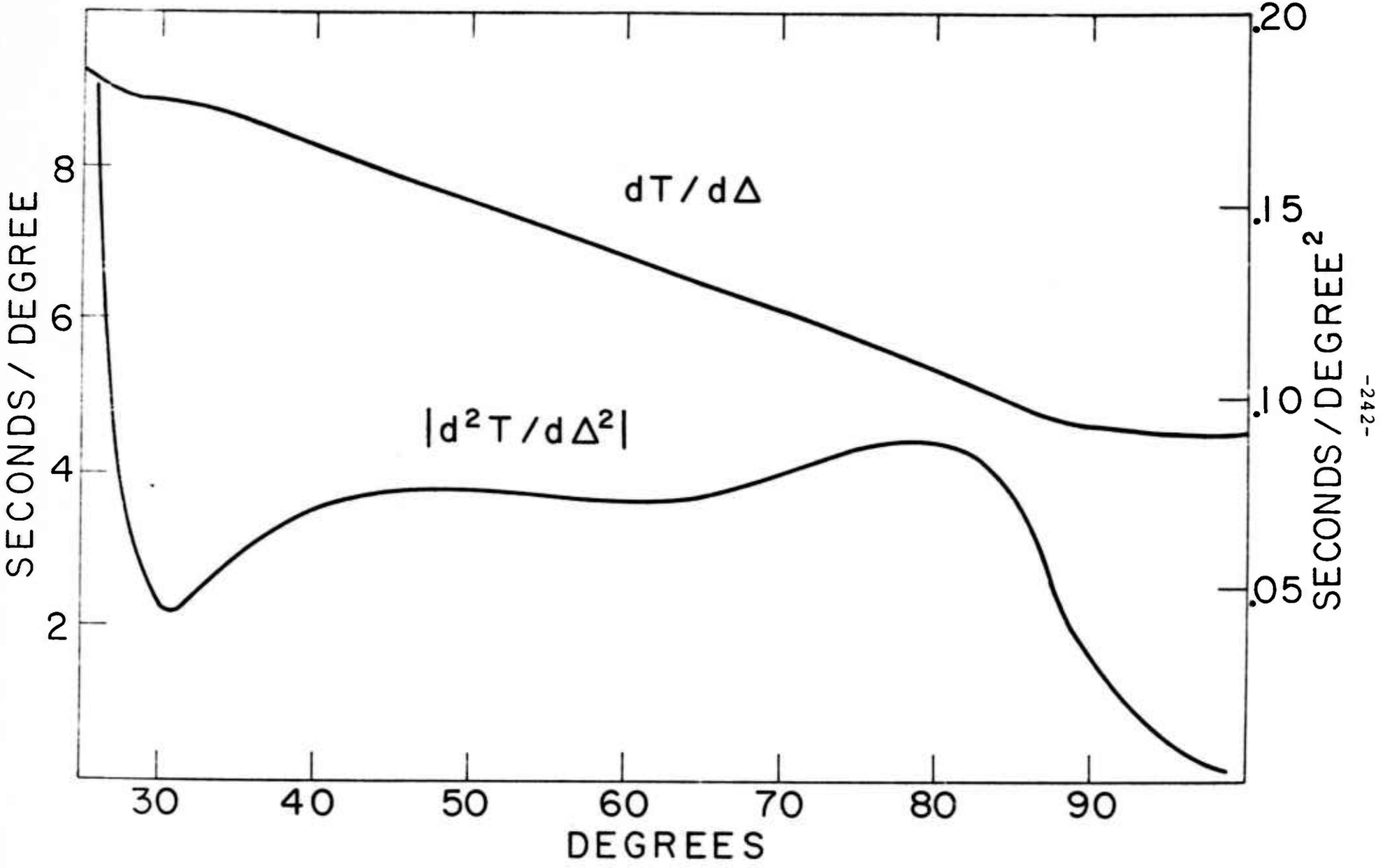
dT/dΔ
|d²T/dΔ²|
SECONDS/DEGREE
SECONDS/DEGREE²
DEGREES
2
4
6
8
.05
.10
.15
.20
30
40
50
60
70
80
90

Figure 8

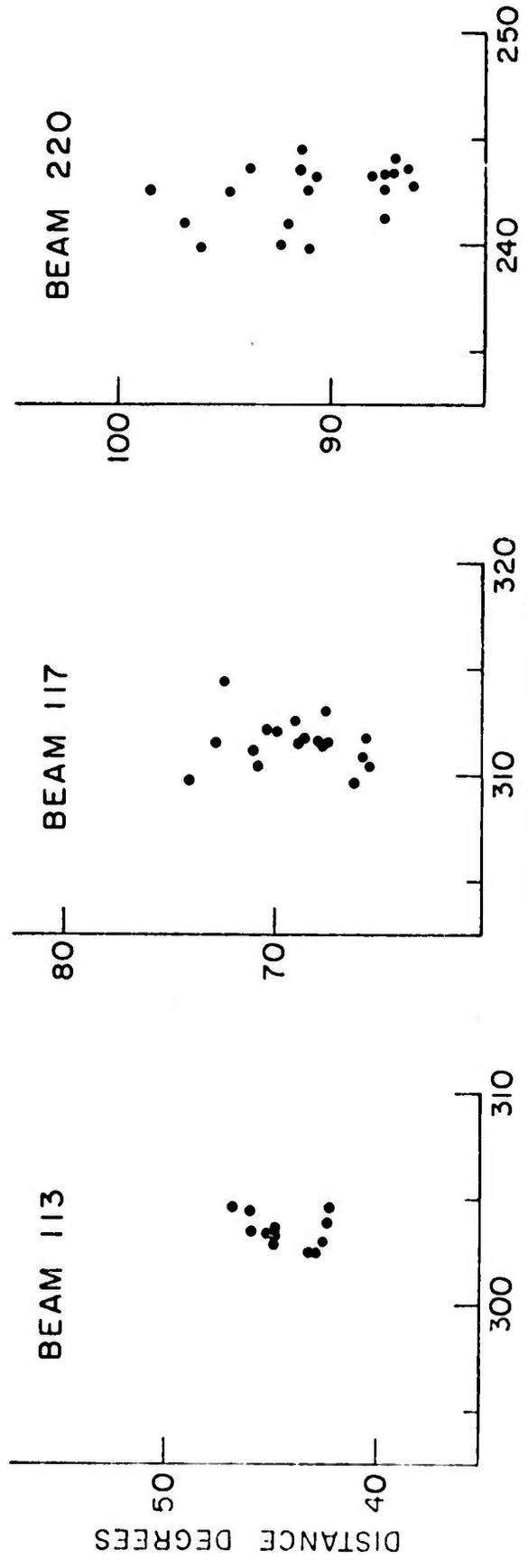
BEAM 220
BEAM 117
BEAM 113
DISTANCE DEGREES
AZIMUTH DEGREES
100
90
80
70
50
40
250
240
320
310
310
300

Figure 9

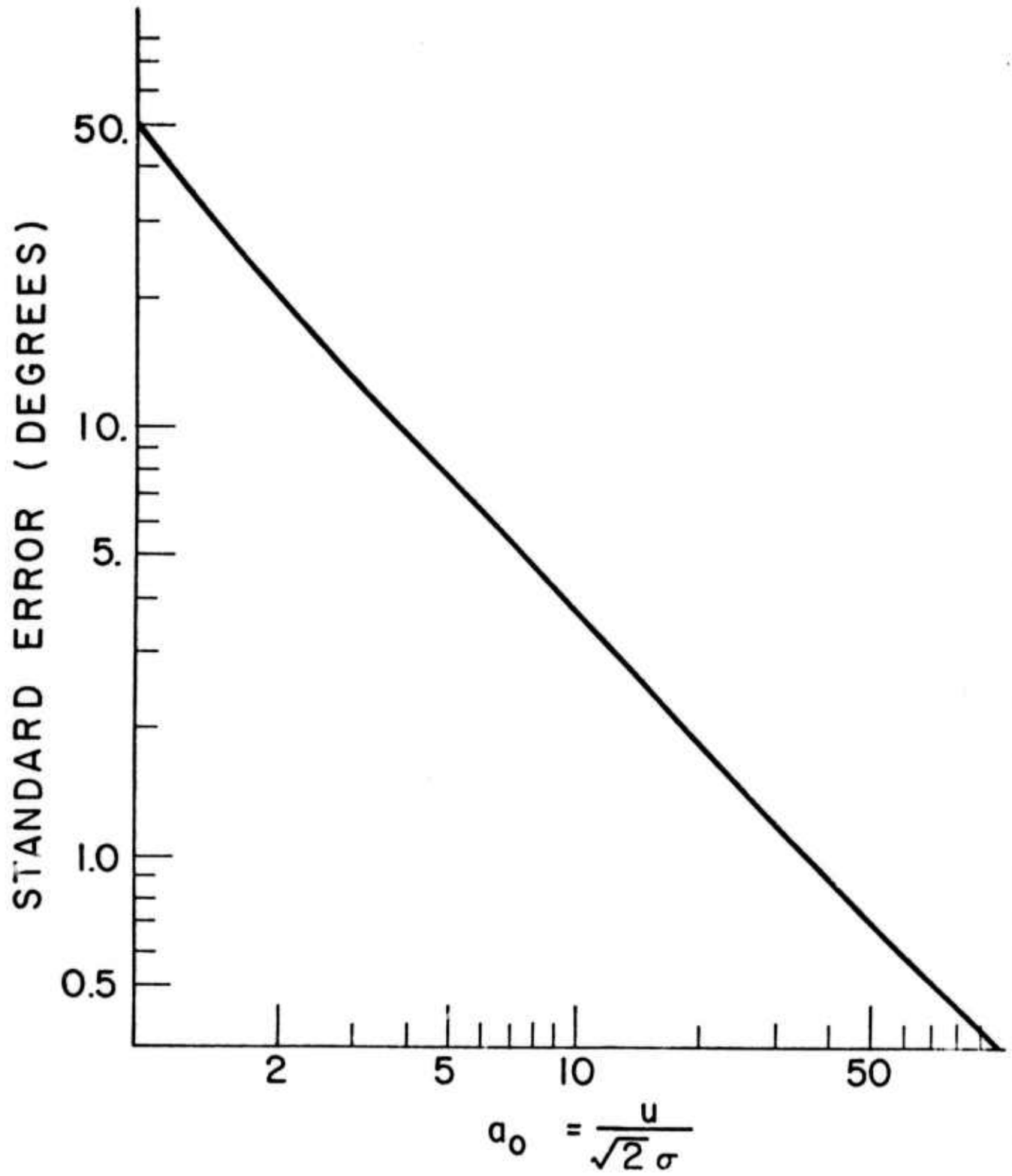
STANDARD ERROR (DEGREES)
50.
10.
5.
1.0
0.5
2
5
10
50
$a_0 = \frac{u}{\sqrt{2}\sigma}$

Figure 10

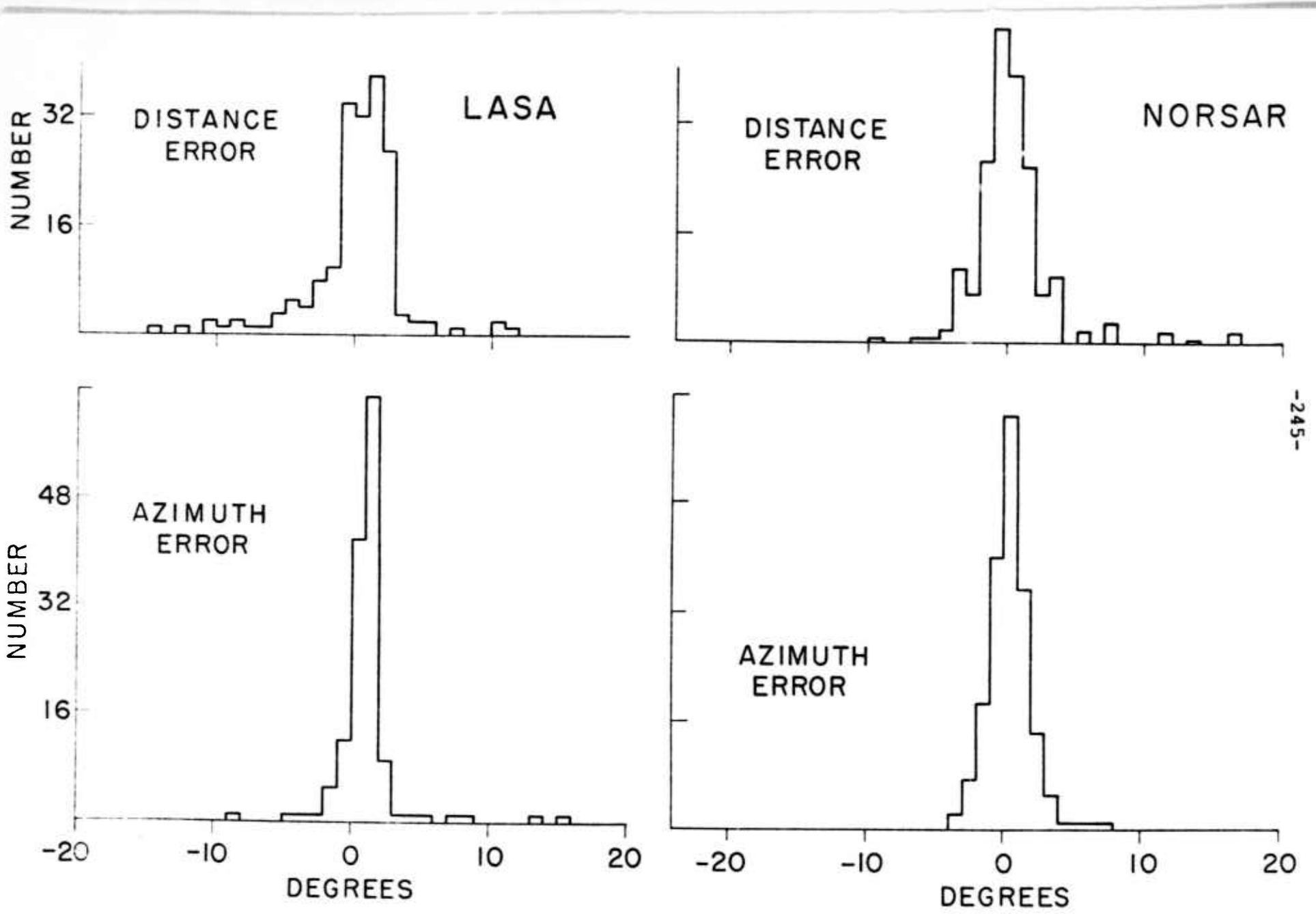
NUMBER
32
16
DISTANCE
ERROR
LASA
DISTANCE
ERROR
NORSAR
48
32
16
AZIMUTH
ERROR
AZIMUTH
ERROR
-20
-10
0
10
20
DEGREES
-20
-10
0
10
20
DEGREES

Figure 11

5. LIST OF PUBLICATIONS DURING CONTRACT YEAR

Aki, K., Recent results on the mechanism of earthquakes with implications on the prediction and control program, Tectonophysics, 13, 423-446, 1972a.

Aki, K., Scaling law of earthquake source-time function, Geophys. J. Roy. Astron. Soc., 31, 3-25, 1972b.

Aki, K., Scattering of P waves under the Montana LASA, J. Geophys. Res., 78, 1334-1346, 1973.

Ida, Y., Stress concentration and unsteady propagation of longitudinal shear cracks, J. Geophys. Res., 78, 3418-3429, 1973a.

Ida, Y., The maximum acceleration of seismic ground motion, Bull. Seism. Soc. Am., 63, 959-968, 1973b.

Ida, Y., Cohesive force and unsteady propagation of a longitudinal-shear crack, Proceedings of the Conference on Dynamic Crack Propagation, Lehigh University, July, 1972, in press.

Julian, Bruce R. and M.K. Sengupta, Seismic travel time evidence for lateral inhomogeneity in the deep mantle, Nature, 242, 443-447, 1973.

Reasenberg, P. and K. Aki, A precise, continuous measurement of seismic velocity for monitoring in situ stress, submitted to J. Geophys. Res., 1973.

Rosenman, M. and S.J. Singh, Quasi-static strains and tilts due to faulting in a viscoelastic half-space, Bull. Seism. Soc. Am., in press, 1973.

Shlien, S. and M.N. Toksöz, Automatic event detection and location capabilities of large aperture seismic arrays, Bull. Seism. Soc. Am., in press, 1973.

Singh, S.J., Generation of SH-type motion by torsion-free sources, Bull. Seism. Soc. Am., in press, 1973a.

Singh, S.J., A spherical cavity in a micropolar elastic medium and related problems, submitted to Int. J. Eng. Sci., 1973b.

Singh, S.J. and M. Rosenman, On the disturbance due to a spherical distortional pulse in an elastic medium, Pure and Applied Geophys., in press, 1973a.

Singh, S.J. and M. Rosenman, Quasi-static deformation of a viscoelastic half-space by a displacement dislocation, Phys. Earth Planet. Interiors, in press, 1973b.

Smith, A.T., Jr. and M.N. Toksöz, Stress distribution beneath island arcs, Geophys J. Roy. Astron. Soc., 29, 284-318, 1972.

Solomon, S.C., On Q and seismic discrimination, Geophys. J. Roy. Astron. Soc., 31, 163-177, 1972.

Solomon, S.C., Shear-wave attenuation and melting beneath the mid-Atlantic ridge, J. Geophys. Res., in press, 1973.

Toksöz, M.N., Subduction of the lithosphere and the causes of deep focus earthquakes, Benioff volume, in press, 1973.

Toksöz, M.N. and H.H. Kehrer, Tectonic strain release by underground nuclear explosions and its effect on seismic discrimination, Geophys. J. Roy. Astron. Soc., 31, 141-161, 1972.

Toksöz, M.N., N.H. Sleep and A.T. Smith, Evolution of the downgoing lithosphere and the mechanisms of deep focus earthquakes, Geophys. J. Roy. Astron. Soc., in press, 1973.

Wiggins, R.A., G.A. McMechan and M.N. Toksöz, The range of earth structure nonuniqueness implied by body-wave observations, Rev. Geophys. Space Phys., 11, 87-113, 1973.

6. LIST OF THESES COMPLETED DURING CONTRACT YEAR

Johnson, C.E., Regionalized earth models from linear programming methods, M.S. Thesis, M.I.T., Sept., 1972.

Sengupta, M.K., A travel-time study using deep-focus earthquakes, M.S. Thesis, M.I.T., May, 1972.

Shlien, S., Automatic classification of seismic detections from large aperture seismic arrays, D.Sc. Thesis, M.I.T., June, 1972.

Sleep, N.H., Deep structure and geophysical processes beneath island arcs, Ph.D. Thesis, M.I.T., Jan., 1973.